Alma Mater Studiorum
Università degli Studi di Bologna

FACOLTÀ DI SCIENZE MATEMATICHE FISICHE E NATURALI

DOTTORATO di RICERCA
in
FISICA NUCLEARE E SUBNUCLEARE
(FIS/04)

B mesons proper time measurement with the LHCb experiment: impact on physics parameters and calibration methods

Tesi di Dottorato di:
Dott. Gabriele Balbi

Relatore:
Prof. Domenico Galli

Coordinatore:
Prof. Fabio Ortolani

Correlatrice:
Dott. Stefania Vecchi

Anno Accademico 2006-2007
Ciclo XIX del Dottorato di Ricerca in Fisica

Contents

List of Figures

Introduction

Apparently, the universe that we observe is just composed by ordinary matter. This fact may sound trivial, but indeed it hides one of the most intriguing questions that still deserve a convincing answer from the scientific community. In fact, it is believed that, before the Big Bang, not space nor time existed. The Big Bang then acted as a singularity from which time, space and all the matter were originated. Since in every High Energy Physics process equal amounts of matter and anti-matter are created, it is likely that during the first instants after the Big Bang, matter and anti-matter were equally populating the early universe. Then, matter and anti-matter started to annihilate each-other through the ordinary processes that we study every day in particle physics, and thus the question: why matter is still there surviving nowadays, but anti-matter seems to have disappeared completely? The most plausible answer is that matter and anti-matter have not a symmetric behaviour: they should somehow be different!

The first experiments pointing out the different behaviour of matter and anti-matter date back to the 1960's, when for the first time a break of the CP symmetry — i.e. the symmetry which transforms a particle into its anti-particle in the framework of particle field theory — was observed in the decays of the neutral kaons. Since then, many experiments with improving precision were carried out, confirming such spectacular phenomena and culminating with the measurement of the violation of the CP symmetry in the decays of the neutral B-mesons, by the BaBar and Belle collaborations at the beginning of the new century.

It is worth to mention that the first measurement of the CP violation in the B-meson sector by BaBar and Belle has been one of the most important discoveries of the modern particle physics. Until this discovery, which is confirming so far the spectacular consistency of the Standard Model, CP violation remained, during almost 40 years, confined in the kaon sector. It was then of paramount importance to verify whether the description of the CP violation in the Standard Model, which was able to explain the measurements for the kaons, was also able to correctly predict the existence of the CP violation in the B-meson sector, i.e. confirming that the flavour sector of the Standard Model was a general theory for these phenomena.

The fact that such measurements needed almost 40 years to be performed can be explained by considering that it was required to overcome a technological challenge. In fact, as it will be discussed throughout this thesis, the measure-

ment of the CP violation in the B-meson sector requires the determination of the proper decay time of the B-mesons themselves. In order to do that, very accurate silicon detectors were required, capable of a spazial resolution on the decay vertices of the order of 100 μm. At the same time, due to the small branching ratios of the interesting decays involved, very high luminosities were required in order to produce a sufficient number of B-mesons, from e.g. e^+e^- collisions at the $\Upsilon(4S)$ energy, at the level of $10^{32}\,\mathrm{s}^{-1}\mathrm{cm}^{-2}$. These two challenges were solved for the first time together at the asymmetric B-factories, were the BaBar and Belle detectors are still operating.

It is known that the Standard Model is not the ultimate description of elementary particle dynamics, but an effective field theory valid to the energy scale explored so far. There are indeed already available experimental evidence of phenomena that cannot be described within the Standard Model, like for instance neutrino oscillations. Finding and identifying hints of New Physics in the quark flavour dynamics still represents a great challenge at the colliders. In order to distinguish among several scenarios of New Physics depicted by different theoretical models, it is very important to study CP violation phenomena and rare decays with high precision. In general a more precise knowledge of the Cabibbo-Kobayashi-Maskawa (CKM) matrix, responsible in the Standard Model for the quark flavour mixing, may reveal new sources of CP violation, e.g. due to the presence of New Physics particles in higher order processes.

The LHCb (Large Hadron Collider beauty) experiment is one of the four experiments at the LHC, and is specifically dedicated to explore the B-meson dynamics. To this end, LHCb will exploit the large beauty production cross section, expected to be about $500\,\mu b$ at $14\,TeV$ p-p collisions. Differently from the B-factory case, the hadronization of the b-quarks at LHC will generate all the possible B-hadrons, remarkably the B_s and B_c mesons, where the present experimental knowledge is still rather poor. The number of $b\bar{b}$ pairs produced at the LHCb interaction point will be of the order of 10^{12} per year, allowing for the search of extremely rare decays, with branching fractions at the level of 10^{-9}. In order to reduce the acquisition rate to a sustainable level (order of 2 kHz), maintaining at the same time a high efficiency on the signals of interest, LHCb is provided with an efficient and flexible trigger system. LHCb, by means of its vertex detector, will be able to reconstruct the proper time of decays with a great accuracy ($\sim$ 40 fs) and therefore it is well suitable to study minutely CP violation for the very fast oscillating B_s mesons. Moreover the features of the LHCb detector are also suitable to study the charm and τ decays, which also offer another great opportunity to find out New Physics.

For my Ph.D thesis, I developed a new procedure (called the FITPull method) to monitor and check the measurement of the B decay proper time and its error. The procedure is based on the use of the kinematical constraints between the track parameters of the particles involved in the B decays, without relying on Monte Carlo information. The method can be calibrated on the decay mode $J/\Psi \rightarrow \mu\mu$, which will be exploited by LHCb as a general monitor channel

for the charged tracks calibration, with the aim of identifying and eventually recovering imperfect measurements of the track parameters. I applied the FITPull method to two different reference channels: $B \to h^+h^-$ and $B_s \to D_s\pi$, evaluating its performance in correcting track measurement errors. I have also contributed to the implementation of a software tool, the `GlobalFitter`, that is used to compute the FITPull distributions of the input track parameters, and I released the package that will be used in the official LHCb analysis framework.

The thesis is organized in 4 chapters. In Chapter 1 the LHCb experiment, its sub-detectors and trigger system are described. Chapter 2 introduces the theoretical framework of the B-meson mixing and CP violation in the Standard Model, with some details of the relevant measurements that LHCb will perform. In Chapter 3 the FITPull method is described, and finally Chapter 4 gathers the results of some studies on Monte Carlo simulated data, by investigating the impact of the calibration method on the physical quantities which are mostly affected by the precision of the B proper time measurement.

Chapter 1

The LHCb experiment

In the introduction it has been pointed out that the aim of the LHCb experiment is the exploration with high precision of the CP violation in B sector. In order to identify B decays LHCb must fulfill a series of requirements:

1. Accurate reconstruction of the primary and secondary vertexes and precise proper time measurements.
2. Good particle tracking, even with high occupancy.
3. Accurate particle identification in a wide momentum range (1-150 GeV/c).
4. Trigger system with high efficiency and high background rejection power.

The LHCb spectrometer (fig.1.1) was designed to reach all the forementioned requirements.

In the next sections, I will give you a short description of the LHC characteristics and then I will describe the LHCb detector with its components.

1.1 The LHC environment

The LHC supplies two interacting beams of protons with an energy in the center mass of $\sqrt{s} = 14$ TeV at the bunch crossing rate of 40 MHz with a luminosity $\mathcal{L}$ of $2 \cdot 10^{32} cm^{-2} s^{-1}$. In the LHC accelerator the particles are gathered in bunches, each one containing about 10^{11} particles. Hence 40 MHz is the fundamental frequency for the LHC and its associated electronics. The number and the structure of bunches in each beam is:

$$3564 = 12 \times 297 =$$

$$= 11 \times [3 \times (81b + 8e) + 30e] + [2 \times (81b + 8e) + 119e]$$

where b means a full bunch whereas e stands for an empty one. There are 3564 space bunches, 2835 are occupied and 729 are empty. The interaction frequency

of the 2 beams is not the same in all the interaction points of the LHC due the presence of the empty bunches. Indeed the collisions happen only when the 2 beams are in phase, i.e. when two full bunches cross each others.

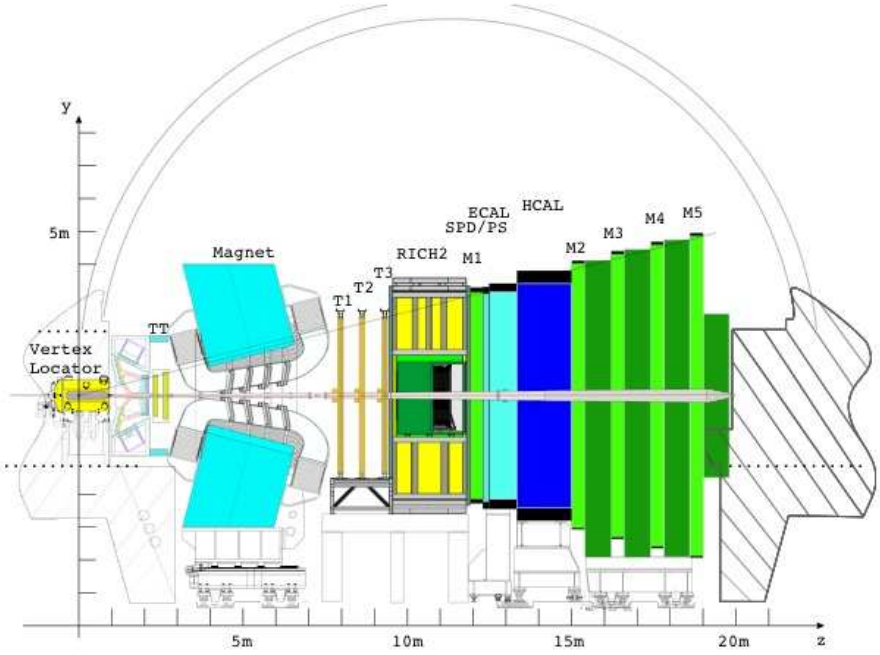

Figure 1.1: The LHCb detector is composed by several subdetectors.

The position of the interaction point of LHCb ensures 2622 crossing bunches that represents only the 73.6% of the total full bunches in the rings, therefore the effective interaction frequency of LHCb will be $\nu_{eff} = 29.5$ MHz.

The Monte Carlo simulations, based on the current knowledge, have shown that the $b\overline{b}$ mesons are produced predominantly at low polar angles. For this reason a single-arm detector covering the high rapidity space can detect efficiently both b and $\overline{b}$ decay products. LHCb was designed according this criteria.

Its acceptance extends out to 300 mrad in the horizontal (bending) plane and 250 mrad in the vertical plane (with a lower cut due to the beampipe of 20 mrad). We expect, in one year data taken ($10^7 s$), we will collect about 10^{12} $b\bar{b}$ events, since the expected quark b production cross section is about 500μb. In fact the rate production of the $b\bar{b}$ events is:

$$R_{b\bar{b}} = \sigma_{b\bar{b}}\mathcal{L} \tag{1.1}$$

The inelastic cross section has been estimated close to 80 mb. So, unfortunately, the ratio between the rate of $b\bar{b}$ and inelastic events will be $\sim 0.6\%$. Due to

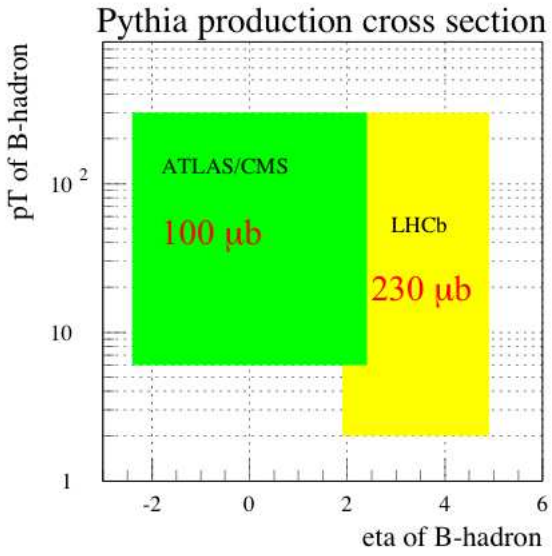

Figure 1.2: LHCb was designed to maximize the B acceptance within cost and space constraints. The forward spectrometer relies on much softer p_T triggers, efficient also for purely hadronic B decays.

	Cross Section[mb]
σ_{Tot}	100
σ_{inel}	80
$\sigma_{non-radiative\,inelastic}$	55
$\sigma_{visible\,cross\,section\,LHCb}$	68
σ_{bb}	0.500
σ_{cc}	1.5

Table 1.1: Cross sections for LHCb experiment.

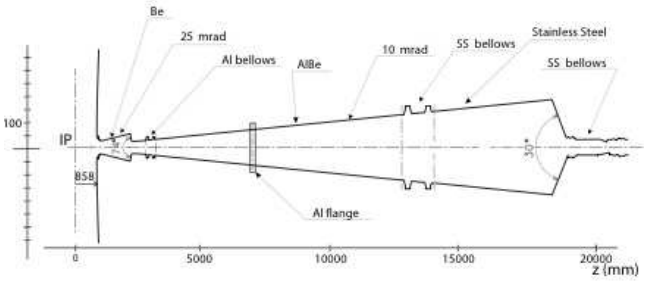

Figure 1.3: The beam pipe in a lateral view.

the LHCb design the best environment is reached with few primary interactions per bunch crossing. The distribution of p-p interactions occurred per bunch crossing can be described by a Poisson distribution:

$$P(\mu, n) = \frac{\mu^n}{n!} e^{-\mu} \tag{1.2}$$

where the average is given by:

$$\mu = \frac{\mathcal{L}\sigma_{tot}^{\cdot}}{\nu_{eff}} \tag{1.3}$$

1.2 The LHCb detector

1.2.1 The Beam Pipe

The proton beams circulate in the accelerator inside ultra vacuum pipes, in order to minimize the collisions with the residual gas in the pipe. The pipe has to be sufficiently strong to stand the difference in pressure between the vacuum inside it and the air outside in the cavern. Close to the IP, the pipe has to be sufficiently transparent to all the primary particles to reduce multiple scattering effects. The best material, that has the mechanical requirements to stand the pression and to ensure the high radiation transparency, is beryllium. Beryllium is used pure in several parts of the beam pipe, as well disguised as aluminium alloy.

The beam pipe, within the LHCb detector, is composed by three different parts. The first one, placed around the interaction point, is cylindrical with a radius of approximately of 120 cm and 1.8 m long. This cylinder is followed by two conical sections. The first one has aperture of 25 mrad and it is 1.4 m long. The latter section has an aperture angle of 10 mrad and it is 17.3 m long.

1.2.2 The VELO

The presence of displaced secondary vertices respect to the primary vertex at the IP is a remarkable and distinctive feature of the b-hadron decays. For this

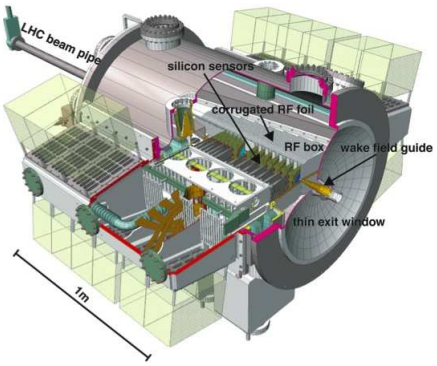

Figure 1.4: In this picture is depicted the Velo structure.

reason the VErtex LOcator has to provide precise measurements of the track coordinates close the interaction region. The VELO was optimized for the best impact parameter resolution, the low cost of fabrication, a high thermal conductivity and the less material budget[1].

To minimize the impact parameter error, the extrapolation to primary vertex has to be as short as possible. Thus it requires detector stations as close as possible to the beam pipe.

This detector is composed by 21 silicon stations placed along the beam direction, each one composed by two strip sensors, with 220μm thickness, for the r and ϕ measurements.

Also in order to minimize the material in the interaction region, the VELO is enclosed in a thin aluminium box with a pressure of less than 10^{-4} mbar. The detector vacuum box is equipped with corrugated foils to limit the amount of material seen by detected particles. In these conditions the typical resolution for the primary vertex will be, along the z axis, about 40μm, whereas along the x and the y axes will be 10 μm. For the secondary vertices the spatial resolution depends on the number of the tracks involved in the reconstruction process and can fluctuate from 100 to 300 μm depending on the decay under study.

1.2.3 The RICH

In LHCb, the hadron identification, over a wide momentum range (1-150GeV/c), will be performed by two Ring Imaging Cherenkov detectors (RICH) equipped with 3 different radiators (Aerogel, CF_4, C_4F_{10}). These detectors exploit the Cherenkov effect to identify the particles. The RICH1 is placed before the TT station, after the VELO (fig. 1.6).

[1]The resolution is dominated by multiple scattering thus a minimisation of material budget is an important design parameter to reach a better performance.

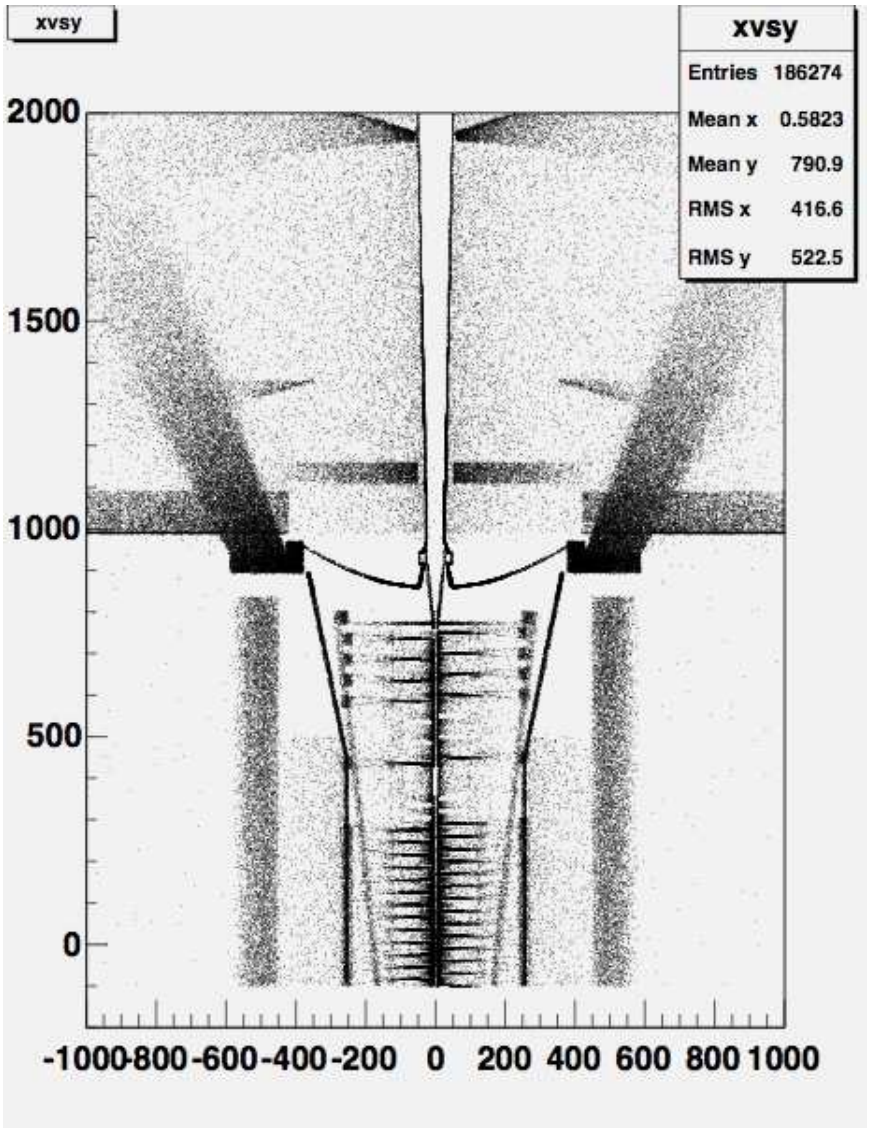

Figure 1.5: A picture with the projection of the Velo and the beam pipe, obtained observing the secondary interactions in a Monte Carlo simulation.

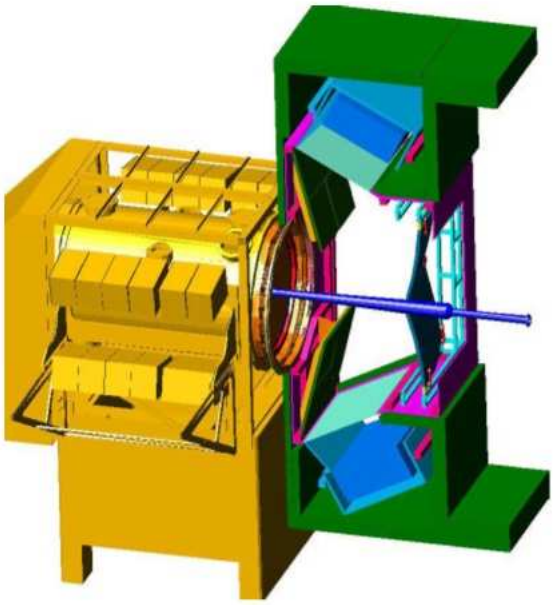

Figure 1.6: The Velo sealed to RICH1 detector.

It contains two radiators: silica aerogel and fluorocarbon gas C_4F_{10}. It is fundamental to the particle identification of the low momentum range and it plays an important role for the b flavour tagging through the $b \to c \to s$ quark decay chain.

The high momentum particles, up to $150 GeV/c$ are measured by the RICH2 placed between the T3 station and the M1 chamber. filled with CF_4 gas.

Cherenkov radiation is emitted when a charged particle traverses a medium with a velocity greater than the velocity of light in that medium. If the momentum of a certain particle exceeds a threshold, depending on its mass, a cone of light is emitted in the forward direction. The focusing of the light is accomplished using spherical mirrors. They are tilted to bring the image out of the detector acceptance (fig.1.9 and fig.1.7). In this manner the cones of light appear as circles on the focal plane where a matrix of a pixeled photodetectors HPD (Hybrid Photomultiplier Detector) is placed: 168 for the RICH1 and 262 for the RICH2. Each HPD tube has 1024 pixels of size $0.5 \times 0.5\ mm^2$. Using the momentum of the reconstructed tracks, the mass and thus the particle type can be determined. The basic equation that relates the angle θ_c and the particle momentum is:

$$\cos\theta_c = \frac{1}{n\beta} \tag{1.4}$$

with n being the refraction index of the radiator medium. Particles start to radiate Cherenkov light above a threshold $\beta_{th} = 1/n$. A large refractive index

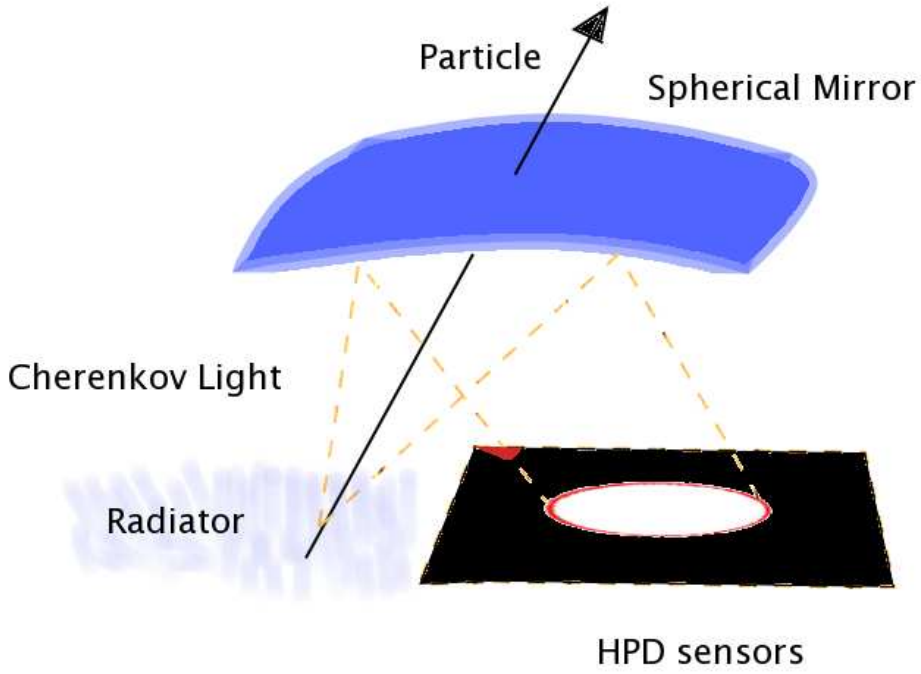

Figure 1.7: The particle, if its momentum goes over the threshold, emits a Cherenkov light cone which is projected by the mirrors on the HPD plane. In such way each track is associated to a circle on the plane. The radius determines, with the knowledge of the momentum, the mass of the particle.

	RICH2	RICH1	
	CF_4	C_4F_{10}	aerogel
n	1.0005	1.0014	1.03
θ_{MAX} [mrad]	32	53	242
$p_{threshold}(\pi)$ [GeV/c]	4.4	2.6	0.6
$p_{threshold}(K)$ [GeV/c]	15.6	9.3	2.0
$\sigma_\theta^{emission}$[mrad]	0.31	0.71	0.66
$\sigma_\theta^{chromatic}$[mrad]	0.42	0.81	1.61
σ_θ^{pixel}[mrad]	0.18	0.83	0.78
σ_θ^{track}[mrad]	0.20	0.42	0.26
σ_θ^{total}[mrad]	0.58	1.45	2.00
N_{pe}	19.1	35.3	6.9

Table 1.2: The table contains the main characteristics of the three radiators and the principal errors introduced in the Cherenkov angle measurement.

	RICH2	RICH1	
	CF_4	C_4F_{10}	aerogel
π	0.03157	0.05286	0.24194
K	0.03101	0.05252	0.24187
p	0.02936	0.05157	0.24167
e	0.03162	0.05288	0.24195
μ	0.03159	0.05287	0.24194

Table 1.3: Cherenkov angles for the three radiators for a particle momentum of 80GeV/c, with different mass hypotheses.

allows to identify particles in the low-momentum range, while a small index is useful in the high-momentum range.
Therefore as a function of the mass m

$$p = cm\beta\gamma \;\Rightarrow \beta = \frac{p}{\sqrt{m^2c^2 + p^2}} \;\Rightarrow \tag{1.5}$$

$$\cos\theta_c = \frac{1}{n} \cdot \frac{\sqrt{m^2c^2 + p^2}}{p} = \frac{1}{n} \cdot \sqrt{\frac{m^2c^2}{p^2} + 1} \tag{1.6}$$

The Cherenkov-angle resolution is limited by the finite pixel size of the HPD, the variations in gas pressure, the knowledge of the trajectory of the incident particle, the photon emission point, the effects of chromatic aberration and the photoelectrons statistics.

The expected number of detected photoelectrons from a track coming through a Cherenkov radiator of length L is given by

$$N_{pe} = \left(\frac{\alpha}{\hbar c}\right) L\epsilon_A \eta \int QRT \sin^2\theta_c dE_\gamma \tag{1.7}$$

where Q is the HDP quantum efficiency, R the mirror reflectivity and T is the quartz cap window transmittance (typical values are reported in table 1.2).

An event in the RICH is a set of ring images, which may overlap where there is a high track density. The Cherenkov rings are not perfect circles but they are elliptical in shape due to the direction of the track in the acceptance. Instead of attempting to fit these circles, a great simplification is achieved by reconstructing the Cherenkov angles at emission for each hit under the assumption that it is originated from a given track.

A pattern recognition algorithm is performed in order to individuate the exact particle mass. It has been conceived structured in two different steps. The first step is to decide from which track has originated each detected photon. Then the second step is to fit those hits with a ring originated by that track. The ring radius allows to calculate θ_c.

The pattern of hit pixels observed in the RICH photodetector is compared to the pattern that would be expected under a given set of mass hypotheses for

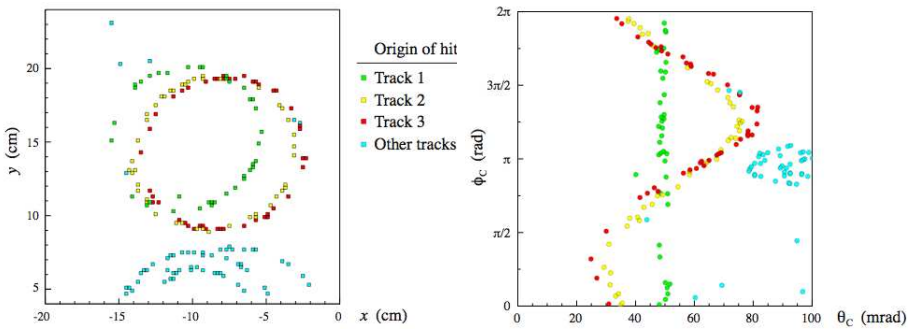

Figure 1.8: Example of a RICH event. The first image is a zoom of a region of the detection plane. Assuming that the truly hits are coming out from the track 1, it can be noticed the uniform distribution of the azimuthal angle ϕ_c against the polar angle θ_c.

the reconstructed tracks passing through the detectors, using the knowledge of the RICH optics. A likelihood is determined from this comparison and then the track mass-hypotheses are varied to maximize the likelihood. The RICH systems give as output a set of probabilities for each single particle type hypothesis.

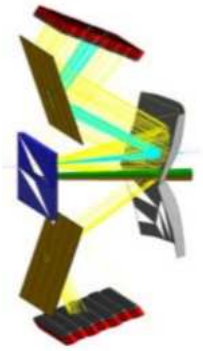

Figure 1.9: RICH1. The Cherenkov radiation is emitted and led by the spherical mirrors to the photomultipliers array.

The expected performances of the RICH system has been evaluated using the simulated data. The performances are quantified in terms of efficiency ϵ (the fraction of true particles of a given type that are identified correctly) and the purity $\mathcal{P}$ (the fraction of tracks that have been correctly identified). The efficiencies are higher than 80% and the purities are also high but for muons we have some contamination from pions [16].

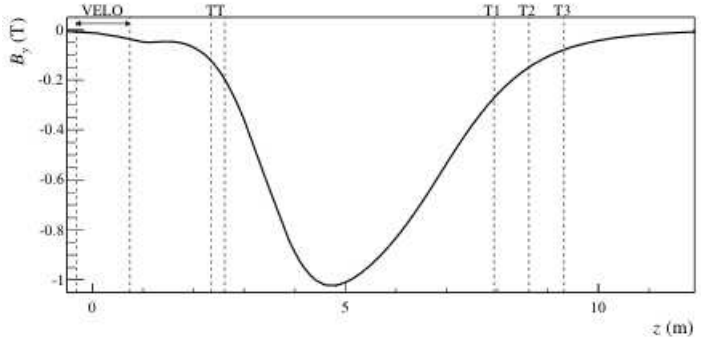

Figure 1.10: B-Field in the detector.

1.2.4 The Magnet

LHCb exploits the forward region of the pp collisions and requires a dipole field with a free aperture of ± 300 mrad horizontally and ± 250 mrad vertically. Tracking detectors in and near the magnetic field have to provide momentum measurement for charged particles with a precision of about 0.6% for momenta up to 140 GeV/c. This demands an integrated field of 4 Tm for tracks originating near the primary interaction point.

The LHCb magnet is a warm magnet due to the significantly lower costs, the faster construction and the lower risks. It also provides the possibility of a rapid ramping up of the field, synchronous to ramping up of LHC magnets, as well as regular field inversion.

The central field is 1.1 T and it provides a bending power along the beam axis of $4Tm$.

As shown in fig.1.10, the$B$ field is not confined within the magnet region. A non negligible contribution is recorded in the TT station. This feature allows to estimate, with a rough precision, the momenta of the tracks in a very short time, at trigger level. A more complete and precise estimation needs the information from the T stations, but it would take too much time for the trigger system.

In the VELO region the B field contribution is very small and limited to the last detector planes.

1.2.5 Silicon tracker and straw tubes: the TT chamber and the T1-T3 tracker chambers

The LHCb Silicon Tracker is a large-surface silicon microstrip detector which constitutes an important part of the LHCb tracking system. It uses single-sided silicon strip detectors with a strip pitch of approximately 200 μm, produced from 6 inches wafers and arranged into up to 38 cm long readout strips. The tracking stations are optimized for momentum measurement so they have a good spatial resolution in the bending plane and sufficient pattern-recognition capabilities in

Figure 1.11: The installation of the magnet in the LHCb cavern.

the non-bending plane of the magnet.

The Silicon Tracker collects two parts: the "Trigger Tracker" (TT) station, placed between RICH1 and the LHCb dipole magnet, and the "Inner Tracker" (IT) that covers the innermost region of the tracking stations T1-T3, between the LHCb dipole magnet and RICH2. (fig.1.13). Outside the T1-T3 stations, the OT (Outer tracker) is placed and it covers a great part of the tracking volume. The OT system is constituted by straw tubes.

The TT chamber is devoted to two different purposes. Firstly, it will be used in the trigger to assign transverse-momentum information of large impact parameter tracks. Secondly, it will be used in the offline tracking. Moreover it is fundamental to reconstruct the long living neutral particles (K_s) that decay outside of the pertinent region of the VELO and tracking the low momentum particles that are bent out of the acceptance before reaching the tracking stations T1-T3.
The TT chamber is constituted by four planes, gathered in groups of two, called TTa and TTb, of wide pitch silicon microstrip sensors and covers an area of about 7 m^2. The orientation of the strips for the first plane is vertical, the 2nd plane has strips rotated by -5^0 around the beam axis, the 3rd plane by $+5^0$, and for the last plane the strips are again vertical. The layout of this detector is shown in fig.1.12.

The particle fluxes are very high near the LHCb beam pipe, but fall off rapidly with increasing distance, therefore the tracking system behind the mag-

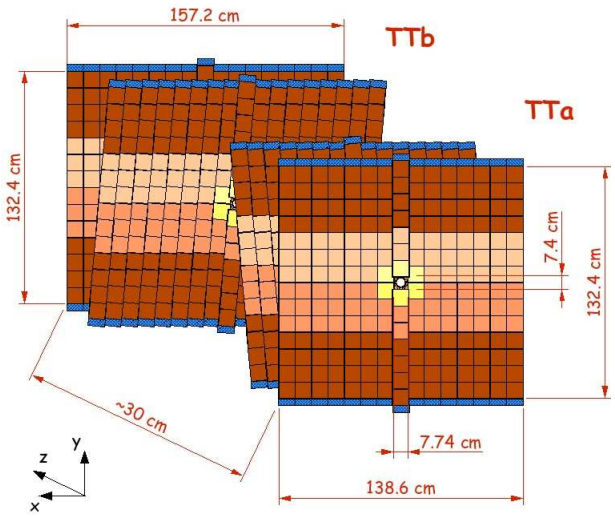

Figure 1.12: The TT chamber layout.

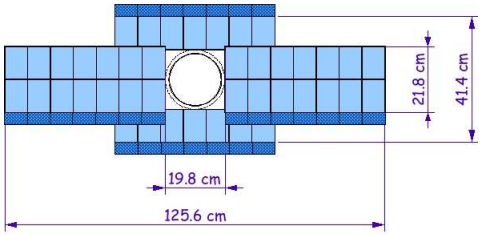

Figure 1.13: Inner Tracker: the cross shape of the detector

net, composed by the T1-T3 stations, is divided in two parts: in the highest particle flux region there is a small silicon detector at high rapidity and high granularity (the inner tracker). The second part is a drift chamber detector using straw-tube technology, the outer tracker OT, that covers the most of the LHCb acceptance surrounding the inner tracker. Every tube has a radius of 5mm and it is filled with a mixture of gases like $Ar/CF_4/CO_2$. This configuration achieves a drift time about 25ns. Each outer tracker station consists of multiple layers of wires with both vertical orientation and ± 5 degree stereo angles.

1.2.6 The calorimeter system: ECAL and the HCAL

The calorimeter system is very important for the experiment since it can select at trigger level 0 high transverse energy hadron, electron, photon candidates. Also the calorimeter system provides the electron identification that is fundamental for flavour tagging with the semileptonic electron decays. Another qualifying feature is the precision requested to reconstruct all the B-decays that contains prompt γ or π^0.

As seen in fig.1.1, the calorimeter system is composed by the electromagnetic (ECAL) and the hadronic (HCAL) calorimeters. To improve the e/γ discrimination the ECAL is preceded by the SPD (scintillator pad detector) and the PS (preshower) devices.

To get optimal energy resolution for high energy photon showers, the ECAL must be thick enough. In the [15] was proposed a 25 X_0. Whereas the trigger requirements on the HCAL resolution allow 5.6 interaction lengths.

- ECAL: The ECAL will be built with the shashlik technology. That allows to reach a resolution for the electromagnetic shower of :

$$\sigma(E)/E = 10\%/\sqrt{E} \oplus 1.5\% \tag{1.8}$$

  which, with the preshower information, provides a good electron/hadron separation at trigger and at reconstruction stage. This device has to provide a wide range of digital measurements from a few 10 MeV up to 200 GeV to cover the broad momentum range of the B products.

- HCAL: It is composed by iron/scintillating tiles readout by WLS[2] fibers. Its task is measuring the energy of the hadronic showers. The granularity of this calorimeter is lower then the ECAL and also the energy resolution obtained is:

$$\sigma(E)/E = 80\%/\sqrt{E} \oplus 10\%$$

[2]Wave Length Shifter

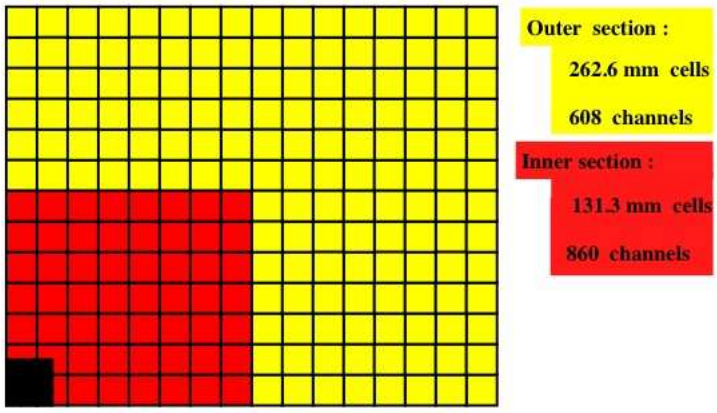

Figure 1.14: Lateral segmentation of HCAL.

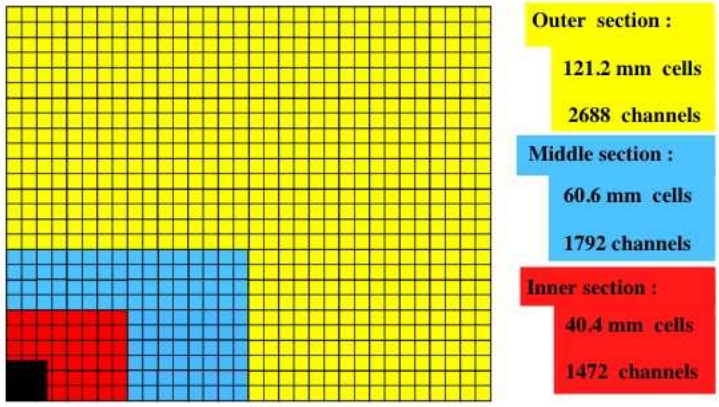

Figure 1.15: SPD/PS and ECAL transverse granularity

- SPD/PS: Before the ECAL there is a 12 mm lead wall. Just before and just after there are two detecting plastic scintillator plane the SPD and the PS. The SPD detector provides the discrimination between neutral and charged particles, whereas the PS contributes to the pion/electrons discrimination.

1.2.7 The muon chambers

The purpose of the LHCb Muon System is to provide fast (L0) triggering and offline muon identification. The system is made of five Stations (M1-M5) of rectangular shape, covering an acceptance of ±300 mrad (horizontally) and ±200 mrad (vertically). M1 is placed in front of the SPD/PS. M2-M5 are located downstream the Hadron Calorimeter (HCAL) and are separated by iron

filters. The stations cover an area of 435 m^2. The total absorber (including the calorimeters) is approximately 20 interaction lengths.

The acceptance of the Muon System is about 20 % for muons from inclusive b decays.

Each station is divided into four regions, R1 to R4, with increasing distance from the beam axis. All the regions have approximately the same acceptance, and their granularity is tuned in order to keep occupancy roughly constant over the detector. The granularity of the readout is higher in the bending plane, in order to give a rough measurement of the track momentum and p_T at trigger level.

The information must be gathered within 20 ns, so the detectors are optimized for speed. Therefore the choice went to Multi Wire Proportional Chambers (MWPC) with 2 mm wire spacing and a small gas gap (5 mm). Triple-GEM detectors are used in the innermost region (R1) of Station M1. This choice was dictated by the better aging properties of this kind of detector. There are 1380 chambers in the Muon System, of 20 different sizes.

The detector readout is made on cathod pads giving a binary (yes/no) information.

The Muon Trigger is based on a five-fold coincidence of the stations. Therefore its efficiency scales as ϵ^5, where ϵ is the efficiency of each station. In order to ensure the necessary high efficiency and adequate redundancy, four layers of detectors are used in M2-M5. Two layers are used in M1 (this is a compromise between performances and material budget before the ECAL/PS/SPD). In practice, since we work at fixed Minimum Bias rate, the dependence on ϵ is less steep (approximately like $\epsilon^{3.5}$). In normal operating conditions $\epsilon = 46$ % for $b \to \mu X$ events inside the acceptance.

1.2.8 The LHCb trigger

The trigger system is one of the most challenging points of the whole experiment. It is projected in order to discriminate the B meson events from the minimum-bias events. This selection is implemented by looking for particles having a large transverse momentum (p_T) and by the presence of secondary vertices.

The trigger of LHCb is constituted by two different and sequentially levels. The first one (L0) is a hardware selector, whereas the second one (HLT) implements a decision software algorithm.

1.2.8.1 The first level L0

The trigger L0 has an input rate of 40 MHz and an output rate of 1 MHz. It is based on the identification of leptons, hadrons and photons with high-transverse momentum (p_T) in calorimeters (scintillanting pad detector, preshower, electromagnetic and hadronic calorimeters) and muon chambers, combined with a pile-up veto. The pile-up velo unit identifies bunch crossings with more than one pp interaction using a dedicated part of the vertex detector system and the

calorimeters. The p_T thresholds for the hadrons and muons can be adjusted according to physics needs.

In case of a positive answer, the L0 decision, the L0 decision unit passes the information on the high p_T particle to the following trigger.

1.2.8.2 The second level of trigger, HLT

After the hardware trigger L0, there is an another trigger device which is a software trigger devoted to a further event discrimination in order to draw the pure B events out.

In the Trigger TDR [14]the original schema of the trigger system placed after the L0 level is described. It was composed by two different data streams:

- Level 1 with a latency of about 58 ms at maximum L0-accept rate of 1.1 MHz. The event size was dominated by VELO and TT for a total rate of 5 GByte/s.
- HLT with no latency limitation. It runs on the L1-accept rate of 40 kHz with a LHCb event size of approximately 5 GByte/s.

The two streams shared the same readout network and the Event Farm Filter (EFF) .

The new project adopted recently foresees a single data stream at the L0-accept rate of nearly 56 GByte/s. This change provides these advantages:

1. Only one data-flow through the system.
2. Elimination of the subfarm controllers which were charged of the event building and data distribution over the EFF nodes.
3. Cut out of the L1 Trigger Receiver Module and the decision sorter with the relative software.
4. No latency limitations for event processing.
5. Combination of the L1 and HLT trigger processes running over each EFF node into a single program doing away the context switching between them.

There are four streams in the HLT, for a total of 2 kHz output rate. Some select specific$B$ decay streams for physics studies, other trigger for calibration and efficiency studies.

		Rate[Hz]	
Generic Stream	DiMuon	600	Dimuons with a mass above 2.5 GeV and no IP cuts. These events are used to measure the uncertainty on lifetime measurements.
Generic Stream	Inclusive B	900	Events with one high PT and high-IP muon, used for systematic studies of the trigger efficiency and for data mining. Because of the muon, this sample is highly tagging-enriched.
Exclusive	Exclusive B	200	The core physics stream with exclusively reconstructed decays including sidebands and control channels.
Inclusive	Inclusive D^*	300	PID-blind D^* events with $D^0 \to hh$ and no D^0 mass cut. These events allow to measure the PID efficiency and mis-ID rate. Can also be used for CP measurements in D decays.
Inclusive	Optional streams		Other optional inclusive selections are available. For instance the inclusive Phi or high-IP dilepton selections.

Table 1.4: HLT data stream partition

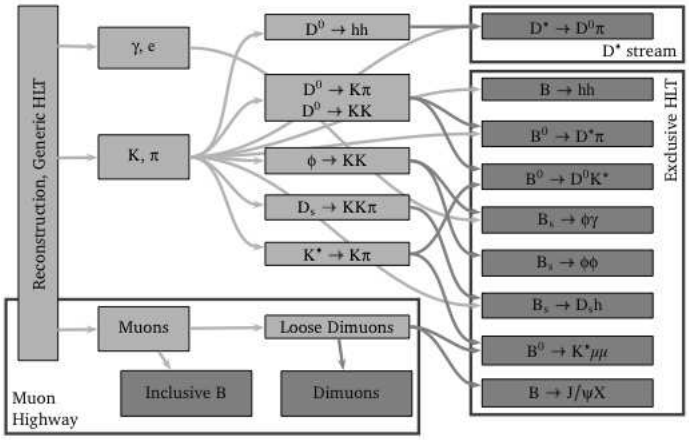

Figure 1.16: Simplified data flow in the HLT.

The main steps of the HLT are described in fig.1.16:

1. **Velo Tracking** The velo R and 3D tracking are performed and the PV is built.

2. **Generic HLT and full tracking** First the veloTT algorithm is run and the muon pattern recognition is made. The forward tracking is done for selected tracks and muons candidates. The errors from the tracking are not used, but recomputed from a parameterization. [3] Events with good muon candidates and heavy dimuons lead to a HLT accept for the inclusive B and dimuon streams. For the others, the generic HLT decision is made looking for separated 2-track vertices of high-PT tracks.

3. **PID and particle making** The `TrgParticleMaker` is executed to make pion and kaon candidates. By default every track is a kaon candidate, but one can use the RICH to refine the selection.

4. **Resonances building** After they pass some loose preselection cuts, these kaons and pions are combined to make K*, D0, Phi and D* intermediate states.

5. **Exclusive selections** Finally the resonances are combined to make Bcandidates for all the 10 core physics channels (see documentation). This step can lead to a HLT accept for the exclusive B or $D*$ streams. The HLT will run at 40 kHz in 10 ms (average) on a 2007 CPU.

[3] (a) *TrgInsertTrackErrParam.opts*

1.3 LHCb performances

In this section I summarize the main performances of the detector related to the recostructing capabilities taking in account the various subdetector information.

1.3.1 The tracking performances

The main task of the tracking system is to provide efficient reconstruction of charged-particle tracks with a precise estimates of the track parameters and their corresponding covariances[4]. In the event reconstruction these estimates are used to match the various information coming from all subdetectors: RICH rings, calorimeter clusters and muon candidates.
The running environment of LHCb will be hadronic, so there will be a great number of tracks per event. The fraction of B mesons produced that decays within the LHCb acceptance is foreseen about the 35%, due to the impossibility of detection up to 10 mrad given rise to the presence of the beam pipe. Also the geometrical acceptance varies according to the kind of decay. In these delicate conditions the track reconstruction will be very challenging.

Every reconstructed track state is a 5-component vector $(x, y, \frac{dx}{dz}, \frac{dy}{dz}, \frac{Q}{p})$, defined by a position and a tangent direction at given z.
Depending on which parts of detector are traversed by the particle flight, each track is classified as (fig.1.17):

In last months this convention has been changed, but in the thesis we will ignore it

- **Long track**: traverse the full tracking setup from the VELO to the T stations. They are the most important set of tracks for Bdecay reconstruction.
- **Upstream track:** traverse only the VELO and TT stations. They are in general lower momentum tracks that do not traverse the magnet. However. they pass through the RICH1 detector and may generate Cherenkov photons. They are therefore used to understand backgrounds in the particle-identification algorithm of the RICH. They may also be used for B decay reconstruction or tagging, although their momentum resolution is rather poor (20%).
- **Downstream track**: traverse only the TT and T stations. The most relevant cases are the decay products of K_s^0 and Λ that decay outside the VELO acceptance.
- **T track**: are only measured in the T stations. They are typically produced in secondary interactions due the conversion of the neutral particles, but useful for the global pattern recognition in RICH2.

[4] A track is defined ghost when less of 70% of its hits are associated to a Monte Carlo particle

- **Velo track**: are measured in the VELO only and are typically large angle or backward tracks, useful for the primary vertex reconstruction. They don't own any measurement for the momentum.

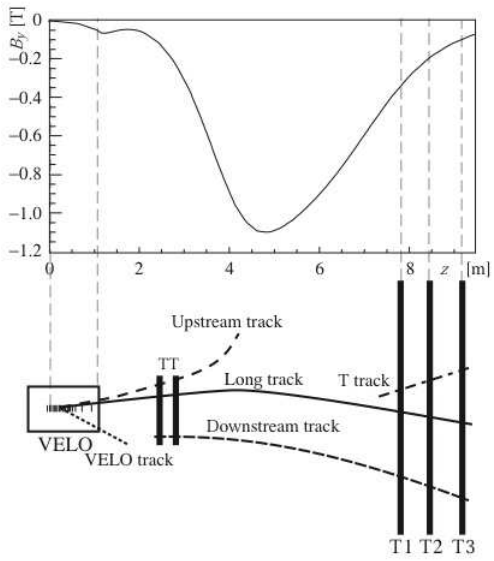

Figure 1.17: Classification of the tracks.

1.3.1.1 The reconstruction method

A track is modeled by a set of straight line segment, tangent to the trajectory of the particle. In LHCb these lines are called *track states*. As seen before, the state vector chosen is:

$$\vec{x} = \begin{pmatrix} x \\ y \\ t_x \\ t_y \\ q/p \end{pmatrix} \quad t_x = \frac{\partial x}{\partial z} \quad t_y = \frac{\partial y}{\partial z} \tag{1.9}$$

and also there is associated a 5×5 covariance matrix. The location of the track states can be chosen anywhere along the trajectory. Usually the states are determined at the measurement planes.

The track reconstruction starts with a search for track "seeds" that are the initial track candidates. The combination of the measurement and the track state is referred to as a *node*. A measurement can be transport from a node to another one. This procedure, called transport, exploits

$$\vec{x}_k = f_k(\vec{x}_{k-1}) + \vec{w}_k \tag{1.10}$$

where k represents the index of a node, f_k is the track propagation function and $\vec{w}_k$ is the process noise as the multiple scattering effects.

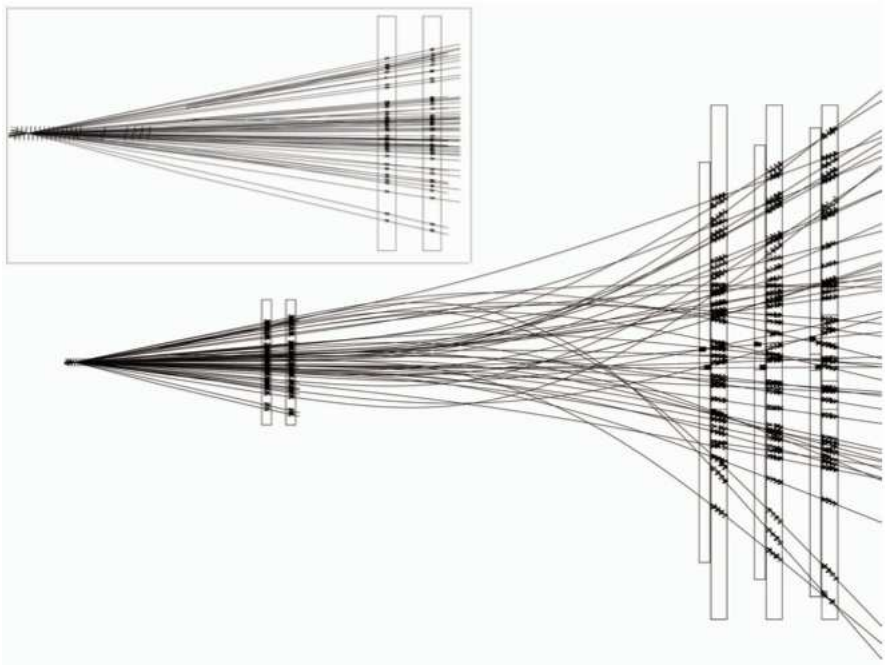

Figure 1.18: Tracking and reconstruction

The VELO and T seeds that have not been used as part of either a long, upstream, or downstream track, are defined to be of type VELO or T track.

The hits used by the forward algorithm are neglected in the hit search of any subsequent algorithm. Moreover the VELO and T seeds that are used by either the forward or track matching algorithm are not considered by the upstream or downstream tracking algorithms. This cooperative strategy, referred to as the *filtered mode*, avoids as much as possible the creation of clone tracks, i.e., tracks which share a large fraction of their hits. The filtered mode is the default tracking strategy.

While, the *concurrent mode* refers to the case in which each algorithm considers all possible hits and seeds. This means, for instance, that the T seeding will also find segments of long tracks that are already found by the forward tracking algorithm.

Thereafter, the track matching algorithm will consider all these VELO and T seeds to find mostly the same tracks as the forward tracking.

In details, starting with a VELO seed, an algorithm runs to form a track

with each of the hits in the following T stations (TT, T1, T2, T3). This is the *forward tracking algorithm* that has an efficiency of reconstruction of about 90%. With an enough number of hit along the trajectory, the track is reconstructed.

The leftover hits are treated in the same way but in opposite direction, starting from T stations to the VELO region. The *backward tracking* has an efficiency of 5%.

Then the algorithm switches to the search of upstream tracks (VELO and TT). The remainder VELO seeds and the T seeds are matched to the TT station hits.

Remaining VELO and T seeds are stored as VELO and T tracks. After that, all found trajectories are refitted by a Kalman filter, in order to determine more precisely the track parameters. The quality of a reconstructed track resides in the $\chi^2$and in the residuals pull distribution of the tracks' parameters.

The track matching algorithm makes combinations of T seeds and VELO seeds in order to fit long tracks. Firstly the momentum of the T seed is estimated. Then the momentum is used to extrapolate the T seed to the matching plane. The VELO tracks are extrapolated with a straight line to the same place. A χ^2criterion is used to select the correct match between the VELO and the T seeds. For every successful match, TT hits are searched for and assigned to the track.

The momentum of a T seed can be estimated assuming that the particle originated from the interaction point. This method, also known as *p-kick* method, involves a basic simplification. It assumes, at first approximation, that all the effects of the B field are concentrated in a single point on $z = z_{magnet}$ in the center of the magnet, where the kick is exerted. The total integrated magnetic field along the z axis is 4.2 Tm and the z_{magnet} is placed where the integrated field is half.

By means of the Lorentz force, the actual momentum kick assumes the form

$$\Delta\vec{p} = q \int d\vec{l} \times \vec{B} \tag{1.11}$$

and in terms of track parameters, for the main component Δp_x, we obtain [11, 10]:

$$\Delta p_x = p_{x,f} - p_{x,i} = p \left(\frac{t_{x,f}}{\sqrt{1 + t_{x,f}^2 + t_{y,f}^2}} - \frac{t_{x,i}}{\sqrt{1 + t_{x,i}^2 + t_{y,i}^2}} \right) = q \int \left| d\vec{l} \times \vec{B} \right|_x \tag{1.12}$$

where $t_{x,f}$ and $t_{y,f}$ are the slopes measured in the T region and $t_{x,i}$ and $t_{y,i}$ are the unknown slopes before the magnet. The trajectory of the particle can be approximated by two intersecting straight lines as illustrated in fig. 1.19. The path starts from the T seed and it is extrapolated to the z_{magnet}. Here the path makes a kink towards the nominal interaction point giving a first estimate of the slope before the magnet. Then along this path, the integrated field is calculated and a second focal plane at $z = z_c$ is determined. The new values

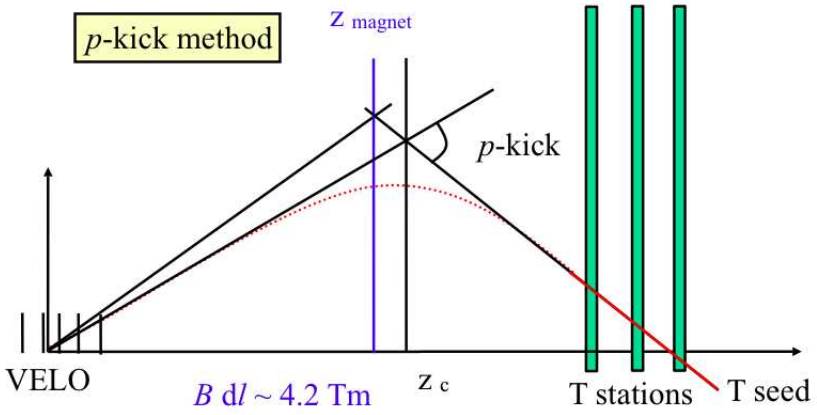

Figure 1.19: The effect of the magnet is approximate by an instant kick at z_{magnet}. Along this trajectory the integrated field is estimated and a new value for the centre of the magnetic field z_c is obtained.

for the slopes before the magnet and the magnetic field value are substituted in the eq.1.12 obtaining an estimation for the momentum p.

From this value of the momentum, the T seeds are extrapolated to a plane placed behind the last VELO station where they are matched to the VELO seeds. In order to select only the combinations that match correctly the T and VELO seeds, a χ^2 cut is applied. At last the TT hits have to be added to each matched track.

The T-tracking algorithm is implemented in C++ code running within the Gaudi software framework[12].

1.3.1.2 Performances of the tracking system and the particle identification

The tracking system is devoted to provide the necessary information for the reconstruction of the charged particles trajectories and their momenta. Tracking performances can be represented by several quantities

- efficiency: that is the probability to correctly reconstruct a particle in the detector acceptance
- ghost rate: that is
- momentum resolution:
- IP resolution

Geometrical acceptance represents a limit for the tracking system since only 35% of the B decay products are contained within the detector. As we have

Decays vs. Mass Resolution $[MeV/c^2]$	**ATLAS**	**CMS**	**LHCb**	
$B_s \to \mu\mu$	80	46	18	
$B_s \to D_s\pi$	43		14	
$B_s \to J/\Psi\phi$ (without J/Ψ mass constraint)	36	32	16	
$B_s \to J/\Psi\phi$ (with J/Ψ mass constraint)	16	13	8	

Table 1.5: Mass resolutions in ATLAS, CMS and LHCb experiments.

already seen one of the greater dangers is the ghost track, i.e. the . For the long tracks we can see the expected ghost rate and efficiency in the figure1.20. However we can state that for B decay the predicted efficiency is greater than the 95%.

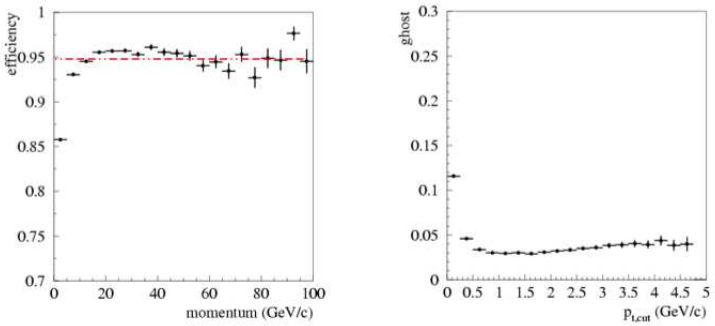

Figure 1.20: Long track performances and ghost rates expressed as the ratios $Efficiency = \frac{\#Correct}{\#True}$ and $Ghost = \frac{\#Ghosts}{\#Ghosts+\$Correct}$.

The figure 1.21 points out the shape of the momentum resolution and the impact track parameter as a function of the momentum. The resolution of the impact parameter can be expressed as a linear function of the transverse momentum p_T :

$$\sigma_{IP} = 14 + \frac{35\,GeV}{p_T}\,\mu m \tag{1.13}$$

The performances of the tracking system also can be summed up observing some other features. The first result is, with any doubt, the excellent mass resolution as shown in tab.1.5. Another critical point is the proper time resolution that is indispensable for all the time dependent B_s measurements (table 1.6).

The particle identification process exploits the information coming from the tracking system. The great discrimination power of pions/kaons is one of the prestigious features of the LHCb detector given by the RICH. In the figure 1.22 is depicted the reconstruction efficiency of kaons in the quark decay chain

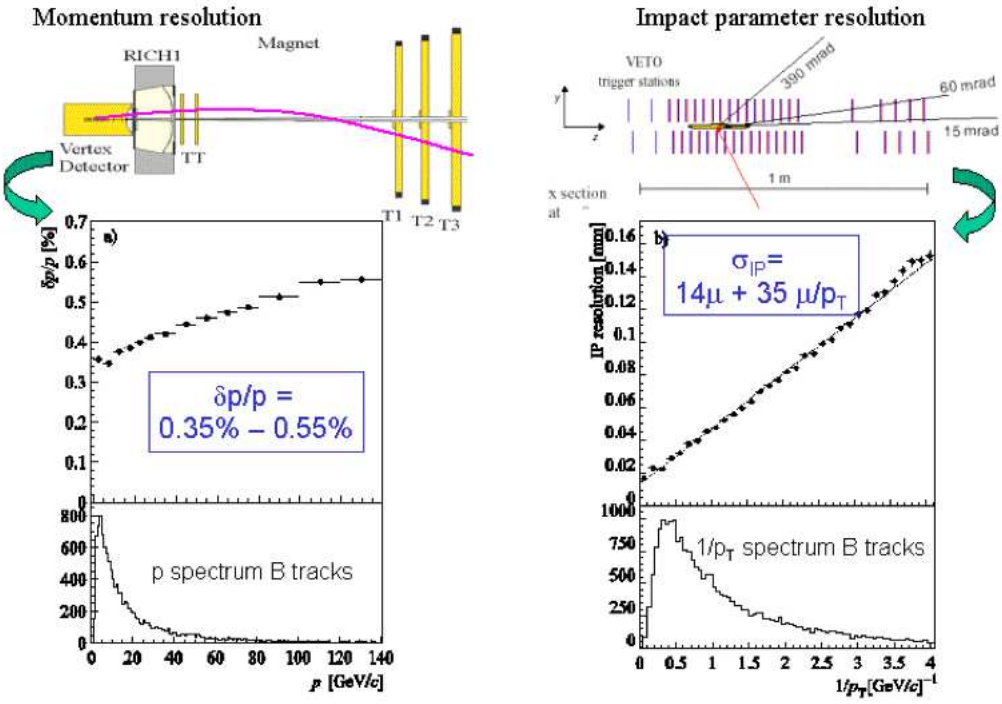

Figure 1.21: Momentum Resolution and its impact parameter as a function of the track momentum.

	$\sigma_{time}[fs]$
ATLAS	~ 95
CMS	~ 100
LHCb	~ 40

Table 1.6: Proper time resolution in the $B_s \to D_s\pi$ at LHC.

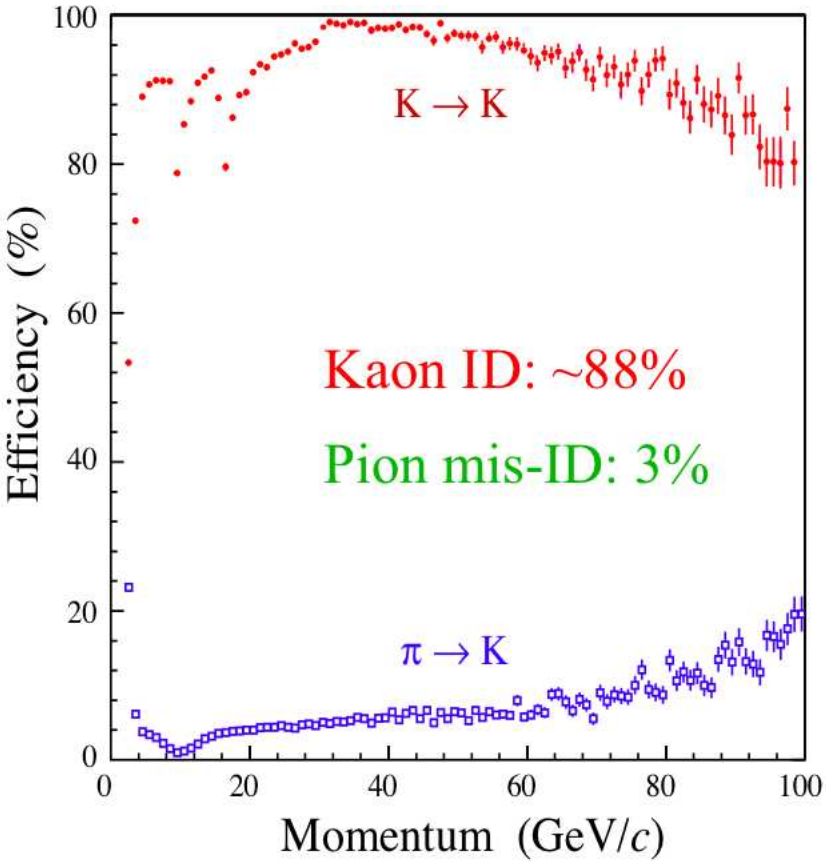

Figure 1.22: Kaon efficiency.

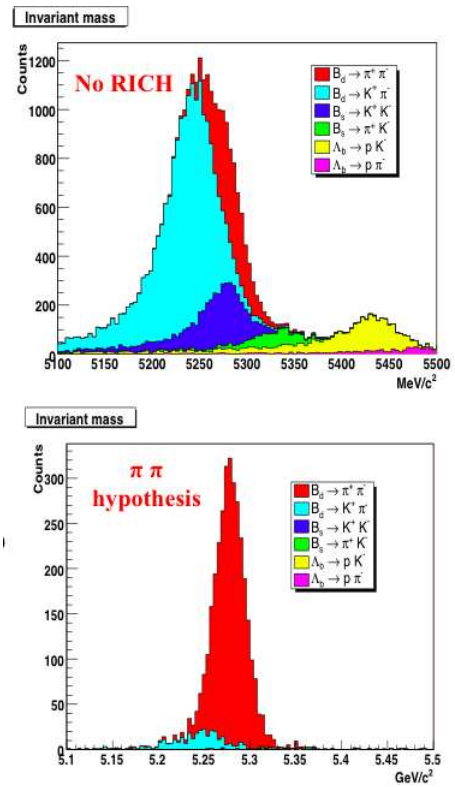

Figure 1.23: The invariant mass in $B_d \to \pi\pi$ hypothesis with or without the RICH.

Hypot.	$\Delta \ln \mathcal{L}$	Efficiency
muon	$\Delta \ln \mathcal{L}(\mu - \pi) < -8$	90%
electron	$\Delta \ln \mathcal{L}(e - \mu) > 0$	95%
kaon	$\Delta \ln \mathcal{L}(K - \pi) > 2, \quad \Delta \ln \mathcal{L}(K - p) > -2$	88%

Table 1.7: $\Delta \ln \mathcal{L}$ for some particle hypothesis

$b \to c \to s$ fundamental in the tagging procedure(par.1.3.2). For kaons, with momentum from 2 to 100 GeV/c, we have an efficiency of 90%.

The electrons are recognized with the ECAL device. The efficiency of the electron identification is about 95% and the mis-identification π/e is nearly 0.7% for the decay $J/\Psi \to e^+e^-$ coming from the B decay $B_d \to J/\Psi K_s$.

Finally the muons efficiency is approximately 94% in a Monte Carlo sample of $B_d \to J/\Psi K_s$ with a mis-identification μ/π nearly 3%.

In practice the particle identification is implemented combining all the information coming from the subdetectors. Every detector provides a particle probability for a certain track. With these hypothesis and probability, a log-likelihood function is computed. For example the probability for an electron is calculated as

$$\mathcal{L}(e) = \mathcal{L}^{RICH}(e) \times \mathcal{L}^{ECAL}(e) \times \mathcal{L}^{MUON}(non - \mu) \tag{1.14}$$

while for a muon

$$\mathcal{L}(\mu) = \mathcal{L}^{RICH}(\mu) \times \mathcal{L}^{ECAL}(non - e) \times \mathcal{L}^{MUON}(\mu) \tag{1.15}$$

Thus the identification is performed evaluating

$$\Delta \ln \mathcal{L}(e - \mu) = \ln[\mathcal{L}(e)/\mathcal{L}(\mu)] \tag{1.16}$$

1.3.2 The B flavour tagging

The B mesons can oscillate and can decay with a different value of flavour. The locution *flavour tagging* means the identification of the initial flavour of the B-mesons reconstructed. This capability is very important in order to study decays involving CP asymmetries and flavour oscillations. The flavour tagging performances is expressed by the formula:

$$\varepsilon_{eff} = \varepsilon_{tag} D^2 = \varepsilon_{tag} \left(1 - 2w\right)^2 \tag{1.17}$$

where the w is the wrong tag fraction whereas the ε_{tag} is the probability that the tagging method retrieves a result:

$$\varepsilon_{tag} = \frac{R + W}{R + W + U} \quad w = \frac{W}{R + W}$$

where W represent the wrong tagged fraction, R the right one and U the untagged fraction.

The tagging algorithm exploits the B decay characteristics. Two main methods are implemented: the *opposite-side tagging* and the *same-side tagging*.

The opposite side tagging determine the characteristics of the b/hadron which accompanies the B/signal under study. by looking at the charge of the decaying lepton in semileptonic decays, or the kaon in b/c/s transitions. In case the opposite B is charged the reconstructed vertex charge tags the event.

The same side tagging algorithms determine directly the flavour of the signal B meson exploiting the correlation in the fragmentation decay chain. The procedure of flavour tagging is implemented by several algorithms, all using long tracks and particle identification for leptons and kaons based on optimized cuts on the combined $\Delta ln\mathcal{L}$ quantities.

Chapter 2

CP violation in B mesons

2.1 Prologue

The CP violation is one of the most astonishing phenomena in particles' physics. In 1957 it was demonstrated that the electroweak interactions are C (charge conjugation) and P (parity) not conserving. For example in the process

$$\pi^+ \to e^+ \nu_{eL} \overset{C}{\longleftrightarrow} \pi^- \to e^- \overline{\nu}_{eL} \overset{P}{\longleftrightarrow} \pi^- \to e^- \overline{\nu}_{eR} \tag{2.1}$$

a $\overline{\nu}_{eL}$ left-handed, never seen in nature, appears after the C transformation. Then, applying the parity, a truly process is obtained therefore the combination of the two operators, CP[1], is conserved this electroweak process.

However in 1964 it was observed in the neutral K kaons decay a plain CP violation. In particular, Christenson, studied the decay $K_L \to \pi^+\pi^-$ and he found out that the mass eigenstates K_s and K_L are not eigenstates for the electroweak Hamiltonian for the $K^0 - \overline{K}^0$. Up to 2001 the CP violation was observed only in the kaon system, but, in the last years it was observed also in the B sector with unambiguous evidences.

2.2 A short introduction: CKM matrix

In the standard model, the electromagnetic and weak interactions are unified into a single electroweak theory accomplished under an $SU(2) \otimes U(1)$ gauge group. This theory is based on spontaneous break (the SBB scheme):

$$SU(2) \otimes U(1)_Y \to SBB \to U(1)_Q$$

The corresponding gauge bosons are the photon of the electromagnetic interaction and the W and Z bosons of the weak force. In the SM, the weak gauge

[1]The CP operation transform a particle in antiparticle trading off their helicity and their momenta. The weak interactions break separately the C and the P symmetry, but they preserve the CP with a good approximation.

bosons get their mass from the spontaneous symmetry breaking of the electroweak symmetry from $SU(2) \times U(1)_Y$ to $U(1)_Q$, caused by the Higgs mechanism, i.e. they obtain their masses in Yukawa couplings to the Higgs field

$$\mathcal{L}_Y = -Y^d_{ij}\overline{Q^I_{Li}}\phi d^I_{Rj} - Y^u_{ij}\overline{Q^I_{Li}}\epsilon\phi^* u^I_{Rj} + h.c. \tag{2.2}$$

where $Y^{u,d}$are 3×3 complex matrices, ϕ is the Higgs field, *i,j* are generation labels and ϵ is the 2×2 antisymmetric tensor. Q^I_L are left-handed quark doublets, and d^I_R and u^I_R are right-handed down and up type quark singlets, respectively, in the weak-eigenstate basis. When the field ϕ acquires a vacuum expectation value, $< \phi >= (0, v/\sqrt{2})$, the lagrangian in eq.2.2 yields mass terms for the quarks. Diagonalizing $Y^{u,d}$ by four unitary matrices, $V^{u,d}_{L,R}$ as

$$M^f_{diag} = V^f_L Y^f V^{f\dagger}_R (v/\sqrt{(2)}) \qquad f = u, d \tag{2.3}$$

the physical states are obtained. As an important result the charged currents $W^\pm$ interactions couple to physical u_{Lj} and d_{Lk} quarks with coupling given by

$$V_{CKM} = V^u_L V^{d\dagger}_L = \begin{pmatrix} V_{ud} & V_{us} & V_{ub} \\ V_{cd} & V_{cs} & V_{cb} \\ V_{td} & V_{ts} & V_{tb} \end{pmatrix}$$

The couplings of the quarks to the Higgs field are not diagonal, for every weak basis. To diagonalize the Yukawa couplings, the CKM matrix has been introduced [8]. The CKM matrix connects the electroweak eigenstates $(d^{'}, s^{'}, b^{'})$ of the down type quarks with their mass eigenstates (d, s, b) through the following unitary transformation:

$$\begin{pmatrix} d^{'} \\ s^{'} \\ b^{'} \end{pmatrix} = \begin{pmatrix} V_{ud} & V_{us} & V_{ub} \\ V_{cd} & V_{cs} & V_{cb} \\ V_{td} & V_{ts} & V_{tb} \end{pmatrix} \begin{pmatrix} d \\ s \\ b \end{pmatrix}$$

In fact for the quarks, the weak flavour eigenstates are different from the mass eigenstates and can be expressed as a superposition of them. By convention, the phases are defined so that the isospin $+1/2$ quarks u, c, t are identical to the mass eigenstates. Therefore the three doublets(weak eigenstates) are:

$$\begin{pmatrix} u \\ d' \end{pmatrix}_L \quad \begin{pmatrix} c \\ s' \end{pmatrix}_L \quad \begin{pmatrix} t \\ b' \end{pmatrix}_L$$

where the d' s' b' are linear superpositions of the mass eigenstates d s b. In the new basis the charged current (CC) interactions mediated by $W^\pm$ bosons are purely left-handed and they are responsible for parity violation. Also, the lack of flavour changing neutral current at the tree level is due to the unitary of the CKM matrix, since the Z_μ interaction terms are now flavour diagonal. The lagrangian that gives a description the interactions between the quarks and the W bosons can be written as

$$\mathcal{L}^{cc}_q = -\frac{g}{\sqrt{2}}\left(J^{cc\dagger}_\mu W_\mu + J^{cc}_\mu W^\dagger_\mu\right) \tag{2.4}$$

where the charged current is

$$J_\mu^{cc} = (\bar{u}\ \bar{c}\ \bar{t})_L\, \gamma_\mu V_{CKM} \begin{pmatrix} d \\ s \\ b \end{pmatrix}_L \tag{2.5}$$

and W_μ describes the vector boson.

Applying the CP operator, the lagrangian

$$CP\mathcal{L}_q^{cc}(CP)^{-1}$$

has the same density if the $V_{CKM} = V_{CKM}^*$, i.e. the CP is conserved only if the elements are real.

However the CPT invariance, which is a more general condition, requires the V_{CKM} unitarity ($V_{CKM} \cdot V_{CKM}^\dagger = I$), thus, with three quark families, complex elements and CP violation are allowed.

The CKM matrix is a $n \times n$ complex matrix, where $n = 3$, so it contains $2n^2$ real numbers. The constraint of unitarity requires

$$\sum_k V_{ik} V_{jk}^* = \delta_{ij}$$

i.e. for the diagonal terms there are N constraints, and for the off diagonal terms there are $n(n-1)$ constraints. In this matrix there are four independent parameters[2]. One of the most popular parametrization for the CKM matrix is the Wolfenstein one:

$$V_{CKM} = \begin{pmatrix} 1 - \frac{\lambda^2}{2} - \frac{\lambda^4}{8} & \lambda & A\lambda^3(\rho - i\eta) \\ -\lambda + \frac{A^2\lambda^5}{2}(1 - 2\rho) - iA^2\lambda^5\eta & 1 - \frac{\lambda^2}{2} - \lambda^4(\frac{1}{8} + \frac{A^2}{2}) & A\lambda^2 \\ A\lambda^3\left[1 - (1 - \frac{\lambda^2}{2})(\rho + i\eta)\right] & -A\lambda^2(1 - \frac{\lambda^2}{2})\left[1 + \lambda^2(\rho + i\eta)\right] & 1 - \frac{A^2\lambda^4}{2} \end{pmatrix} + \mathcal{O}(\lambda^6) \tag{2.6}$$

where the four independent parameters are: A, η, λ, ρ.

The condition of unitarity $V_{CKM}V_{CKM}^\dagger = V_{CKM}^\dagger V_{CKM} = I$ originates 9 vectorial equations which are functions of the four independent parameters. Fatally only two equations are, from an experimentalist point of view, significantly.

$$V_{ud}V_{ub}^* + V_{cd}V_{cb}^* + V_{td}V_{tb}^* = \mathcal{O}(\lambda^3) + \mathcal{O}(\lambda^3) + \mathcal{O}(\lambda^3) = 0 \tag{2.7}$$

$$V_{ud}^*V_{td} + V_{us}^*V_{ts} + V_{ub}^*V_{tb} = \mathcal{O}(\lambda^3) + \mathcal{O}(\lambda^3) + \mathcal{O}(\lambda^3) = 0 \tag{2.8}$$

[2]In a generic $n \times n$ matrix, there are $2n^2$ independent real values. The CKM matrix is also unitary then the number of independent parameters is reduced to n^2. Moreover we have to take account the number $2n$ of the quarks' fields. We can redefine the fields choosing $2n - 1$ arbitrary relative phases. In this case we obtain at last $n^2 - (2n - 1) = (n - 1)^2$.

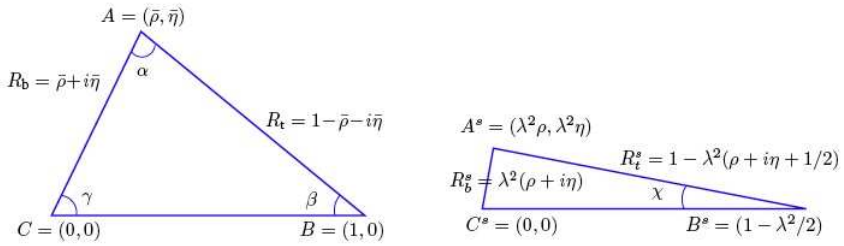

Figure 2.1: Graphical representation, in the complex plane $\overline{\rho}$-$\overline{\eta}$, of the equations 2.7 and 2.8.

For the sake of the simplicity we analyse only the eq.2.7 (see the left picture in fig. 2.1). In the complex plane this equation can be represented as a triangle with the three sides:

$$V_{ud}V_{ub}^* = A\lambda^3(\bar{\rho} + i\bar{\eta})$$

$$V_{cd}V_{cb}^* = -A\lambda^3$$

$$V_{td}V_{tb}^* = A\lambda^3(1 - \bar{\rho} - i\bar{\eta})$$

where the $\bar{\rho} = \rho(1 - \lambda^2/2)$ and $\bar{\eta} = \eta(1 - \lambda^2/2)$. Dividing the three equations by the complex quantity $V_{cd}V_{cb}^*$ we transform the triangle in the plane and the new vertexes are $C(0,0)$ $B(0,1)$ $A(\bar{\rho}, \bar{\eta})$. The sides $\overline{CA}$ and $\overline{AB}$ have length of:

$$\overline{CA} = R_b = \frac{|V_{ud}V_{ub}^*|}{|V_{cd}V_{cb}^*|} = \sqrt{\bar{\rho}^2 + \bar{\eta}^2} = (1 - \lambda^2/2)\frac{1}{\lambda}\frac{|V_{ub}|}{|V_{cb}|} \tag{2.9}$$

$$\overline{AB} = R_t = \frac{|V_{td}V_{tb}^*|}{|V_{cd}V_{cb}^*|} = \sqrt{(1 - \bar{\rho})^2 + \bar{\eta}^2} = \frac{1}{\lambda}\frac{|V_{td}|}{|V_{cb}|} \tag{2.10}$$

The unitarity condition can be at last summarized as

$$R_b e^{-i\gamma} + R_t e^{-i\beta} = 1$$

with

$$\beta = \arg\left(\frac{V_{td}V_{tb}^*}{V_{cd}V_{cb}^*}\right) = \arctan\left(\frac{\bar{\eta}}{1 - \bar{\rho}}\right)$$

$$\gamma = \arg\left(\frac{V_{ud}V_{ub}^*}{V_{cd}V_{cb}^*}\right) = \arctan\left(\frac{\bar{\eta}}{\bar{\rho}}\right)$$

Within the SM, all the physical measurements, depending on the V_{CKM} matrix elements (decay rates, CP asymmetries...), have to be consistent with this complex triangle.

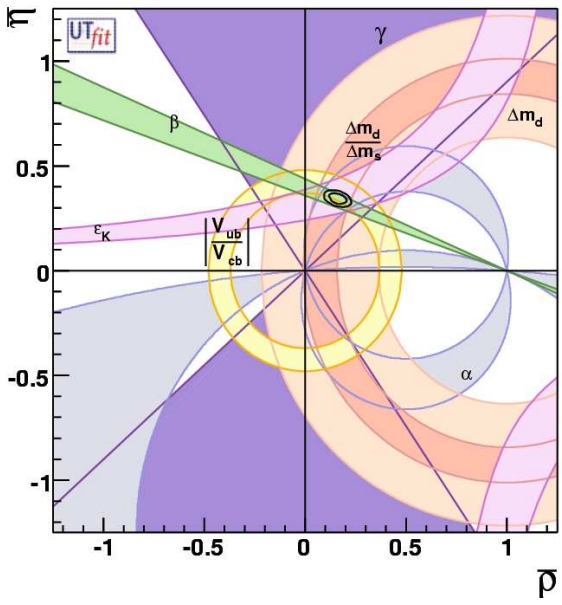

Figure 2.2: Graphical representation of the CKM unitarity triangle, obtained exploiting the present experimental results.

2.2.1 The present knowledge of CKM

The SM validity is addressed to a precise knowledge of the unitary triangle. The combination of the present experimental results are represented in fig. 2.2 obtained by the UTFit group.

Several physical observables contribute to the definition of the CKM picture:

- α $B_d \to \rho\pi$, as well as $B_d^0 \to \pi^+\pi^-$, gives access to $\sin(2\alpha)$ but the second decay requires the knowledge of the "penguin pollution", which can be extracted from $B_d^0 \to K^\pm\pi^\mp$

- β The $B^0/\overline{B}^0$ mixing phase ϕ_d turns out to be equal to 2β and can be extracted from $B_d^0 \to J/\Psi K_s$ and similar channels. $B_d^0 \to \phi K_s$ also allows the measurement of 2β but it is dominated by penguin loops. Both measurements giving different results could show signs of New Physics.

- γ This angle can be accessed by the $B_d^0 \to D^{(*)}\pi$ channels, which give $\gamma + \phi_d$ obtained from the measurement described above. There is also the $B_s^0 \to D_s K$ channel, which is sensitive to $\gamma + !\phi_s$.

- χ This angle can be estimated with the B_s mixing phase, ϕ_s, which is equal to -2χ in the SM and can be extracted from asymmetries in $B_s^0 \to J/\Psi\phi, B_s^0 \to J/\Psi\eta, B_s^0 \to \eta_c\phi$ or $B_s^0 \to J/\Psi\eta^{'}$

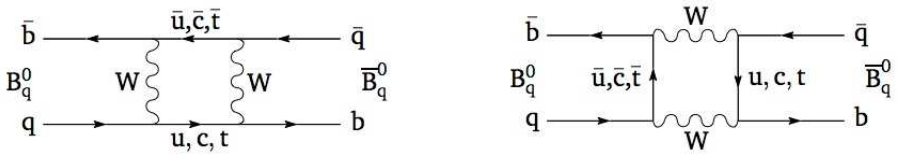

Figure 2.3: Box Diagrams illustrating the $B_q/\overline{B}_q$ mixing.

- $|R_b|$ This is the length of the CA side of the unitarity triangle (**db**) which involves the ratio$|V_{ub}|/|V_{cb}|$. Both the numerator and the denominator can be obtained via semileptonic decays of B-mesons, e.g. $b \to ul\overline{\nu}$ or $b \to ucl\overline{\nu}$ decay processes.
- $|R_t|$ This is the length of the AB side of the unitarity triangle (**db**), $|Rt| = \frac{1}{\lambda}\frac{|V_{td}|}{|V_{cd}|}$, where the problematic term is V_{td}. However it can be determined with the help of the mass difference $\Delta m_{d,s}$ of the mass eigenstates of the neutral B_d and B_s meson systems with $\frac{\Delta m_s}{\Delta m_d} = \frac{m_{B_s}}{m_{B_d}}\epsilon^2\frac{|V_{ts}|^2}{|V_{td}|^2}$ where ϵ (of order unity) expresses hadronic structure functions. More specifically the ratio $\Delta m_s/\Delta m_d$is independent of m_t and short distance QCD corrections. In principle, this ratio is affected by much smaller theoretical uncertainties than the hadronic matrix elements appearing in Δm_s and Δm_dseparately. The determination of $|V_{td}/|V_{ts}|$ can also be done with rare decays through $b \to$ transitions.

Up to now the experimental results show an agreement with the SM theoretical framework. A more precise determination of the sides and the angles of the unitarity triangle can show up inconsistencies due to NP effects.

2.3 The Particle-antiParticle system

The neutral B_q mesons (bound states of $\bar{b}q$ quarks) can oscillate and decay (fig. 2.3). They decay through electroweak processes ($\Delta B = 1$) , while they can oscillate to its antiparticles via flavour violation transitions ($\Delta B = 2$).

The time evolution of a particle-antiparticle system $P^0 \leftrightarrow \bar{P}^0$ is defined with a vector in the Hilbert space:

$$|\Psi(t)\rangle = a(t)\left|P^0\right\rangle + b(t)\left|\bar{P}^0\right\rangle + \sum_i |f\rangle \tag{2.11}$$

according to the Schroedinger equation:

$$i\hbar\frac{\partial}{\partial t}|\Psi\rangle = \mathcal{H}|\Psi\rangle \tag{2.12}$$

where H is an infinite-dimensional Hermitian matrix in the Hilbert space and it describes the electro-weak and the strong interactions:

$$\mathcal{H} = \mathcal{H}_{weak} + \mathcal{H}_{strong} + \mathcal{H}_{em} \tag{2.13}$$

. To treat in some ways this equation, we need to make some assumptions.

1. The initial state is a linear combination of P^0 and $\bar{P^0}$
2. We analize only the coefficient $a(t)$ and $b(t)$.
3. We use the WeissKopf-Wigner[3] approximation[14]
   we obtain a new matricial equation:

$$\mathcal{H} = \mathbf{M} - \frac{i}{2}\mathbf{\Gamma} = \begin{pmatrix} m_{11} - \frac{i}{2}\Gamma_{11} & m_{12} - \frac{i}{2}\Gamma_{12} \\ m_{21} - \frac{i}{2}\Gamma_{21} & m_{22} - \frac{i}{2}\Gamma_{22} \end{pmatrix} \tag{2.14}$$

Assuming the CPT invariance, considerable simplifications arise from $\mathcal{H} = \mathcal{H}^\dagger$. To find the solutions we diagonalize H and solve eq.2.12. The two states are

$$\begin{array}{l} |P_1\rangle = p\left|P^0\right\rangle + q\left|\bar{P}^0\right\rangle \\ |P_2\rangle = p\left|P^0\right\rangle - q\left|\bar{P}^0\right\rangle \end{array} \tag{2.15}$$

are the mass eigenstates with eigenvalues:

$$\begin{array}{l} m_1 - \frac{i}{2}\Gamma_1 = m_{11} - \frac{i}{2}\Gamma_{11} + \frac{q}{p}\left(m_{12} - \frac{i}{2}\Gamma_{12}\right) \\ m_2 - \frac{i}{2}\Gamma_2 = m_{11} - \frac{i}{2}\Gamma_{11} - \frac{q}{p}\left(m_{12} - \frac{i}{2}\Gamma_{12}\right) \end{array} \tag{2.16}$$

with

$$\left(\frac{q}{p}\right)^2 = \frac{m_{12}^* - \frac{i}{2}\Gamma_{12}^*}{m_{12} - \frac{i}{2}\Gamma_{12}} \tag{2.17}$$

The two mass eigenstates have different masses and widths which depend on the off diagonal elements of the matrix H (eq.2.14):

$$\Delta m = m_2 - m_1 = -2Re\left(\frac{q}{p}\left(m_{12} - \frac{i}{2}\Gamma_{12}\right)\right) \tag{2.18}$$

$$-\Delta\Gamma = \Gamma_2 - \Gamma_1 = 4Im\left(\frac{q}{p}\left(m_{12} - \frac{i}{2}\Gamma_{12}\right)\right) \tag{2.19}$$

While we can observe that p and q terms are bound by the normalization

[3]We can make use of the WeissKopt-Wigner approximation, namely given the times t in which we are interested are much larger than the typical strong interaction scale, we can neglect the weak interactions between the final states, i.e. we simply set $\langle f_i|\,\mathcal{H}_{weak}\,\left|f_{i'}\right\rangle = 0$.

	B_d	B_s
mass[MeV/c^2]	5279.3 ± 0.7	5369.6 ± 2.4
Γ[ps]	1.530 ± 0.009	1.466 ± 0.059
Δm[ps^{-1}]	0.507 ± 0.005	17.77 ± 0.69
$\Delta\Gamma/\Gamma$	0.009 ± 0.037	$0.31^{+0.11}_{-0.13}$

Table 2.1: Main differences between the B_d and B_s systems.

condition

$$|p|^2 + |q|^2 = 1 \tag{2.20}$$

The assignment of the the labels 1 and 2 is an arbitrary choice, with no physical meaning. In the case of the B_d mesons the lifetime difference is too small to be observed, so the classification is made observing which one is heavier. Therefore the mass difference is defined as

$$\Delta m \equiv m_H - m_L > 0 \tag{2.21}$$

whereas the lifetime difference is

$$\Delta\Gamma = \Gamma_H - \Gamma_L < 0 \tag{2.22}$$

A comparison of the present knowledge of the B_d and B_s properties are reported in tab.2.1. We can notice that the B_s have a higher oscillation frequency Δm and a bigger $\Delta\Gamma$.

The time evolution of the mass eigenstates is ruled by these equations:

$$\left|B_j^0(t)\right\rangle = e^{-im_j t} e^{-\frac{\Gamma}{2}_j t} \left|B_j^0\right\rangle, \;\; j = H, L \tag{2.23}$$

so due to the mixing they become (2.16) the general time evolution formulas:

$$\left|B_q{}^0(t)\right\rangle = e^{-im_q} e^{-\frac{\Gamma_q t}{2}} \left[\cos\left(\frac{\Delta m_q}{2}t\right)\left|B_q^0\right\rangle + i\frac{p}{q}\sin\left(\frac{\Delta m_q}{2}t\right)\left|\bar{B}_q^0\right\rangle\right] \tag{2.24}$$

$$\left|\bar{B}_q^0(t)\right\rangle = e^{-im_q} e^{-\frac{\Gamma_q t}{2}} \left[\cos\left(\frac{\Delta m_q}{2}t\right)\left|\bar{B}_q^0\right\rangle + i\frac{p}{q}\sin\left(\frac{\Delta m_q}{2}t\right)\left|B_q^0\right\rangle\right] \tag{2.25}$$

2.3.1 Time dependent decay rates

Let us consider a specific decay of the neutral $B_q/\overline{B}_q$ mesons to final states $f/\overline{f}$.

The transition amplitudes are expressed by the following relations:

$$A_f \equiv \left|\left\langle f\left|T\right|B_q^0\right\rangle\right|, \;\; A_{\bar{f}} \equiv \left|\left\langle \bar{f}\left|T\right|B_q^0\right\rangle\right|$$

$$\bar{A}_f \equiv \left|\left\langle f\left|T\right|\bar{B}_q^0\right\rangle\right|, \;\; \bar{A}_{\bar{f}} \equiv \left|\left\langle \bar{f}\left|T\right|\bar{B}_q^0\right\rangle\right|$$

where $|f\rangle$ is the generic final state. In the next paragraph we will see how the decay amplitudes can be computed within the SM considering all the possible hadronic contributions. The relevant fact is that the previous transition amplitudes depend on the CKM elements.

From the eq.2.25 and the eq.2.24 we can calculate the time dependent decay rates. For an initial $\left|B_q^0\right\rangle$ meson is:

$$A\left[B_q^0(t)\to f\right] = \left|\left\langle f\left|T\right|B_q^0\right\rangle\right| = e^{-im_q t}e^{-\frac{\Gamma_q t}{2}}\left[\cos\left(\frac{\Delta m_q}{2}t\right)A_f + i\frac{p}{q}\sin\left(\frac{\Delta m_q}{2}t\right)\bar{A}_f\right] \tag{2.26}$$

likewise, for a meson that borns as$\left|\bar{B}_q^0\right\rangle$, the decay amplitude is:

$$A\left[\bar{B}_q^0(t)\to f\right] = \left|\left\langle f\left|T\right|\bar{B}_q^0\right\rangle\right| = e^{-im_q t}e^{-\frac{\Gamma_q t}{2}}\left[\cos\left(\frac{\Delta m_q}{2}t\right)\bar{A}_f + i\frac{p}{q}\sin\left(\frac{\Delta m_q}{2}t\right)A_f\right] \tag{2.27}$$

If $f \neq \overline{f}$ we have four different decay rates:

$$\Gamma\left(B_q^0(t)\to f\right) = \frac{\left|A_f\right|^2}{2}e^{-\Gamma t}\left[I_+(t) + I_-(t)\right] \tag{2.28}$$

$$\Gamma\left(B_q^0(t)\to \bar{f}\right) = \frac{\left|\bar{A}_{\bar{f}}\right|^2}{2}\left|\frac{p}{q}\right|^2 e^{-\Gamma t}\left[\bar{I}_+(t) - \bar{I}_-(t)\right] \tag{2.29}$$

$$\Gamma\left(\bar{B}_q^0(t)\to f\right) = \frac{\left|A_f\right|^2}{2}\left|\frac{p}{q}\right|^2 e^{-\Gamma t}\left[I_+(t) - I_-(t)\right] \tag{2.30}$$

$$\Gamma\left(\bar{B}_q^0(t)\to \bar{f}\right) = \frac{\left|\bar{A}_{\bar{f}}\right|^2}{2}e^{-\Gamma t}\left[\bar{I}_+(t) - \bar{I}_-(t)\right] \tag{2.31}$$

with

$$I_+(t) = \left(1+\left|\lambda_f\right|^2\right)\cosh\frac{\Delta\Gamma}{2}t - 2\mathrm{Re}(\lambda_f)\sinh\frac{\Delta\Gamma}{2}t \tag{2.32}$$

$$I_-(t) = \left(1+\left|\lambda_f\right|^2\right)\cos\Delta m t - 2\mathrm{Im}(\lambda_f)\sin\Delta m t \tag{2.33}$$

$$\bar{I}_+(t) = \left(1+\left|\bar{\lambda}_{\bar{f}}\right|^2\right)\cosh\frac{\Delta\Gamma}{2}t - 2\mathrm{Re}(\bar{\lambda}_{\bar{f}})\sinh\frac{\Delta\Gamma}{2}t \tag{2.34}$$

$$\bar{I}_-(t) = \left(1+\left|\bar{\lambda}_{\bar{f}}\right|^2\right)\cos\Delta m t - 2\mathrm{Im}(\bar{\lambda}_{\bar{f}})\sin\Delta m t \tag{2.35}$$

$$\lambda_f \equiv \frac{p}{q}\frac{\bar{A}_f}{A_f} \quad \bar{\lambda}_{\bar{f}} \equiv \frac{p}{q}\frac{A_{\bar{f}}}{\bar{A}_{\bar{f}}} \tag{2.36}$$

2.3.2 Classification of CP violation (CPV)

Depending on the decay considered, three possible mechanisms can lead to a CP violation.

1. CP Violation in the mixing
2. CP Violation in the decay
3. CP Violation in the interference of mixing and decay

Since the amplitude phase is convention dependent, any CPV can be manifested if at least two amplitudes with different CP behaviors interfere.

CP violation in mixing This CPV in mixing is originated by

$$|p/q| \neq 1 \tag{2.37}$$

that implies that the probability for initial pure B_q to decay as B_q or initial $\overline{B}_q$to decay as $\overline{B}_q$, at time t are different.

This CPV can be well isolated in semileptonic decays of neutral B:

$$\frac{\Gamma(\bar{B}^0(t) \to l^+\nu X) - \Gamma(B^0(t) \to l^-\bar{\nu}X)}{\Gamma(\bar{B}^0(t) \to l^+\nu X) + \Gamma(B^0(t) \to l^-\bar{\nu}X)} = \frac{1-|q/p|^4}{1+|q/p|^4} = Im\frac{\Gamma_{12}}{M_{12}} \tag{2.38}$$

even if this asymmetry can be measured, since the M_{12} and Γ_{12} are affected by large hadronic uncertainties, no precise extraction of CKM parameters can be performed from this type of decays.

CP violation in decay(or direct) This kind of CPV borns from when the two amplitudes which are different. As shown in the following equations, they depend on the strong δ_k and the weak phases ϕ_k :

$$\bar{A}_{f^-} = \left\langle f^- \right| \mathcal{H}_{weak} \left| B^- \right\rangle = \sum_{k=1,2} A_k e^{i(\delta_k - \phi_k)} \tag{2.39}$$

$$A_{f^+} = \left\langle f^+ \right| \mathcal{H}_{weak} \left| B^+ \right\rangle = \sum_{k=1,2} A_k e^{i(\delta_k + \phi_k)} \tag{2.40}$$

This CPV can be best isolated in charged B decays since mixing effects do not enter in this process. The asymmetry is given by

$$A_{CP}^{Dir}(B^{\pm} \to f^{\pm}) = \frac{\Gamma(B^+ \to f^+) - \Gamma(B^- \to f^-)}{\Gamma(B^+ \to f^+) + \Gamma(B^- \to f^-)} = \frac{1 - |\bar{A}_{f^-}/A_{f^+}|^2}{1 + |\bar{A}_{f^-}/A_{f^+}|^2} \quad (2.41)$$

This asymmetry is non zero if there is weak or a strong phase difference, hence

$$A_{CP}^{Dir} = \frac{-2A_1A_2\sin(\delta_1 - \delta_2)\sin(\phi_1 - \phi_2)}{A_1^2 + A_2^2 + 2A_1A_2\cos(\delta_1 - \delta_2)\cos(\phi_1 - \phi_2)} \quad (2.42)$$

The sign of strong phases δ_k are the same because CP is conserved by strong interactions. The weak phases, instead, have opposite signs.

CP violation in the interference and in the decay This type of CPV can be observed only in neutral B meson decays to CP eigenstates ($f \equiv \overline{f}$) when $Im(\lambda_f) \neq 0$. This CP violation can be turn out as well in absence of direct CPV with $|p/q| = 1$ since

$$|\lambda_f| = \left|\frac{p \cdot \bar{A}_f}{q \cdot A_f}\right| = 1 \quad (2.43)$$

It contains aspects of both direct and indirect CP violation. In fact, in this case, the CPV is originated from the interference of a decay with mixing a decay without.

2.4 Theoretical Framework

The CP asymmetries, shown in the previous paragraph, represent a valid tools to evaluate the CPV within the SM. Unfortunately the hadronic uncertainties of the decay transition limit the accuracy of the measurements of the CKM elements. In some cases they even prevent any estimate. However a theoretical tool exists and it can be employed with profit. The most complicated b-hadron decays are non-leptonic transitions, that are mediated by $b \to q_1\overline{q}_2 d(s)$ with $q_1, q_2 \in \{u, c\}$ and $q_1, q_2 \in \{d, s\}$.

The starting point for the study of the weak decays of hadrons is the effective weak Hamiltonian which has the following generic structure [26]:

$$\mathcal{H}_{eff} = \frac{G_F}{\sqrt{2}} \sum_i V^i_{CKM} C_i(\mu) Q_i \tag{2.44}$$

where the G_F is the Fermi constant and the Q_i are the relevant local operators which control the decays. The Wilson coefficients C_i and the CKM elements describe the strength of each local operator Q_i. The simplest decay that we can analize is the beta decay:

$$\mathcal{H}^{\beta}_{eff} = \frac{G_F}{\sqrt{2}} \cos\theta_c \, [\overline{u}\gamma_\mu(1-\gamma_5)d \otimes \overline{e}\gamma^\mu \nu_e] \tag{2.45}$$

where V_{ud} has been expressed in terms of $\cos\theta_c$. In this case the Wilson coefficient is equal to unity and the local operator Q_i is the term between the brackets given by a two $V-A$ currents product. In this context the formula 2.44 can be regarded as a generalization of of the Fermi Theory to include all quarks and leptons. Thus the effective hamiltonian can be thought as a simply series, known also the operator product expansion (OPE), of effective vertexes multiplied by effective coupling constants C_i.

Likewise the transition amplitudes for non-leptonic decays are calculated using low energy effective Hamiltonian which are expressed using OPE which factorizes QCD and weak effects. The OPE technique allows to separate the short distance contributions C_i from the long distance contributions Q_i. The coefficient $C_i(\mu)$ are the scale dependent couplings of the hadronic matrix elements $\langle f|Q_i(\mu)|i\rangle$ and they are perturbative quantities. The short distance part contains the information on the integrated heavy fields which are treated as dynamical degrees of freedom.
For the B decays there are six classes of hadronic operators, as reported in fig.2.4:

Current-Current (Tree processes)

$$Q_1 = (\bar{c}_\alpha b_\beta)_{V-A}(\bar{s}_\beta c_\alpha)_{V-A} \qquad Q_2 = (\bar{c}b)_{V-A}(\bar{s}c)_{V-A} \tag{2.46}$$

QCD Penguins

$$Q_3 = (\bar{s}b)_{V-A} \textstyle\sum_{q=u,d,s,c,b}(\bar{q}q)_{V-A} \qquad Q_4 = (\bar{s}_\alpha b_\beta)_{V-A} \textstyle\sum_{q=u,d,s,c,b}(\bar{q}_\beta q_\alpha)_{V-A} \tag{2.47}$$

$$Q_5 = (\bar{s}b)_{V-A} \sum_{q=u,d,s,c,b} (\bar{q}q)_{V+A} \qquad Q_6 = (\bar{s}_\alpha b_\beta)_{V-A} \sum_{q=u,d,s,c,b} (\bar{q}_\beta q_\alpha)_{V+A} \tag{2.48}$$

Electroweak Penguins

$$Q_7 = \tfrac{3}{2}(\bar{s}b)_{V-A} \sum_{q=u,d,s,c,b} e_q (\bar{q}q)_{V+A} \qquad Q_8 = \tfrac{3}{2}(\bar{s}_\alpha b_\beta)_{V-A} \sum_{q=u,d,s,c,b} e_q (\bar{q}_\beta q_\alpha)_{V+A} \tag{2.49}$$

$$Q_9 = \tfrac{3}{2}(\bar{s}b)_{V-A} \sum_{q=u,d,s,c,b} e_q (\bar{q}q)_{V-A} \qquad Q_{10} = \tfrac{3}{2}(\bar{s}_\alpha b_\beta)_{V-A} \sum_{q=u,d,s,c,b} e_q (\bar{q}_\beta q_\alpha)_{V-A} \tag{2.50}$$

Magnetic Penguins

$$Q_{7\gamma} = \tfrac{e}{8\pi^2} m_b \bar{s}_\alpha \sigma^{\mu\nu} (1+\gamma_5) b_\alpha F_{\mu\nu} \qquad Q_{8G} = \tfrac{e}{8\pi^2} m_b \bar{s}_\alpha \sigma^{\mu\nu} (1+\gamma_5) T^a_{\alpha\beta} b_\alpha G^a_{\mu\nu} \tag{2.51}$$

$\Delta S = 2$ and $\Delta B = 2$ Operators

$$Q(\Delta S = 2) = (\bar{s}d)_{V-A} (\bar{s}d)_{V-A} \qquad Q(\Delta B = 2) = (\bar{b}d)_{V-A} (\bar{b}d)_{V-A} \tag{2.52}$$

Semileptonic Operators

$$Q_{9V} = (\bar{s}b)_{V-A} (\mu\bar{\mu})_V \qquad Q_{10A} = (\bar{s}b)_{V-A} (\mu\bar{\mu})_A \tag{2.53}$$

$$Q_{\bar{\nu}\nu} = (\bar{s}b)_{V-A} (\bar{\nu}\nu)_{V-A} \qquad Q_{\bar{\mu}\mu} = (\bar{s}b)_{V-A} (\bar{\mu}\mu)_{V-A} \tag{2.54}$$

The Wilson coefficients $C_i(\mu)$ depend on the energy scale μ. They express the physics contributions from scales higher than μ and due to the asymptotically freedom of QCD; they can be calculated in perturbation theory as long as μ is not too small. C_i include the contributions from heavy particles such as W, Z bosons, top quark and also from the supersymmetric particles in the supersymmetric extension of the SM. For this reason the Wilson coefficients depend generally on m_t and also on the masses of new particles, if extensions of SM are considered. An amplitude for a decay of a given meson M into a final state F is expressed

$$A(M \to F) = \langle F | \mathcal{H}_{eff} | M \rangle = \frac{G_F}{\sqrt{2}} \sum V^i_{CKM} C_i(\mu) \langle F | Q_i(\mu) | M \rangle \tag{2.55}$$

The μ value can be chosen arbitrarily and it achieves the separation of the physics contributions to a given decay amplitude into short-distance contributions, at scales higher than μ, and long-distance contributions, corresponding to scales lower than μ. Usually μ is chosen at the scale mass of the decaying hadron.

So the most important feature of the OPE is, without any doubts, the possibility to separate the amplitude in two distinct parts: the short distance (perturbative) $C_i(\mu)$ and the long-distance (generally non-perturbative) calculation of the matrix elements$\langle Q_i(\mu) \rangle$. These ones involve long distance, no perturbative contributions, so we have to employ some non-perturbative method such

as lattice calculations, QCD sum rules, the 1/N expansion and so on. Anyway these approximations have some limitations. Without a reliable estimate of these elements, we cannot determine accurately the CKM matrix in order to observe some hints of new physics, beyond the SM.

The formula 2.55 can be transformed in a more intuitive master formula for the weak decays amplitudes in the SM:

$$A(Decay) = \sum_i B_i \eta^i_{QCD} V^i_{CKM} F_i(x_t) \tag{2.56}$$

where $x_t = m_t^2/M_W^2$. The B_i are the matrix elements, non perturbative, of local operators and the η_{QCD} are the QCD factors from the RG-analysis. The $F_i(x_t)$ are the Inami-Lim functions and they are from the calculation of the box and penguin diagrams in the SM. The most likely B meson decays are the semileptonic and hadronic decays.
The above formula can be modified to contain the new physics models:

$$A(Decay) = \sum_i B_i \eta^i_{QCD} V^i_{CKM} [F^i_{SM} + F^i_{new}] + \sum_k B^{New}_k [\eta^k_{QCD}] V^k_{New} [G^k_{New}] \tag{2.57}$$

New physics can contribute to the master formula in two ways. It can modify the role of an operator, present already in SM, summing a new short distance functions F^i_{New} that depend on on the new parameters in the SM extension (for example the masses of charginos and squarks).

Also there is a second way that is described by the second term of eq. 2.57 where the matrix V^i_{New} describes new sources of flavour and CP violation beyond the CKM matrix.

2.4.1 Classification of elementary processes

Non leptonic B decays can be thought as a combination of the tree and the penguin diagrams. We can have:

$$b \to q_1 \bar{q}_2 d(s) \qquad b \to q \bar{q} d(s)$$

for the tree and the penguin diagrams. We can divide the transitions in three classes:

- both tree and penguin diagrams are involved. $q_1 = q_2 = q = u, c$

$$b \to c\bar{c}s \qquad b \to c\bar{c}d \quad b \to u\bar{u}s \qquad b \to u\bar{u}d \tag{2.58}$$

- only tree diagrams are present. $q_1 \neq q_2 \in \{c, u\}$

$$b \to c\bar{u}s \qquad b \to c\bar{u}d \quad b \to u\bar{c}s \qquad b \to u\bar{c}d \tag{2.59}$$

- only the penguin diagrams contribute. $q = d$:

$$b \to s\bar{s}s \qquad b \to s\bar{s}d \quad b \to d\bar{d}s \qquad b \to d\bar{d}d \tag{2.60}$$

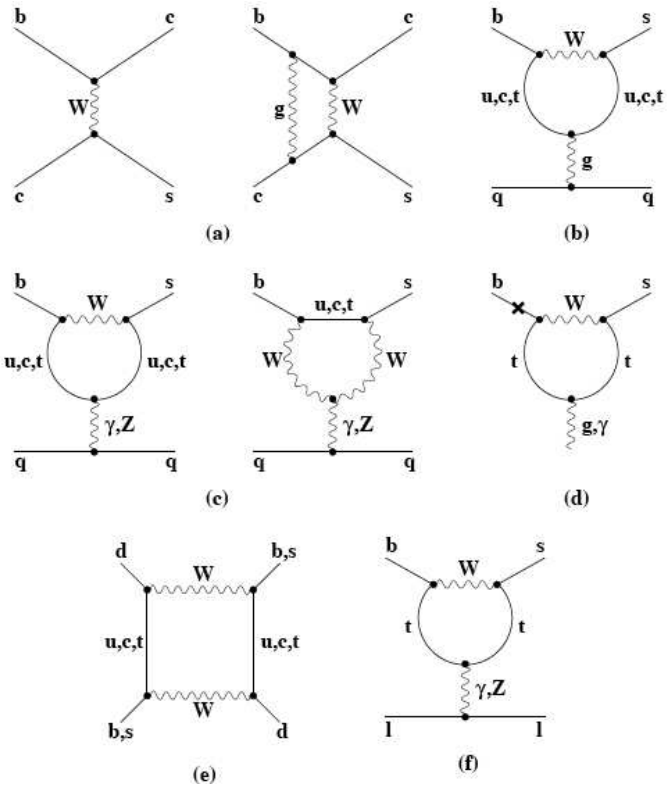

Figure 2.4: Typical penguin and box diagrams:(a) Current-Current; (b) QCD Penguins; (c) Electroweak Penguins; (d) Magnetic Penguins; (e) Box Diagram; (f) Semileptonic Operators

2.5 LHCb Physics program

LHCb can fully exploit the large$B$ meson yields at LHC from the start up with an excellent mass and decay time resolution and particle ID. Also it will have a flexible and robust trigger dedicated to B physics. In next lines I would like to list the main physics tasks that LHCb is going to face.

2.5.1 Δm_s , $\Delta\Gamma_s$ and γ extraction from $B_s \to D_s\pi$

The frequency of the B mesons oscillations is determined by the Δm value. The frequency has different values for the B_s and the B_d systems (tab. 2.1).
One of the first target that LHCb will accomplish, it will be the Δm_s extraction from the $B_s \to D_s\pi$. We foresee about $80,000$ events in one year of data taken ($2\,\mathrm{fb}^{-1}$). For details see the par. 4.4.2.3. The study of this channel also it will provide the CP angle $\gamma+\phi_s$ and the $\Delta\Gamma_s$ value. The angle ϕ_s is an unmeasured quantity that will be retrieved by the $B_s \to J/\Psi\phi$ and the $B_s \to J/\Psi\eta$ channels, so in this way the angle γ will be determined. Since the decay originates from tree diagram processes, the γ measurement is not affected from the presence of new particles. A second way to reach the γ angle is described in the next paragraph.

2.5.2 $B \to h^+h^-$ for γ extraction

Fleischer, following[28], we apply the U-spin symmetry in order to extract the γ angle. We analise the behavior of the decay channels $B_{d(s)} \to h^+h^{'-}$ where $h, h^{'} = \pi, K$. From these decays the extraction of the CKM phases should be rather complicated due the hadronic uncertainties coming from the penguin pollution, but the U-spin symmetry can lead to a plain reduction. The strategy is only limited by theoretical uncertainties introduced by the U-spin breaking corrections [**?**].

Folding in the information coming from the different h^+h^- cases, we can state that:

$$C\left(B_d^0 \to \pi\pi\right) = f_1\left(d, \theta, \gamma\right)$$
$$S\left(B_d^0 \to \pi\pi\right) = f_2\left(d, \theta, \gamma, \phi_d\right)$$
$$C\left(B_s^0 \to KK\right) = f_3\left(d', \theta', \gamma\right)$$
$$S\left(B_s^0 \to KK\right) = f_4\left(d', \theta', \gamma, \phi_s\right)$$

where

$$C_f = \frac{1-|\lambda_f|^2}{1+|\lambda_f|^2} \quad \lambda_f = \frac{q}{p}\frac{\overline{A}_f}{A_f} \tag{2.61}$$

and

$$S_f = 2\frac{\mathrm{Im}\lambda_f}{1+|\lambda_f|^2} \tag{2.62}$$

and the index f represents the final states $\pi\pi$ and KK. So there are 4 equations with 7 unknowns. The mixing phases can be extracted from the $B_d \to J/\Psi K_s$

and $B_s \to J/\Psi\phi$ and, relying on Uspin symmetry we can eliminate two further unknowns. Four equation for 3 unknowns.

Also the $B^0 \to K^+\pi^-$ and $B_s^0 \to \pi^+K^-$ decays differ only in the spectator quarks from the $B_s^0 \to K^+K^-$ and $B^0 \to \pi\pi$ channels. So we can assume

$$\mathcal{A}_{KK}^{dir} \simeq \mathcal{A}_{K\pi} \tag{2.63}$$

$$\mathcal{A}_{\pi\pi}^{dir} \simeq \mathcal{A}_{\pi K} \tag{2.64}$$

where $\mathcal{A}_{K\pi}$ is the charge asymmetry for the $B^0 \to K^+\pi^-$ and $\mathcal{A}_{\pi K}$ is the charge asymmetry for $B_s^0 \to \pi^+K^-$.

Effects of new Physics can be revealed by the extraction of γ observing the large sample of $B \to h^+h^-$ thanks to the great PID and vertexing capabilities of LHCb detector.

2.5.3 $B^\pm \to D_{CP}^0 K^\pm$ for γ, the GLW method

The γ measurement in charged B decays exploits the interference between two amplitudes to $B^- \to \overline{D}^0 K^-$ and $B^- \to D^0 K^-$, that occurs when D^0 and $\overline{D}^0$ decay to common final states. In the GLW method, the interference effect is searched by looking at the D_{CP}^0 decays to CP eigenstates (KK, $\pi\pi$, $K_s\pi^0$, ...). The decay rate is given by:

$$\Gamma(B^\pm \to D_{CP}^0 K^\pm) \propto 1 + r_B^2 + \eta_{CP} \cdot 2r_B \cos(\delta_B \pm \gamma) \tag{2.65}$$

if we neglect the effects due to the D mixing and to the CPV in the D^0 decays. The r_B and δ_B parameters are the ratio magnitude of the amplitudes for the processes $B^- \to \overline{D}^0 K^-$ and $B^- \to D^0 K^-$, and the strong phase. Since r_B can be small, the interference could be small and difficult to measure precisely.

2.5.4 $B^\pm \to D(K\pi)K^\pm$for γ, the ADS method

To enhance the interference effects, a technique, called ADS method, was proposed in 1996 in [**?**] by Atwood, Dunietz and Soni. In this case the D^0 from the favoured $b \to c$ amplitude is reconstructed in the doubly-Cabibbo suppressed final state $K^+\pi^-$, while the $\overline{D}^0$ from the $b \to u$ suppressed amplitude is reconstructed in the favoured final state $K^+\pi^-$ the particular amplitudes of the neutral D meson transitions. [30] The experimental observables depend on four additional parameters: r_B the ratio magnitude of the amplitudes for the processes $B^- \to \overline{D}^0 K^-$ and $B^- \to D^0 K^-$(Fig. 1), the r_D, the ratio magnitude between the $D^0 \to K^+\pi^-$ and $D^0 \to K^-\pi^+$ amplitudes and their relative strong phases δ_B,δ_D .

By measuring the four rates (fig.2.5):

$$\Gamma(B^- \to (K^-\pi^+)_D K^-) \propto 1 + (r_B r_D)^2 + 2r_B r_D \cos(\delta_B - \delta_D - \gamma) \tag{2.66}$$

$$\Gamma(B^+ \to (K^+\pi^-)_D K^+) \propto 1 + (r_B r_D)^2 + 2r_B r_D \cos(\delta_B - \delta_D + \gamma) \tag{2.67}$$

$$\Gamma(B^- \to (K^+\pi^-)_D K^-) \propto r_B^2 + (r_D)^2 + 2r_B r_D \cos(\delta_B + \delta_D - \gamma) \qquad (2.68)$$

$$\Gamma(B^+ \to (K^-\pi^+)_D K^+) \propto r_B^2 + (r_D)^2 + 2r_B r_D \cos(\delta_B + \delta_D + \gamma) \qquad (2.69)$$

it is possible to extract the γ angle given the r_B and r_D, values measured independently. The Monte Carlo simulations show that LHCb will produce, every year, about 56000 favoured events, the first two decay rates, while only 700 of suppressed events.

Actually the LHCb strategy will be combined the GLW and the ADS methods in order to exploit the common parameters and to improve the sensitivity of the γ angle. In tab.2.2 are summarized the expected performances of the different measurements that LHCb will study.

2.5.5 $B^\pm \to D^0(K_s\pi^+\pi^-, ...)K^\pm$ with Dalitz plot

This method is the same ADS applied to a multibody D decays. In the case of the three body decay, the Dalitz analysis can directly measure the γ angle from the interference pattern. Introducing the two invariant mass:

$$m_+^2 = m^2(K_s\pi^+) \qquad m_-^2 = m^2(K_s\pi^-) \qquad (2.70)$$

all the "mass combinations" are reported in a 2D plot, like fig.2.6 . The total B decay amplitude is the sum of the contributions from D^0 and $\overline{D}^0$, as reported in the following lines

$$A^- = f(m_-^2, m_+^2) + r_B e^{i(-\gamma+\delta_B)} f(m_+^2 m_-^2) \qquad (2.71)$$

$$A^+ = f(m_-^2, m_+^2) + r_B e^{i(\gamma+\delta_B)} f(m_+^2 m_-^2) \qquad (2.72)$$

where

$$f(m_+^2, m_-^2) = \left[\sum_{j=1}^{N} a_j e^{i\alpha_j} A_j(m_+^2, m_-^2)\right] + be^{i\beta} \qquad (2.73)$$

with N the number of resonances, a_j and α_j amplitude and phase parameters from the B factories and A_j model dependent parametrization of the matrix element.

$$\Gamma(m_-^2, m_+^2) = \left|f(m_-^2, m_+^2)\right|^2 + r_B^2 \left|f(m_+^2, m_-^2)\right|^2 + \\ +2r_B Re\left[f(m_-^2, m_+^2) f^*(m_+^2, m_-^2) e^{i(-\gamma+\delta_B)}\right] \qquad (2.74)$$

Thus the interference contains the γ dependence. At present the preliminary studies with Monte Carlo have shown a good precision for the γ measurement, as reported in the tab. 2.2.

The same idea can be applied in some decays where the D^0 decays in four bodies, like the $B^\pm \to D^0(KK\pi\pi)K^\pm$.

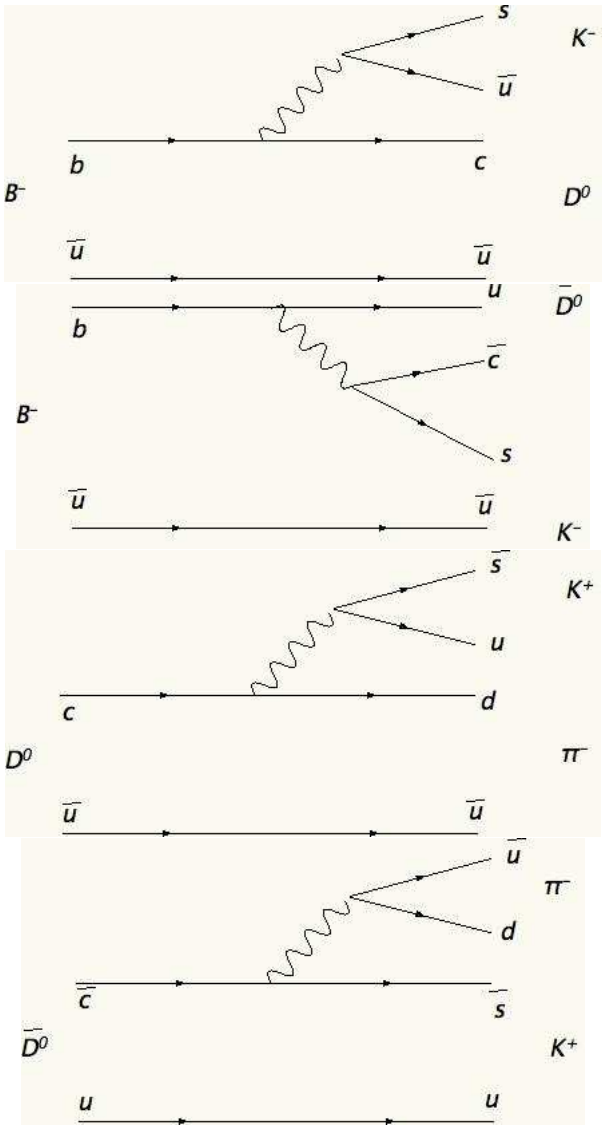

Figure 2.5: Favoured and suppressed decays in $B^{\pm} \to DK^{\pm}$ channel. They give the same final state.

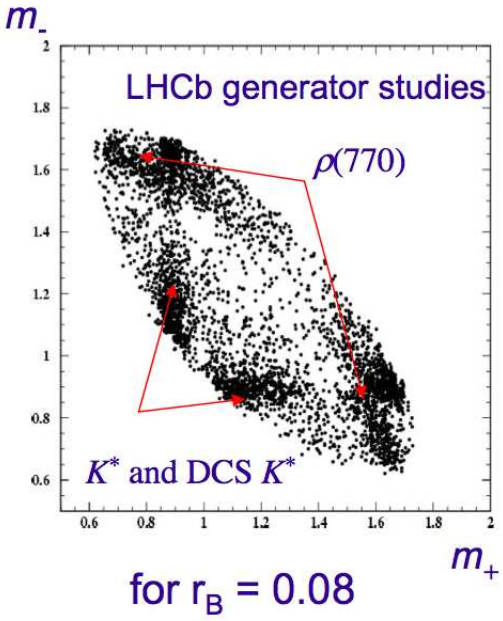

Figure 2.6: The Dalitz plot of the decay $D^0 \to K_s\pi^+\pi^-$. The regions with higher density are the resonance of this decay.

B mode	D mode	Method	$\sigma(\gamma)$
$B^+ \to DK^+$	$K\pi + KK/\pi\pi + K\pi\pi\pi$	ADS+GLW	5°-15°
$B^+ \to D^*K^+$	$K\pi$	ADS+GLW	under study
$B^+ \to DK^+$	$K_s\pi\pi$	Dalitz	15°
$B^+ \to DK^+$	$KK\pi\pi$	4-body "Dalitz"	15°
$B^+ \to DK^+$	$K\pi\pi\pi$	4-body "Dalitz"	under study
$B^0 \to DK^{*0}$	$K\pi + KK + \pi\pi$	ADS+GLW	7°-10°
$B^0 \to DK^{*0}$	$K_s\pi\pi$	Dalitz	under study
$B_S \to D_SK$	$KK\pi$	tagged, A(t)	13°

Table 2.2: Expected γ sensibilities for the LHCb experiment in various $B \to DK$ channels.

Channels	$\sigma(\phi_s)$[rad]	Weight (σ/σ_i)^2 [%]
$B_s \to J/\Psi\eta(\pi^+\pi^-\pi^0)$	0.142	2.3
$B_s \to D_s D_s$	0.133	2.6
$B_s \to J/\Psi\eta(\gamma\gamma)$	0.109	3.9
$B_s \to \eta_c\phi$	0.108	3.9
Combined sensitivity for pure CP eigenstates	**0.060**	**12.7**
$B_s \to J/\Psi\phi$	0.023	87.3
Combined sensitivity for all CP eigenstates	**0.022**	**100.0**

Table 2.3: Expected sensibility to ϕ_s measurement for different decay channel in LHCb.

2.5.6 $B_s \to J/\Psi\phi$, $B_s \to J/\Psi\eta$,$B_s \to \eta_c\phi$ and $B_s \to D_s\bar{D}_s$ for 2χ

Both B_s $\overline{B}_s$ can decay to the same final state $J/\Psi\phi$. Due to the B_s mixing, this process follows two different quantum paths. Their interference, originates a time dependent CP asymmetry, which can point out the phase difference between the $B_s/\overline{B}_s$ oscillation amplitude. The phase difference ϕ_s, within the SM, is estimated as

$$\phi_s = -2\chi = 2\arg\left(\frac{V_{cs}^* V_{cb}}{V_{ts}^* V_{tb}}\right) \tag{2.75}$$

with a little approximation[4] already used in the *golden plated* decay channel $B_d \to J/\Psi K_s$.

The Wolfenstein parametrization ensures that the phase of the decay amplitude is zero, so the observed phase can be wholly ascribed to the $B_s/\overline{B}_s$ oscillation amplitude. Also the SM foresees a small value for the phase ϕ_s[5]and thus, if there is new physics in the $b \to s$ transitions, it will be clearly visible in the CP asymmetry, since

$$\mathcal{A}^{mix} = \sin\phi_s \tag{2.76}$$

Despite the $B_d \to J/\Psi K_s$ channel, the analysis of the $B_s \to J/\Psi\phi$ is more challenging since both particles J/Ψ and ϕ are vectors and the decay proceeds with three different interfering amplitudes, 2 CP even and 1 CP odd. So a completely angular analysis is required (for details see the par. 2.5.8.1). At last the observable time asymmetry is dependent on the $\Delta\Gamma_s$ and Δm_svalues, therefore a great proper time resolution is required.

In case of the $B_s \to J/\Psi\eta$ channel only one CP eigenstate contributes, so the analysis is simpler but the statistics will be about a factor 10 less. Some other minor channels can contribute to the ϕ_s measurement. In tab. 2.3 are summarized the expected performances in one year of data taking, for the different measurements that LHCb will study.

[4]In a similar way as in the $B_d \to J/\Psi K_s$ there are some penguin contributions, but the leading penguin term has the same phase as the tree diagram. So they can be neglected.

[5]$2\chi = 2\eta\lambda^2 = \mathcal{O}(0.04)$

2.5.7 $B_d \to \pi^+\pi^-\pi^0$ and $B \to \rho\rho$ with Dalitz analysis for α extraction

The time dependent analysis of the $B \to \pi^0\pi^+\pi^-$ Dalitz space provides enough observables to fit the different tree and Penguin graph contributions, and hence determine the unitarity triangle angle α with precision of $\sigma(\alpha) < 10$ degrees in one year of data taking.

The extraction of α from the CP asymmetry in $B \to \rho^+\rho^-$ is directly analogous to the method first investigated in the $\pi^+\pi^-$ system. In contrast to $\pi^+\pi^-$, however, the isospin analysis proposed by Gronau and London here provides significant constraints on α because of the small branching ratio for $B \to \rho^0\rho^0$. The main contribution of LHCb to the $B \to \rho\rho$ analysis could be the $B \to \rho^0\rho^0$ measurement since the annual yield of the LHCb will be not competitive with the present production of the other B experiments.[6]

In general the final state is composed by two vectors and then an angular analysis is required. Furthermore, any complications brought about by the vector-vector final state are minor, since the longitudinal polarization is found to be almost maximal.

2.5.8 Looking for New Physics: Rare Decays

Beside the study of B decay asymmetries and rates, to measure the unitarity triangle angles, thanks to the high statistics and precision, LHCb will be able to measure several rare decays. Some of these processes are particularly important to test new physics contributions.

2.5.8.1 $B_s \to \phi\phi$ for new Physics

This decay is a FCNC (flavour changing neutral current) process, that is mediated by loop diagrams as is shown in fig.2.7. For this reason the process is a rare decay. New physics contributions, due to supersymmetric particle exchange in the loop, can contribute significantly to the asymmetry. Within the SM the CP asymmetry is expected $< 1\%$ since

$$\lambda_{\phi\phi}^{SM} = \frac{q}{p}\frac{\overline{A}_{\phi\phi}}{A_{\phi\phi}} = \frac{V_{tb}V_{ts}^*}{V_{tb}^*V_{ts}} \cdot \frac{V_{tb}^*V_{ts}}{V_{tb}V_{ts}^*} = 1 \tag{2.77}$$

So a large asymmetry will be a clear sign of new physics.

The final state is composed by two vectors so an angular analysis is required in order to extract the CP asymmetries. The helicity amplitudes are exploited to calculate the differential decay distributions

$$\frac{d\Gamma(t)}{d\,\cos\theta_1 d\cos\theta_2 d\phi_2 d\phi_1} \propto \left| \sum_{\lambda=0,\pm1} H_\lambda(t) D^{1*}_{\lambda,0}(\phi_1,\theta_1,0) D^{1*}_{\lambda,0}(\phi_2,\theta_2,0) \right|^2 \tag{2.78}$$

[6] Expected annual yields in LHCb (2fb^{-1}) : $B^\pm \to \rho^\pm\rho^0$ 9000 events (B/S$\sim$ 1); $B \to \rho^-\rho^+$ 2000 events (B/S$<$ 5@ 90%C.L.).

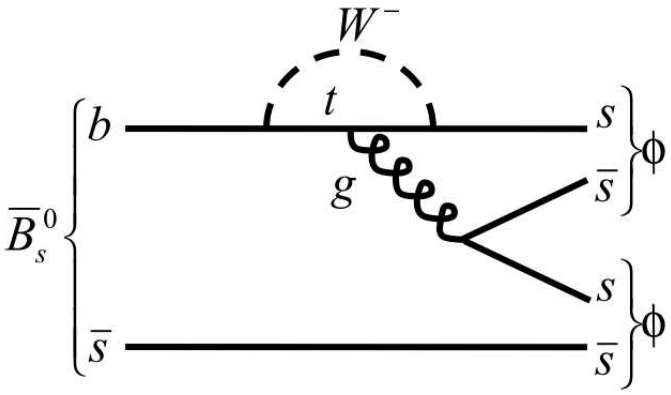

Figure 2.7: FCNC processes govern the $B_s \to \phi\phi$ decay.

where

$$H_0(t) = A_0(t)\; H_{+1}(t) = \left(A_\parallel + A_\perp\right)/\sqrt{2}\; H_{-1}(t) = \left(A_\parallel - A_\perp\right)/\sqrt{2}$$

with A_0 $A_\parallel$ CP even states and $A_\perp$ the odd one. So the time dependent differential description is

$$\frac{d\Gamma(t)}{d\,\cos\theta_1 d\cos\theta_2 d\phi_2 d\phi_1} \propto |A_0(t)|^2 f_1(\theta_1,\theta_2,\chi) + |A_\parallel(t)|^2 f_2(\theta_1,\theta_2,\chi) +$$

$$+|A_\perp(t)|^2 f_{13}(\theta_1,\theta_2,\chi) + Im(A^*_\parallel(t)\,A_\perp(t)) f_4(\theta_1,\theta_2,\chi) +$$

$$+Re(A^*_\parallel(t)\,A_0(t)) f_5(\theta_1,\theta_2,\chi) + Im(A^*_0(t)\,A_\perp(t)) f_6(\theta_1,\theta_2,\chi) \qquad (2.79)$$

where $f_i(\theta_1,\theta_2,\chi)$ are six symmetric angular functions under ϕ meson interchange. Assuming the branching fraction determined by the CDF collaboration ($\sim 10^{-5}$), in the LHCb detector will detect about 4000 events for one year of data taking and reach sensitivity of new physics phase $\sigma(\phi_{NP}) = 0.10$.

2.5.8.2 A rare decay: $B_s \to \mu\mu$

The $B_s \to \mu\mu$ is a very suppressed decay in the SM (BR($B_s \to \mu\mu$) of about $3.8 \cdot 10^{-9}$). There are various extensions to the SM that foresee an enhancement of this branching ratio by 1 to 3 orders of magnitude. In details within the SUSY theory, the branching ratio is enhanced by a $\tan^6\beta$ factor. For this reason, the branching ratio measurements of the decay $B_s \to \mu\mu$ can be a powerful tool to probe for physics beyond the SM. Thank to the great number of $b\overline{b}$ events produced and the LHCb performances, in a year of data taking, a 3 sigmas measurement of the SM value will be possible (fig.2.9). At present the CDF limit is: BR($B_s \to \mu\mu$) $<$ 2.0x10-7 @95% CL.

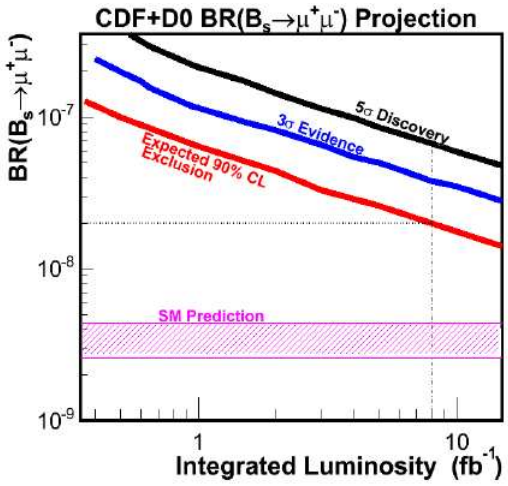

Figure 2.8: Current best limits on the branching ratio $B_s \to \mu\mu$ from CDF and D0 data.

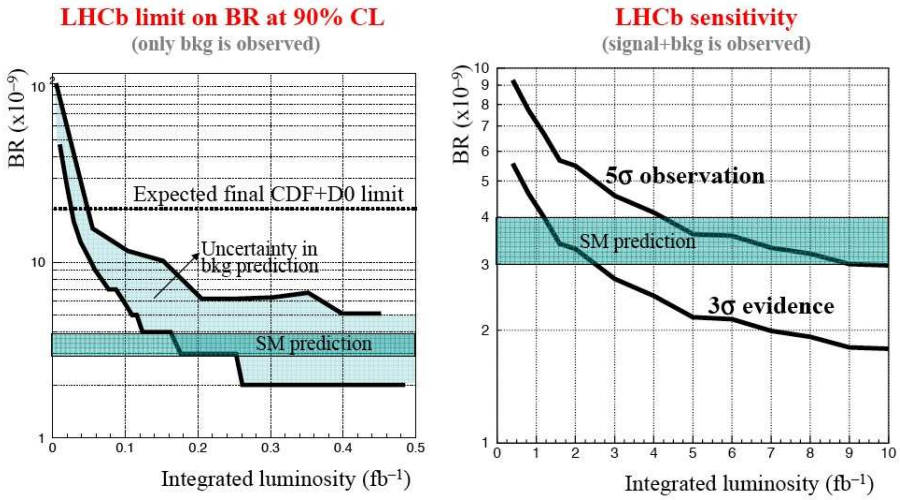

Figure 2.9: Branching ratios limits for $B_s \to \mu\mu$ explored by LHCb experiment.

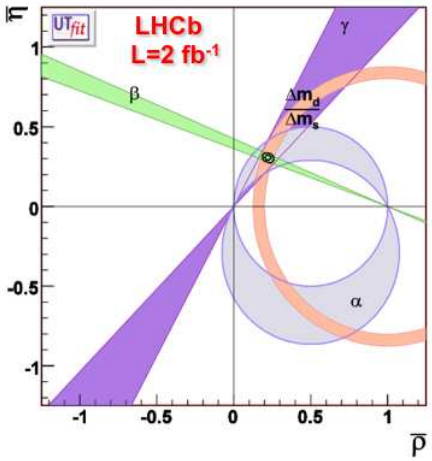

Figure 2.10: After 1 year of data taking, LHCb will collect about $2fb^{-1}$. The CKM triangle is

2.5.9 LHCb impact on the CKM fits

In next years, LHCb will collect a great amount of data, about 2 fb^{-1}/year. The fig. 2.10. shows how our knowledge about the unitarity triangle will be improved due to the increased precision on the measurement of β and γ, and maybe to a less extent of α. The present precisions relate to the triangle apex are $\sigma(\overline{\rho})/\overline{\rho} = 17\%$ and $\sigma(\overline{\eta})/\overline{\eta} = 4.7\%$. After one year of data taking this limit will be shift in order to reach a precision of $\sigma(\overline{\rho})/\overline{\rho} = 7.1\%$ and $\sigma(\overline{\eta})/\overline{\eta} = 3.9\%$. As shown in fig. 2.10, the CKM triangle is well constrained and it is compatible to the SM forecasts, will be very small. For this reason, in order to distinguish new physics, it will become absolutely important an auspicious improvement in the precision of the theoretical model and in the experimental analysis skill.

Chapter 3

Experimental method for proper time calibration

3.1 Introduction

One of the main features of the LHCb experiment is the possibility to measure the B proper time very accurately ($\sigma_\tau \approx 40fs$) which is one of the necessary requirements to measure the fast $B_s/\bar{B}_s$ oscillations and to study precisely the time dependent CP asymmetries.
For this reason the correct measurement of B proper time and the evaluation of its resolution are key points in LHCb physics analyses.
B lifetime can be calculated knowing its distance of flight (from the production vertex, PV to the decay vertex, SV) and its momentum ($\vec{\mathbf{p}}$):

$$\tau_B = \frac{M_B \cdot (\mathbf{PV} - \mathbf{SV})}{\|\mathbf{p}\|} \tag{3.1}$$

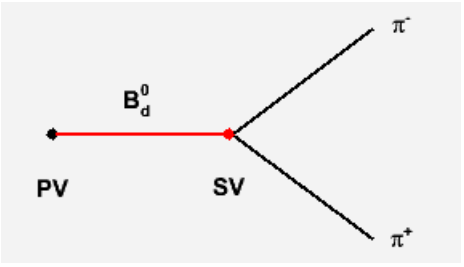

Figure 3.1: Schematic representation of decay channel $B_d \to \pi\pi$: in black are indicated measurable quantities (PV and track parameters), while in red are the unmeasured ones (secondary vertex PV and B_d parameters).

PV is indirectly measured with a common vertex fit of all track segments in the Vertex Locator (VELO), while SV and B momentum are determined by a common vertex fit of the stable B decay products.
In general we can say that the proper time is a function of measured quantities $\tau_B(m_1, m_2, \cdots m_N)$ and its error can be obtained merely by error propagation in case m_i are gaussian distributed:

$$\sigma_\tau^2 = \mathbf{J}_\tau \cdot \mathrm{cov}(\vec{m}) \cdot \mathbf{J}_\tau{}^T \tag{3.2}$$

where $\vec{\mathbf{J}} = (\frac{\partial \tau_B}{\partial m_1}, \frac{\partial \tau_B}{\partial m_2}, ..., \frac{\partial \tau_B}{\partial m_n})$ is the Jacobian and $cov(\vec{m})$ is the covariance matrix associated to the measurements.
Within the validity limits of the equations above, for each event we can calculate B proper time and its error, which estimates the resolution event by event.
From Monte Carlo data it is quite easy to check the correctness of the proper time: by comparing the reconstructed value with the true B decay ($\hat{\tau}_B$) we can calculate the statistical quantity:

$${}^{MC}Pull(\tau_B) = \frac{\tau_B - \hat{\tau}_B}{\sigma_\tau} \tag{3.3}$$

which is distributed as a normal gaussian if the measurement and the error are correct.
On real data we cannot apply this statistical test, since the true B decay is unknown. For this reason it is very important to develop some experimental tools which, at least indirectly, test or study the reliability of measurements and resolutions.
The LHCb collaboration studied different strategies to retrieve proper time resolution from real data, for example by studying the proper time distribution of $J/\psi \to \mu^+\mu^-$ produced directly in pp collisions [32, 33] . The aim of these studies is to find a parametrization of the resolution as a function of kinematical observables.
In this chapter we discuss the possibility to use a kinematical/vertex fitter as a tool to test the input measurements and, at least indirectly, the reliability of proper time measurements. Running such tool on experimental data, would be a fundamental starting point for LHCb analyses, devoted to measure precise time dependent CP violation effects in $B_{d/s}$ decays. This work summarizes several contributions given to the Proper Time & Mixing working group meetings that are quoted in references [34].

3.2 Constrained kinematical and geometrical fit

Constrained fits are widely used in high energy physics experiments to get the best estimates of some relevant information from a set of measurements, or for testing the compatibility of data with a given hypothesis. They can be used for track reconstruction, vertex reconstruction or physics analyses, where one needs to select events of a given decay. Depending on the specific application, the input measurements and the constraints applied can be very different. Despite

the differences, from a statistical/mathematical point of view all the constrained fits can be solved by looking for the set of unknown parameters which minimize the χ^2 according to the measurements and to the given constraints. The mathematical/statistical formalism used is based on the least squares (maximum likelihood) and the Lagrange multiplier method, which will be briefly summarized in the next section.
Beyond the above functionalities, in some cases constrained fits can also be useful to test the correctness of the measurements. If the error distributions are gaussian and the constraint equations are "quasi-linear" within the errors, the distribution normalized residuals (namely FITPull) are normal gaussians (mean=0, sigma=1). Any deviation from the expected shape can be ascribed to a wrong input measurement: i. e. a BIASed value or a scale factor (SF) multiplying the covariance matrix. In this context constrained fits can also be useful in data and resolution calibration.

3.2.1 A statistics reminder: Least squares and Lagrange multipliers method.

Let us consider a set of N measurements m_i of a given observable. Due to the finite experimental accuracy the measured values deviate from the "true" ones, y, by a random amount which is measured by its error σ_i. If the error distribution $E_i = m_i - y$ is gaussian with sigma σ_i the best estimate of the true value $\hat{y}$ can be found by maximizing the likelihood as a function of y:

$$L(y) = \prod_{i=1}^{N} \frac{1}{\sqrt{2\pi}\sigma_i} \exp(-\frac{(m_i - y)^2}{2\sigma_i^2}) \tag{3.4}$$

or, equivalently, by minimizing the weighted sum of the distance squared (least squares):

$$S(y) = \sum_{i=1}^{N} \frac{(m_i - y)^2}{\sigma_i^2} \tag{3.5}$$

In a more general approach we can consider several measurements of different observables that are related by functional relationships. In this case each measurement m_i corresponds to a true value y_i that satisfies a set of constraint equations f_c. A dependence on additional parameters a_j, for which no direct measurement exists, can also be present:

$$f_c(y_1, \cdots, y_N, a_1, \cdots, a_p) = 0 \qquad\qquad c = 1, \cdots, k \tag{3.6}$$

The chisquare in equation (3.5) in this case transforms to the more generic expression:

$$S(\mathbf{y}) = (\mathbf{m} - \mathbf{y})^T \mathbf{W} (\mathbf{m} - \mathbf{y}) = \Delta\mathbf{y}^T \mathbf{W} \Delta\mathbf{y} \qquad\qquad \mathbf{y^T} = (y_1, \cdots, y_N) \tag{3.7}$$

where $\mathbf{W}$ is the inverse covariance matrix associated to the measurements $\mathbf{m^T} = (m_1, \cdots m_N)$ ($\mathbf{W} = \mathrm{cov}^{-1}(\mathbf{m})$).

A simple way to include the equation constraints (3.6) in the least square search is the Lagrange multiplier method: introducing a new unknown scalar variable, the Lagrange multiplier λ_c, for each constraint, the method looks for the minimum of a linear combination of $S(\vec{\mathbf{y}})$ and $\vec{f}(\vec{\mathbf{y}}, \vec{\mathbf{a}})$ involving the multipliers as coefficients.

$$\min\Big((S(\mathbf{y}) - 2\vec{\lambda}^T\mathbf{f}(\mathbf{y},\mathbf{a})\Big) \qquad \vec{\lambda}^{\mathbf{T}} = (\lambda_1, \cdots, \lambda_k) \tag{3.8}$$

$$\begin{cases} \frac{\partial\left(S(\mathbf{y})-2\vec{\lambda}^T\mathbf{f}(\mathbf{y},\mathbf{a})\right)}{\partial y_i} = 0 & i = 1, \cdots, N \\ \frac{\partial\left(S(\mathbf{y})-2\vec{\lambda}^T\mathbf{f}(\mathbf{y},\mathbf{a})\right)}{\partial a_j} = 0 & j = 1, \cdots, p \\ \frac{\partial\left(S(\mathbf{y})-2\vec{\lambda}^T\mathbf{f}(\mathbf{y},\mathbf{a})\right)}{\partial \lambda_c} = 0 & c = 1, \cdots, k \end{cases} \tag{3.9}$$

If the constraint equations have a linear dependence on the parameters they can be rewritten in the matrix form:

$$\mathbf{f}(\mathbf{y},\mathbf{a}) = \mathbf{B}\mathbf{y} + \mathbf{A}\mathbf{a} = \vec{0} \tag{3.10}$$

where $\mathbf{B}$ and $\mathbf{A}$ are $k \times N$ and $k \times p$ matrices respectively. In this case the solution of the constrained least square can be found in one step by solving the linear system:

$$\begin{cases} \mathbf{W}\Delta\mathbf{y} + \mathbf{B}^T\vec{\lambda} &= \vec{0} \\ \mathbf{A}^T\vec{\lambda} &= \vec{0} \\ \mathbf{B}\mathbf{y} + \mathbf{A}\mathbf{a} &= \vec{0} \end{cases} \tag{3.11}$$

In the case of non linear constraints they can be linearized by using a Taylor expansion close to a "good enough" solution $(\vec{\mathbf{y}}^0, \vec{\mathbf{a}}^0)$ and the problem can be solved iteratively. In this case the matrices $\mathbf{B}$ and $\mathbf{A}$ assume respectively the meaning of first derivative with respect to $\vec{y}$ and $\vec{a}$:

$$\mathbf{f}(\mathbf{y},\mathbf{a}) \approx \mathbf{f}(\mathbf{y}^0,\mathbf{a}^0) + \begin{pmatrix} \frac{\partial f_1^0}{\partial y_1} & \cdots & \frac{\partial f_1^0}{\partial y_N} \\ \cdots & \cdots & \cdots \\ \frac{\partial f_k^0}{\partial y_1} & \cdots & \frac{\partial f_k^0}{\partial y_N} \end{pmatrix} \begin{pmatrix} \Delta y_1 \\ \cdots \\ \Delta y_N \end{pmatrix} + \begin{pmatrix} \frac{\partial f_1^0}{\partial a_1} & \cdots & \frac{\partial f_1^0}{\partial a_p} \\ \cdots & \cdots & \cdots \\ \frac{\partial f_k^0}{\partial a_1} & \cdots & \frac{\partial f_k^0}{\partial a_p} \end{pmatrix} \begin{pmatrix} \Delta a_1 \\ \cdots \\ \Delta a_p \end{pmatrix} + \cdots \tag{3.12}$$

If we are close enough to the solution, at each iteration cycle α we can linearise the equations around the values found at the previous step:

$$\begin{aligned} &\mathbf{f}(\mathbf{y}^\alpha,\mathbf{a}^\alpha) + \mathbf{B}^\alpha(\Delta\mathbf{y}^\alpha - \Delta\mathbf{y}^{\alpha-1}) + \mathbf{A}^\alpha(\Delta\mathbf{a}^\alpha - \Delta\mathbf{a}^{\alpha-1}) \approx 0 \\ &\mathbf{B}^\alpha\Delta\mathbf{y}^\alpha + \mathbf{A}^\alpha\Delta\mathbf{a}^\alpha = \mathbf{c} \\ &\mathbf{c} = \mathbf{B}^\alpha\Delta\mathbf{y}^{\alpha-1} + \mathbf{A}^\alpha\Delta\mathbf{a}^{\alpha-1} - \mathbf{f}(\mathbf{y}^\alpha,\mathbf{a}^\alpha) \end{aligned} \tag{3.13}$$

where $\vec{\mathbf{c}}$ is a "residual" value which stops the iteration when the desired accuracy is reached. In this case the best estimates of the parameters are found by solving the linear system:

$$\begin{cases} \mathbf{W}\Delta\mathbf{y} + \mathbf{B}^T\vec{\lambda} &= 0 \\ \mathbf{A}^T\vec{\lambda} &= 0 \\ \mathbf{B}\Delta\mathbf{y} + \mathbf{A}\Delta\mathbf{a} &= \mathbf{c} \end{cases} \tag{3.14}$$

The solution of this system is searched by iterating the calculation:

$$\begin{pmatrix} \Delta\mathbf{y} \\ \Delta\mathbf{a} \\ \vec{\lambda} \end{pmatrix} = \begin{pmatrix} \mathbf{W} & \mathbf{0} & \mathbf{B}^T \\ \mathbf{0} & \mathbf{0} & \mathbf{A}^T \\ \mathbf{B} & \mathbf{A} & \mathbf{0} \end{pmatrix}^{-1} \begin{pmatrix} \mathbf{0} \\ \mathbf{0} \\ \mathbf{c} \end{pmatrix} = \begin{pmatrix} \mathbf{C_{11}} & \mathbf{C_{21}}^T & \mathbf{C_{31}}^T \\ \mathbf{C_{21}} & \mathbf{C_{22}} & \mathbf{C_{32}}^T \\ \mathbf{C_{31}} & \mathbf{C_{32}} & \mathbf{C_{33}} \end{pmatrix} \begin{pmatrix} \mathbf{0} \\ \mathbf{0} \\ \mathbf{c} \end{pmatrix} \quad (3.15)$$

When the desired accuracy is reached ($|c_i| \leq \epsilon$) we get the best estimate of the parameters $\hat{\mathbf{y}} = \Delta\mathbf{y} + \mathbf{y}^0 = \Delta\mathbf{y} + \mathbf{m}$ and $\hat{\mathbf{a}} = \Delta\mathbf{a} + \mathbf{a}^0$.

3.2.2 Definition of Pull quantities.

Once the solution of the least square minimization is found, it is possible to calculate also the covariance matrix of the parameters by propagating the errors according to the Jacobian (see Appendix for details)[35].
The covariance matrix has the form :

$$\mathbf{V}\begin{pmatrix} \hat{\mathbf{y}} \\ \hat{\mathbf{a}} \\ \hat{\vec{\lambda}} \end{pmatrix} = \begin{pmatrix} \mathbf{C_{11}} & \mathbf{C_{21}}^T & \mathbf{0} \\ \mathbf{C_{21}} & \mathbf{C_{22}} & \mathbf{0} \\ \mathbf{0} & \mathbf{0} & -\mathbf{C_{33}} \end{pmatrix} \quad (3.16)$$

In particular we are interested in the covariance matrix of the parameters $\vec{\mathbf{y}}$:

$$\mathbf{V}(\hat{\mathbf{y}}) = \mathbf{W}^{-1} - \mathbf{W}^{-1}\,\mathbf{B}^T\,\mathbf{W_B}\,\mathbf{B}\,\mathbf{W}^{-1} + \mathbf{W}^{-1}\mathbf{B}^T\,\mathbf{W_B}\,\mathbf{A}\,\mathbf{W_A}^{-1}\,\mathbf{A}^T\,\mathbf{W_B}\,\mathbf{B}\,\mathbf{W}^{-1} \quad (3.17)$$

and in the covariance matrix of $\mathbf{\Delta y}$ which turns out to be:

$$\mathbf{V}(\mathbf{\Delta y}) = \mathbf{W^{-1}} - \mathbf{V}(\hat{\mathbf{y}}) \quad (3.18)$$

At this point we can define the normalized "stretch values" or "FITPulls" as:

$${}^{FIT}Pulls(y_i) = \frac{\Delta\mathbf{y}_i}{\sqrt{\mathbf{cov}_{ii} - \mathbf{V}(\hat{\mathbf{y}})_{ii}}} \quad (3.19)$$

If the measured data are gaussian distributed and the linearization of the equation constraint is a good approximation within the range spread by the measurements, FITPulls turn out to be distributed as normal gaussians ($\mu = 0$, $\sigma = 1$). Likewise, it is reasonable to expect that if one of the conditions above is not satisfied a deviation from normality of their shape should appear. This feature represents the key point of the calibration method we are proposing in this note.

3.3 Some useful cases in LHCb analyses and the `GlobalFitter` *Tool*

We have shown that constrained least squares provide not only the best estimates of some parameters and the χ^2 value but they also allow the calculation

of the normalized FITPull quantities which, under precise conditions, have a well known distribution.
We want to use the FITPull distributions to check if the measurements (**m**) and their corresponding errors (**cov**) are correctly determined. Of course the method has to be first validated on specific useful cases which LHCb will work on. In particular we have to understand if the hypothesis about the linearization of the constraint equations or the gaussian distribution of the measurements are valid assumptions.
The LHCb collaboration developed several kinematical/geometrical fitters which implement in different ways the constraint equations. In this note we will consider the `Global Fitter` *Tool* which was developed by V.Vagnoni, A.Carbone, G. Balbi and S.Vecchi since it was the only tool suitable to calculate the FITPulls and the proper time error by correctly considering the correlations given by the constraints and the full covariance matrices of the input measurements.

3.3.1 The `GlobalFitter` Tool

The `GlobalFitter` is a general purpose fit tool which aims at fitting in one call a complete multi vertex decay tree. This approach leads to similar results of the other tools, which fit the decay tree step by step in cascade. The main difference to the other fitters is that the `GlobalFitter` retrieves all the kinematical parameters, adjusted after the fitting procedure. Depending on the complexity of the decay tree, the constraint equations may change.

During the first draft of this thesis, in LHCb a particle was defined by 5 track parameters[1] (x, y coordinates at a given reference plane $z = \tilde{z}$, slopes t_x, t_y in (x, z) and (y, z) planes and the momenta p). From these definition it is easy to obtain p_x, p_y, p_z components and the energy E.

$$p_x = p\,\frac{t_x}{\sqrt{1+t_x^2+t_y^2}} \quad p_y = p\,\frac{t_y}{\sqrt{1+t_x^2+t_y^2}} \quad p_z = p\,\frac{1}{\sqrt{1+t_x^2+t_y^2}} \quad E = \sqrt{m^2+p^2} \tag{3.20}$$

Any B decay can be described by a nested tree of decays, each one defined by a vertex and two or more decaying particles. Vertices and particles may or may not be measured and the particles can decay themselves to other particles. For each decay the equations are:

$$\begin{aligned} &x^i - x_V - t_x^i(\tilde{z} - z_V) = 0 \\ &y^i - y_V - t_y^i(\tilde{z} - z_V) = 0 \\ &\vec{p}_X - \textstyle\sum \vec{p}^{\,i} = 0 \\ &M_X^2 - (\textstyle\sum_i E^i)^2 + |\textstyle\sum_i \vec{p}^{\,i}|^2 = 0 \end{aligned} \tag{3.21}$$

where the first two equations request the particle i to originate from (or decay to) the vertex V, the third apply momentum conservation and the last one constraint the origin particle mass M_X. Of course momentum and mass conservation are applied only if the considered decay-unit request the constraint (in

[1] Now in the experiment we use a parametrization with 7 quantities.

case of inclusive decays or large resonance decays this doesn't happen).
We can immediately note that constraint equations couple quasi independent groups of parameters:

- 1) vertex constraints couple track parameters x^i, t_x^i (y^i, t_y^i) with vertex ones x_V, z_V (y_V, z_V)
- 2) mass and momentum conservation constraints couple only slopes t_x^i, t_y^i and momentum p^i of the particles involved in the decay .
- 3) constraint equations are not linear. A Taylor linear expansion is performed close to a first estimate of the solution which is calculated from the measured values.

This feature will be shown up and discussed later on during the examples explanation.
The number of degrees of freedom of the fit depends on the complexity of the decay tree, which is defined by the number of constraints C and by the number of unmeasured parameters U and is given by $N_{dof} = C - U$.
In the following to validate the FITPull method we will consider in detail the channel $B_d^0 \to \pi^+\pi^-$, which is rather simple to reconstruct, since it originates two high p_T pions detached from the interaction vertex. The decay diagram is represented in figure .... where in black are the measured quantities and in red the unmeasured ones. In this decay topology we apply 12 constraints ($\pi^+\pi^-$ common vertex SV, B originating in PV and decaying in SV, and mass and momentum conservation) and we have 8 unknown parameters (SV and B track parameters), so the fit has 4 degrees of freedom.
During the FITPull method test we also considered the channel $B_s^0 \to D_s(KK\pi)\pi$. In this is a case the complexity of the decay tree is higher, the number of constraints is 24 ($KK\pi$ common vertex DV, $D_s\pi$ common vertex BV, B originating in PV and decaying in BV, and mass and momentum conservation in each decay) and we have 16 unknown parameters (DV, BV and B and D track parameters), so the fit has 8 degrees of freedom. Since the results obtained are very similar to the $B_d^0 \to \pi^+\pi^-$, for shortness we only report the simple case ones.

Starting from the measured values by satisfying the constraint equations, it is possible to determine the unknowns; this fitting procedure also achieves the improvements of the measured input track parameters. The `GlobalFitter` employs an iterative procedure to find out the solution.

3.3.2 Inside the `GlobalFitter`. The $B \to \pi\pi$ case

As we have seen in the previous paragraph, the starting step for the `GlobalFitter` *Tool* is the logical decay tree definition, where the B decay is described by a nested tree of decays, each one defined by a vertex object with two or more decaying particles objects.

In the fig.3.1 a $B_d \to \pi\pi$ event has been depicted and it can help us to understand how the `GlobalFitter` works.

The tree construction, in this specific case, can be summarized in these following actions:

- take the two pions (measured values)
- create a new initialized vertex object, that we call decay vertex SV
- attach the pions to SV
- create a new particle object that is the B particle. It is completely unknown.
- attach the SV to the B particle as its decay vertex
- attach the production vertex PV to the B particle

After this process we obtain a complete logical decay tree where there are measured (values and their errors) and unmeasured quantities. In this tree object there are implicitly declared some kinematical constraints.
The `GlobalFitter`, for the fitting procedure, searches for a solution which minimize the eq.3.7. To fulfill this minimization, the program applies the theory of the Lagrange multipliers method with constraints.

If the conditions are linear, the solution is determined in one step with a simple matrix inversion, whereas in case of nonlinear constraints the solution is reduced to a sequence of linear problems by the linearization of the conditions. Coming back to our example, in case of a fit with a mass constraint in the secondary vertex, (SV in fig.3.1) the geometrical conditions are represented by:

$$\begin{aligned} x_0 - t_x^+(z - z_0) - x^+ &= 0 \\ x_0 - t_x^-(z - z_0) - x^- &= 0 \\ y_0 - t_y^+(z - z_0) - y^+ &= 0 \\ y_0 - t_y^-(z - z_0) - y^- &= 0 \end{aligned} \tag{3.22}$$

These 4 lines are the conditions for the trajectories of the two outgoing particles to pass through the SV, while the mass constraint and the conservation of the momentum, applied to the decay vertex:

$$\begin{aligned} \mathbf{p_B} &= \mathbf{p}^+ + \mathbf{p}^- \\ (E^+ + E^-)^2 - (\mathbf{p}^+ + \mathbf{p}^-)^2 - M_B^2 &= 0 \end{aligned} \tag{3.23}$$

In this example the measured quantities are the input track parameters of the two trajectories ($x^+, y^+, p^+, t_x^+, t_y^+$ and $x^-, y^-, p^-, t_x^-, t_y^-$) , while the unmeasured ones are the secondary vertex coordinates. The incidental knowledge of the primary vertex achieves the employment of new four equations:

$$
\begin{aligned}
&x_{PV} - t_x^B(z - z_{PV}) - x^B = 0 \\
&y_{PV} - t_y^B(z - z_{PV}) - y^B = 0 \\
&x_0 - t_x^B(z - z_0) - x^B = 0 \\
&y_0 - t_y^B(z - z_0) - y^B = 0
\end{aligned}
\tag{3.24}
$$

Adding these new constraints, we have to face five new unknowns, i.e. the B track parameters.

The twelve equations point out the necessity to linearize the constraints.

Linearization technique requires starting values for the variables. For the measured variables, the measurement itself is taken as starting approximation. For unmeasured parameters starting values have to be determined in a way depending on the specific kind of problem. The starting values for the parameters are denoted by a. Moreover the linearization is expressed in each iteration in terms of corrections Δy and Δa to the starting values y and a. The corrections Δy, Δa and λ are obtained by the multiplication:

$$
\begin{aligned}
&\Delta\mathbf{y} = \mathbf{C_{31}^T}\,\mathbf{c} = \left(\mathbf{W^{-1}}\,\mathbf{B^T}\,\mathbf{W_B} - \mathbf{W^{-1}}\,\mathbf{B^T}\,\mathbf{W_B}\,\mathbf{A}\,\mathbf{W_A^{-1}}\,\mathbf{A^T}\,\mathbf{W_B}\right)\mathbf{c} \\
&\Delta\mathbf{a} = \mathbf{C}_{32}^T\,\mathbf{c} = \mathbf{W_A^{-1}}\,\mathbf{A^T}\,\mathbf{W_B}\,\mathbf{c} \\
&\vec{\lambda} = \mathbf{C}_{33}\,\mathbf{c} = \left(-\mathbf{W_B} + \mathbf{W_B}\,\mathbf{A}\,\mathbf{W_A^{-1}}\,\mathbf{A^T}\,\mathbf{W_B}\right)\mathbf{c}
\end{aligned}
\tag{3.25}
$$

whereas the new covariance matrix for the combined vector $\hat{\mathbf{y}}$, $\hat{\mathbf{a}}$, $\hat{\lambda}$ is defined in eq.3.16.

At the end of each iteration, the `GlobalFitter` retrieves the vectors of corrections for measured and unmeasured quantities, to be applied to the initial values. After several iterations the convergence is reached and then the program retrieves a vector which contains the the estimated parameters (unknown measurements) and the corrected measured quantities.

3.4 Validation of the FITPull method with input gaussian distributions.

In order to prove that the FITPull can be a valid tool to calibrate tracks and vertices in LHCb we first have to show that in controlled situations they are distributed as *normal gaussians*. For this reason we need to work with perfectly gaussian distributed measurements and pure signal events, so we can avoid the problem of background contamination, or non gaussian dependence.

3.4.1 *Fake measurement* generation

For each test we consider a sample of ≈ 40000 Monte Carlo events generated by the LHCb collaboration during DC04 data production. For each event with a

single pp collision we generate *fake measurements* by smearing the particle and vertex true information corresponding to the specific signal channel considered ($B \to \pi^+\pi^-$) according to a gaussian resolution model. Correlation between different measurement can also be described. Then we apply the `GlobalFitter` vertex tool configured to test the specific decay tree. For each measurement we compute the FITPull, which is plotted on a histogram to study its statistical distribution. Since we only process signal events whose errors are perfectly gaussian distributed, we apply a loose χ^2 cut ($\chi^2 < 1000$) to select events.
The use of fake measurement generation offers the advantage to test the FITPull method also in different situations, for example in the presence of systematic errors, knowing exactly the input variable distribution.
In case we want **gaussian distributed "fake measurements"**, each measurement m_i is obtained by smearing the Monte Carlo true value t_i with the following equation:

$$\begin{array}{ll} m_i & = t_i + \sigma_i \cdot G_{\mu=0}^{\sigma=1} \\ \mathbf{cov}_{ij} & = \rho_{ij} \cdot \sigma_i \cdot \sigma_j \end{array} \tag{3.26}$$

where $G_{\mu=0}^{\sigma=1}$ is the normal gaussian random generator and **cov** is the covariance matrix. Its elements are set to realistic values or parametric functions, which were obtained by Monte Carlo studies on reconstructed particles and vertices:

$$\begin{array}{lll} \sigma_x = \sigma_y = \frac{\sigma_{IP}}{\sqrt{2}} = \frac{C_0 + C_1/p_t}{\sqrt{2}} & C_0 = 0.014\,\text{mm} & C_1 = 0.035\text{mm GeV} \\ \sigma_{t_x} = \sigma_{t_y} = C_2 & C_2 = 0.0004\,\text{mrad} & \\ \sigma_p = C_3|p| & C_3 = 0.004 & \\ \sigma_{V_x} = \sigma_{V_y} = C_4 & C_4 = 0.010\,\text{mm} & \\ \sigma_{V_z} = C_5 & C_5 = 0.040\,mm & \end{array} \tag{3.27}$$

If needed the generation of correlated measurements is done with a simple linear transformation of independent measurements.

3.4.1.1 Adding a scale factor to the covariance matrix or a bias to a measurement.

In case we want to simulate the effect of a BIASED measurement m_i or a scaling factor (SF) to the covariance matrix, equations (3.26) transform to:

$$\begin{array}{ll} m_i & = t_i + \sigma_i \cdot (G_{\mu=0}^{\sigma=1} + BIAS_i) \\ \mathbf{cov}_{ij} & = \rho_{ij} \cdot \sigma_i \cdot \sigma_j / (SF_i \cdot SF_j) \end{array} \tag{3.28}$$

In some of the tests performed, a linear dependence of BIAS or SF of particles measurements on p is also introduced and a charge dependence on the BIAS included ($BIAS_i$ and/or $SF_i = q(a + b\,p)$). $SF_i > 1$ simulates underestimated covariance matrix element.

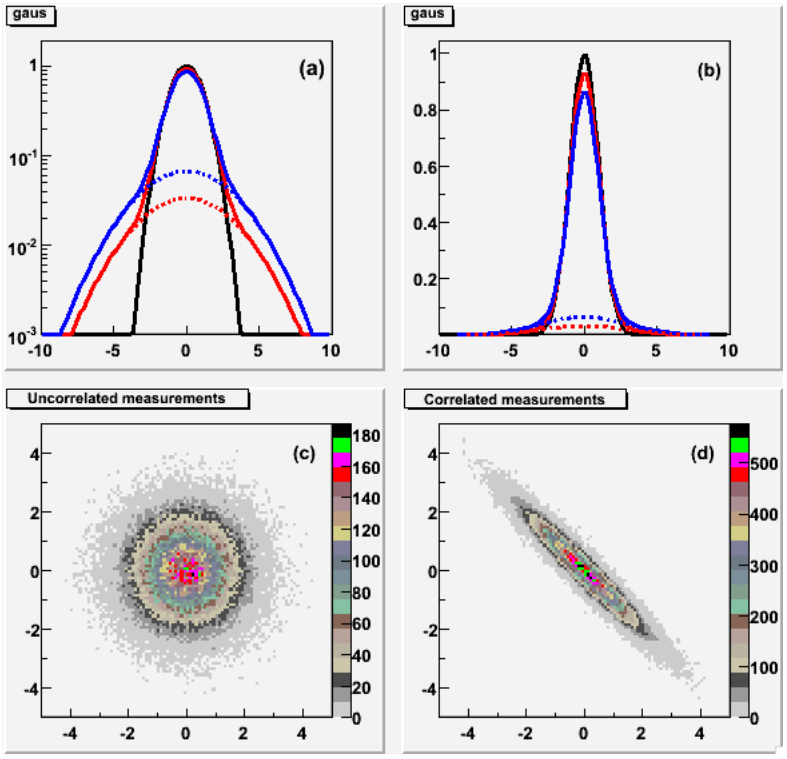

Figure 3.2: Fake measurement generation in case of single gaussian (a) or double gaussian distributions (b) ($w = 0.9$ in red, $w = 0.8$ in blue), for uncorrelated (c) or correlated measurements (d).

3.4.1.2 Non gaussian distributions.

In our studies we want to identify the validity limits of the method if input measurements are not perfect gaussians. In particular we consider the case of a generation of fake measurements according a double gaussian distribution:

$$\begin{array}{ll} m_i & = t_i + \sigma_i \cdot (w \cdot G^{\sigma=1}_{\mu=0} + (1-w) \cdot G^{\sigma=3}_{\mu=0} + BIAS_i) \\ \mathbf{cov}_{ij} & = \rho_{ij} \cdot \sigma_i \cdot \sigma_j / (SF_i \cdot SF_j) \end{array} \tag{3.29}$$

which simulates the effect of tails in the measurement distribution (see figure).

3.4.2 Results

In this section we test the FITPull method in a variety of input conditions in order to study the validity of the tool and characterize its performances. We start with very simple tests and then we add complexity.

3.4.2.1 Correct input data.

By generating *fake measurements* according to equations 3.26 with SF=1 and BIAS=0 we test the fit performances in the ideal case. In this case, if the method is valid, we expect that the FITPulls follow a normal gaussian distribution. In figure for each input measurement (pion track parameters x, y, t_x, t_y, p and PV coordinates V_x, V_y and V_z) the mean (left) and sigma (right) values that fit the corresponding FITPull distributions are represented. The results are in good agreement with zero mean and unit sigma, proving the validity of the method we are proposing. In this situation the B proper time and error are correctly determined, as can be inferred by a comparison with the MC true information. Figure 3.3, also reports the mean and sigma values of the MCPull on proper time, which are in perfect agreement with the values μ =0 and σ =1.
This first test allows us to conclude that if input measurements and errors are correct FITPulls are canonically distributed (normalized gaussian) and proper time value and error are correctly calculated. This result is achieved both in the case we consider correlation betweeen the measurements or not.

3.4.2.2 Biased input data.

If a vertex or a particle measurement is BIASed we would be able to identify it in the real data only if the FITPull associated to the corrupted measurement deviates from the canonical distribution. Following equation (**??**) we first test the effect of a single BIASed measurement to the FITPull distributions. In figure are shown the results of different tests where a BIAS on the particle x (top), t_x (middle) and p (bottom) are considered. As one can see, in case of a single biased measurement without correlations, FITPulls easily show the corrupted variable (mean value $\neq$ 0). The sign of the mean is correctly found, but the value is not equal to the BIAS one: it depends on which measurement is corrupted, being 0.6, 0.4 and 1.2 in case of x, t_x or p BIAS. The input BIAS affects

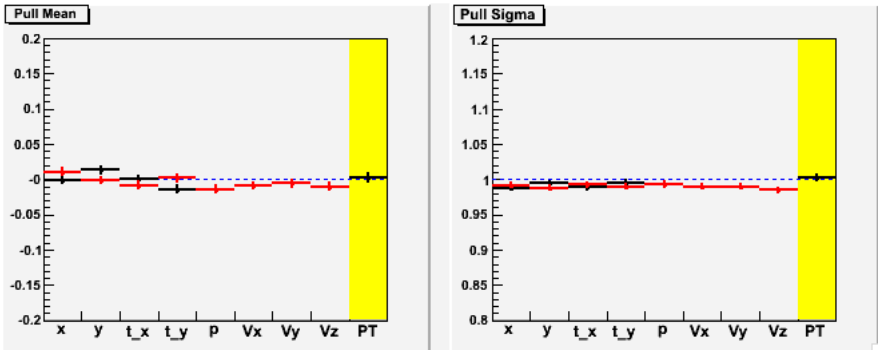

Figure 3.3: Graphical representation of the FITPull parameters: mean values (left) and sigma (right) of the FITPulls associated to each measurement associated to track (x, y, t_x, t_y, p) and PV (V_x, V_y, V_z), obtained by a gaussian fit to the distributions. In case of track measurements red and black points correspond to positive and negative pions. On yellow background are MCPull values of the B proper time calculated with the fitted values. Input fake measurements are independently generated according to BIAS=0 and SF=1.

also FITPull variances, some of these now deviate significantly from unity, even if the input SF is 1. We have to keep in mind this effect in order to correctly interpret the FITPull outputs. Later on we will discuss this problem in more detail.
A bias on y (t_y) gives results equal to the x (t_x) case, since the constraint equations are exactly symmetric.
From these tests it is also evident that B proper time is not BIASed but, especially in the case of the x BIAS, the calculated error shows a SF$\neq$1. These results remark the importance of a calibration method based on real data only, able to spot any incorrect measurement.
If correlations between $x - t_x$ and $y - t_y$ in track parameters are considered[2] the FITPull output changes (see figure 3.5). Although the BIAS is only on x (correlated measurements don't necessarily mean correlated BIASes), FITPull distributions present a mean$\neq$ 0 on both x and t_x with reversed signs. The same thing happens in case of a biased t_x. The reason for this behavior is the almost 100% correlation between the two measurements[3], which makes the fit mean values correlated even if the input ones are not. In fact we have to remember that in this way we are testing the constrained least square method

[2]On Monte Carlo data, by studying MCPull correlations corresponding to different track measurements at *point on track* reference position, we get $\rho_{x,t_x} = \rho_{y,t_y} = -0.95$. (*****)

[3]The correlation between x and t_x is introduced by the transport mechanism in the tracking software, which takes their two initially independent measurements and it projects them to the minimal distance point close to the 2 tracks following the relation

$$x_{transp} - t_x^+(z_{transp} - z_0) - x^+ = 0$$

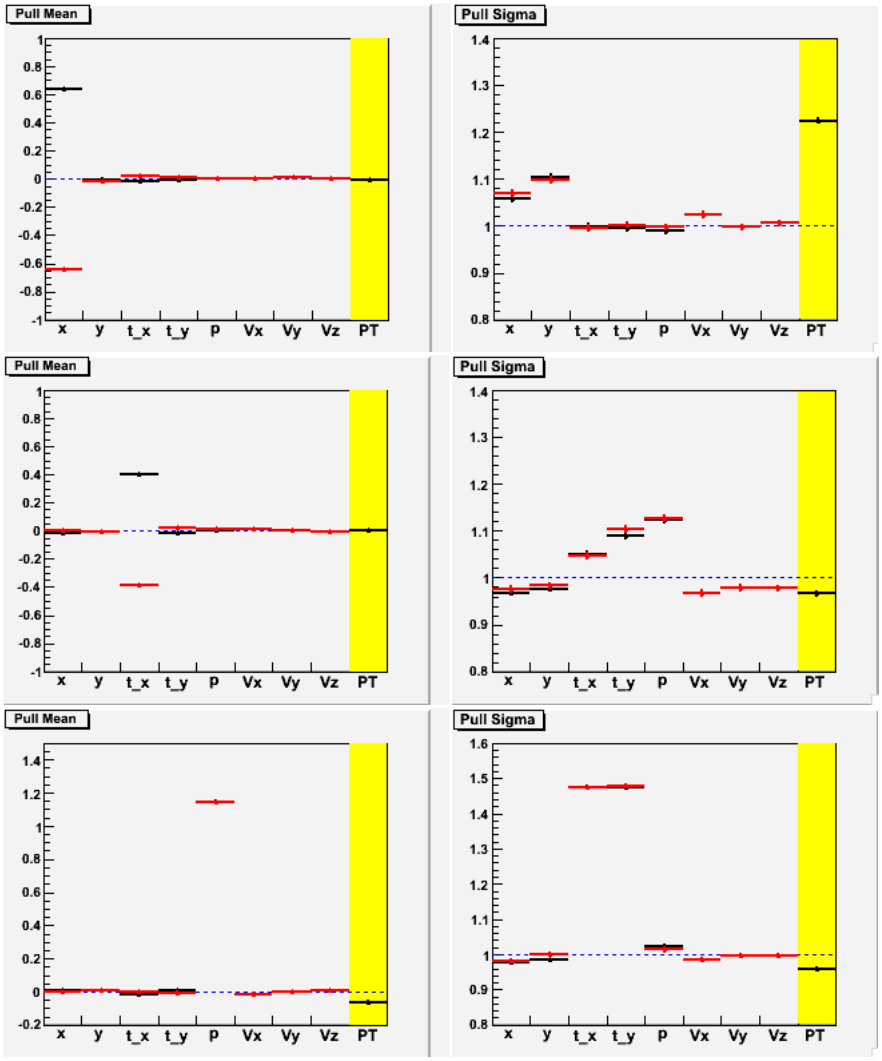

Figure 3.4: Graphical representation of the FITPull parameters (same graphical convention as figure . Input fake measurement are independently generated with SF=1 and BIAS=$\pm$1 on x (top), BIAS=$\pm$1 on t_x (middle) and BIAS=1 on p (bottom). The sign is given by the charge of the particle.

in an unconventional way, since one of the hypothesis is not fulfilled being the input measurements gaussian distributed around the true value, . Even in this case proper time error show a SF.

The effects of a BIAS on PV measurements are plotted in figure 3.6. A BIAS on V_x also modifies FITPulls x and t_x, while in case of a BIAS on V_z only FITPull V_z is affected. This is due to the coupling introduced by the vertex constraint equations which, as we noticed above, strictly group x and t_x to V_x. As a result B proper time is biased if V_z is BIASed.

From the tests performed so far we can conclude that a BIAS on a measurement will make FITPulls appear not canonical. In some cases the corrupted FITPull identifies the corrupted measurement, but, due to the couplings between variables, this statement is not valid in general. In some cases, as expected, a BIAS on a measurement affects also the B proper time in a relevant way.

3.4.2.3 Scale Factor in the covariance matrix.

In order to simulate an incorrect resolution we introduce a $SF = 2$ to the covariance matrix elements of x, t_x, p, V_x and V_z separately. FITPull distributions are sensitive to SF: in this case their sigma deviates from 1 as it is shown in figure , especially in the cases of SF on x, p and V_z. It should be noticed that the mean values are still compatible with 0. The one-to-one correspondence between the wrong FITPull and the corrupted measurement is possible only in some cases, and in general any observed deviation from canonical FITPull distributions can be ascribed to a wrong measurement error.
Figure also shows the effect on B proper time resolution, which in the cases of SF on x, p and V_z, turns out to be affected significantly.

3.4.2.4 Double Gaussian error distribution.

Usually the distribution of real measurements are only approximately gaussian, since tails commonly show up. To be able to use the FITPull method on real data, we have to prove that tails do not modify the output distributions too much, or if they do, we need to establish the validity limits of our proposal.
In this case fake measurements were generated by smearing Monte Carlo truth informations according to double gaussian distributions (see equation 3.29), where a fraction w of events have correct measurements, while the remaining ones have under-estimated errors (by a factor 3). In this test all track parameters are modified simultaneously. In previous tests we have seen that SFs in the covariance matrix affect FITPull variances, so we expect that FITPull distributions are deviated by an amount which depends on the tail contribution. Indeed in cases of $w \neq 1$ FITPulls show a double gaussian shape. The important result is that their main components are still canonical if the tail contribution does not exceed $10 - 15\%$, while they start to deviate significantly for larger amounts (see figure). So we can state that the method is still a good tool provided that the tail contributions are less than $\approx 10\%$. Concerning the B proper time, figure summarizes the dependence of its main and second gaussian contribution as a

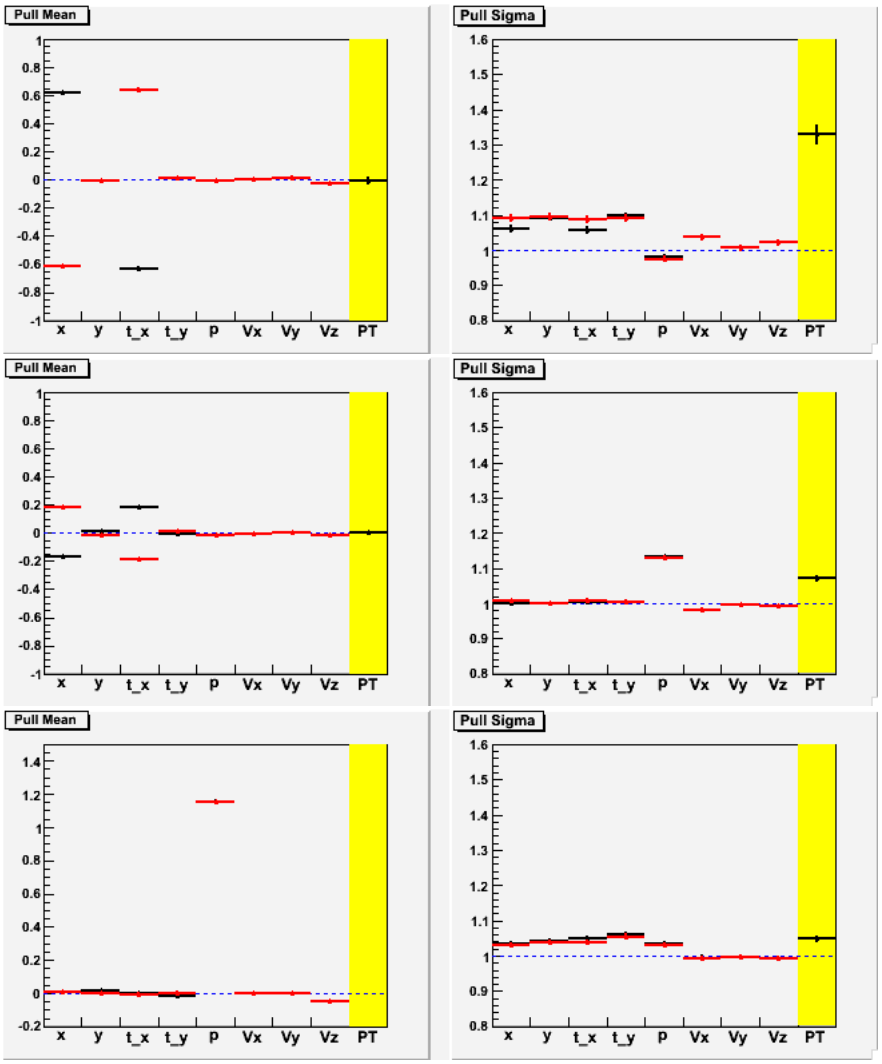

Figure 3.5: Graphical representation of the FITPull parameters (same graphical convention as figure). Input fake measurements are generated with SF and BIAS on(top), BIAS=± 1 on t_x (middle) and BIAS= 1 on p (bottom) in case of correlated $x - t_x$ and $y - t_y$ track parameters.

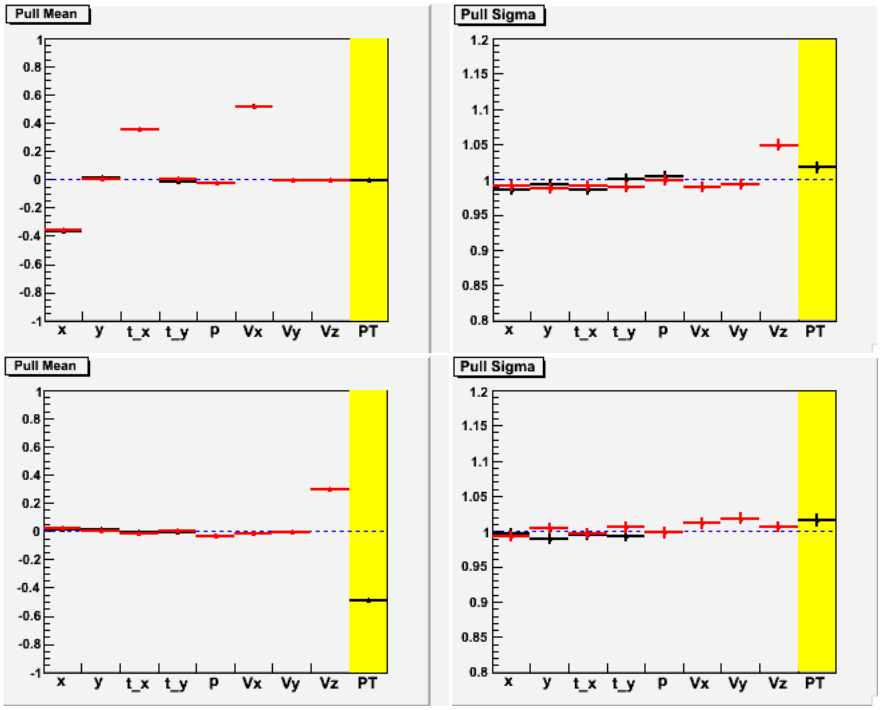

Figure 3.6: Graphical representation of the FITPull parameters (same graphical convention as figure). Input fake measurements are generated with SF=1 and BIAS=1 on V_x (top) and V_z (bottom) in case of correlated $x - t_x$ and $y - t_y$ track parameters.

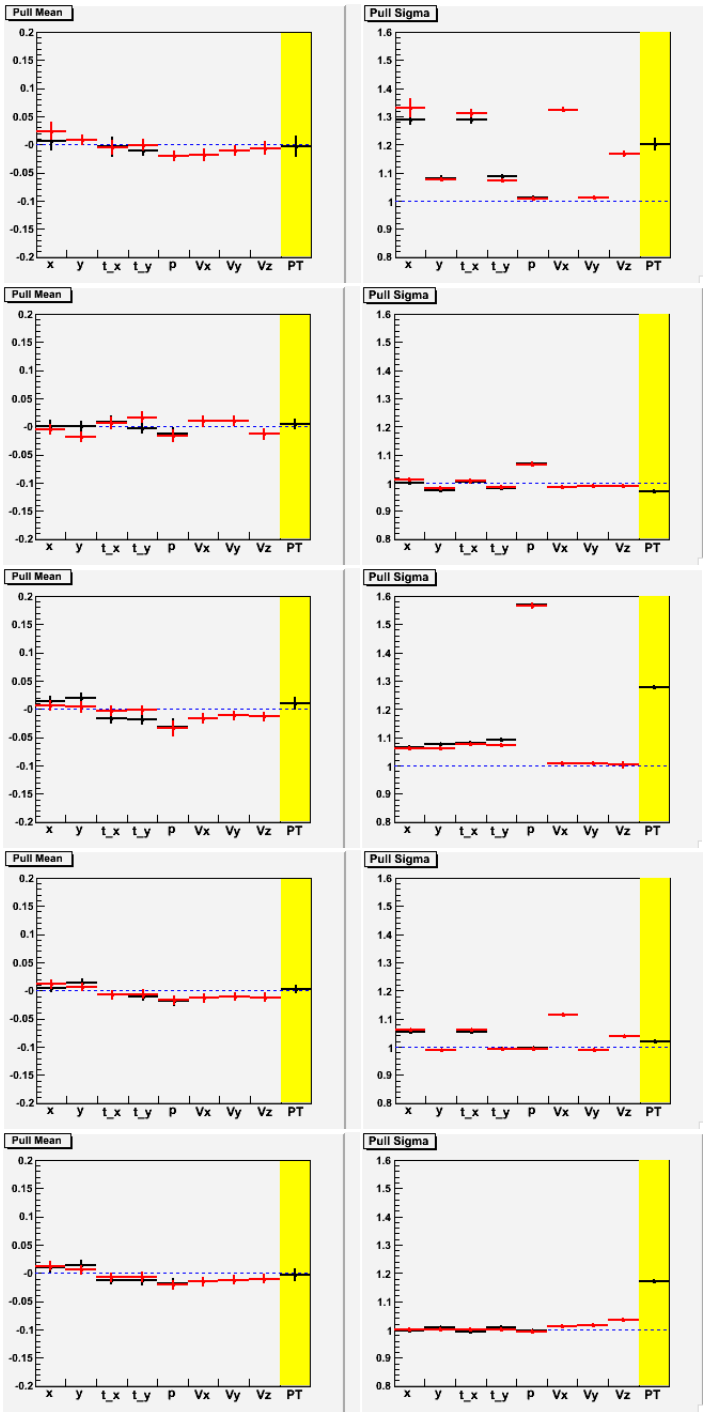

Figure 3.7: Graphical representation of the FITPull parameters (same graphical convention as figure). From top to bottom rows: input fake measurements generated with SF=2 and BIAS=0 on x, t_x, p, V_x and V_z in case of correlated $x - t_x$ and $y - t_y$ track parameters.

function of w. Also in this case for $w \leq 10\%$ most of the events have correct proper time and error.

We have to underline that the second gaussian contribution to the FITPull or to the B proper time MCPull distributions are ascribed to the presence of incorrect measured data (i.e. with under estimated errors). The FITPull method, being a "statistical" method, can only control a sample of several measurements and indicate whether most of the events are well measured. Nothing can be done to eliminate or correct data populating the second gaussian. A cut on the fit χ^2 can only eliminate part of these events (the one populating the tails that contribute to larger χ^2).

3.5 Validation of the FITPull method with reconstructed tracks.

In the previous sections we have shown that the FITPull method is a valid monitor of the input measured quantities. Real tracks will be a much less controlled environment to work with: phase space dependence, non gaussianity, correlation and background are some possible "complications" that can invalidate the FITPull method capability to test measurements.

For this reason in this section we test the FITPull method in a more realistic scenario, by using reconstructed Monte-Carlo tracks. The plot in figure 3.10 shows the MCPull mean and variances as a function of the reconstructed momenta, for the pions produced in $B_d^0 \to \pi^+\pi^-$ decays[4]. Indeed in DC04 data, for a simulation accident [36], tracks were unproperly reconstructed (****), even if track fitting pulls gave satisfactory results. In particular x, t_x and p show momentum and charge dependent BIASes. A slight SF is also affecting reconstructed momentum. We can take advantage of this error to see if the FITPull method monitor is able to put in evidence this effect. From a sample of 100000 (***) $B_d^0 \to \pi^+\pi^-$ Monte Carlo data we combine all reconstructed $\pi^+\pi^-$ pairs and perform a fit with the hypothesis of $B_d^0 \to \pi^+\pi^-$ with the B_d originated from the primary vertex[5]. The combinatorial background is the only source of background we considered. Most of of it is suppressed by choosing $\chi^2 < 10$, but still a fraction $B/(S+B) \approx 0.067$ is present. For simplicity we consider events with only one pp collision with the PV coordinates generated randomly around the true values, like in the previous section.

The FITPulls corresponding to each measurement were fitted with a double gaussian shape in momentum slices and the parameters of the main gaussian are represented in figure. As we hoped the BIAS on x, t_x and p shows up modifying FITPull mean values. Both x and p BIASes are found with the correct sign, while in the case of t_x it appears with opposite sign. The reason for this can be addressed to the $x - t_x$ correlation and the dominance of the x BIAS with respect to the t_x one. In fact simple tests with fake measurements have

[4] in this case the cheated selection is necessary in order to evaluate MCPulls correctly

[5] In this case no cheated selection is performed, as it will be with real data analysis

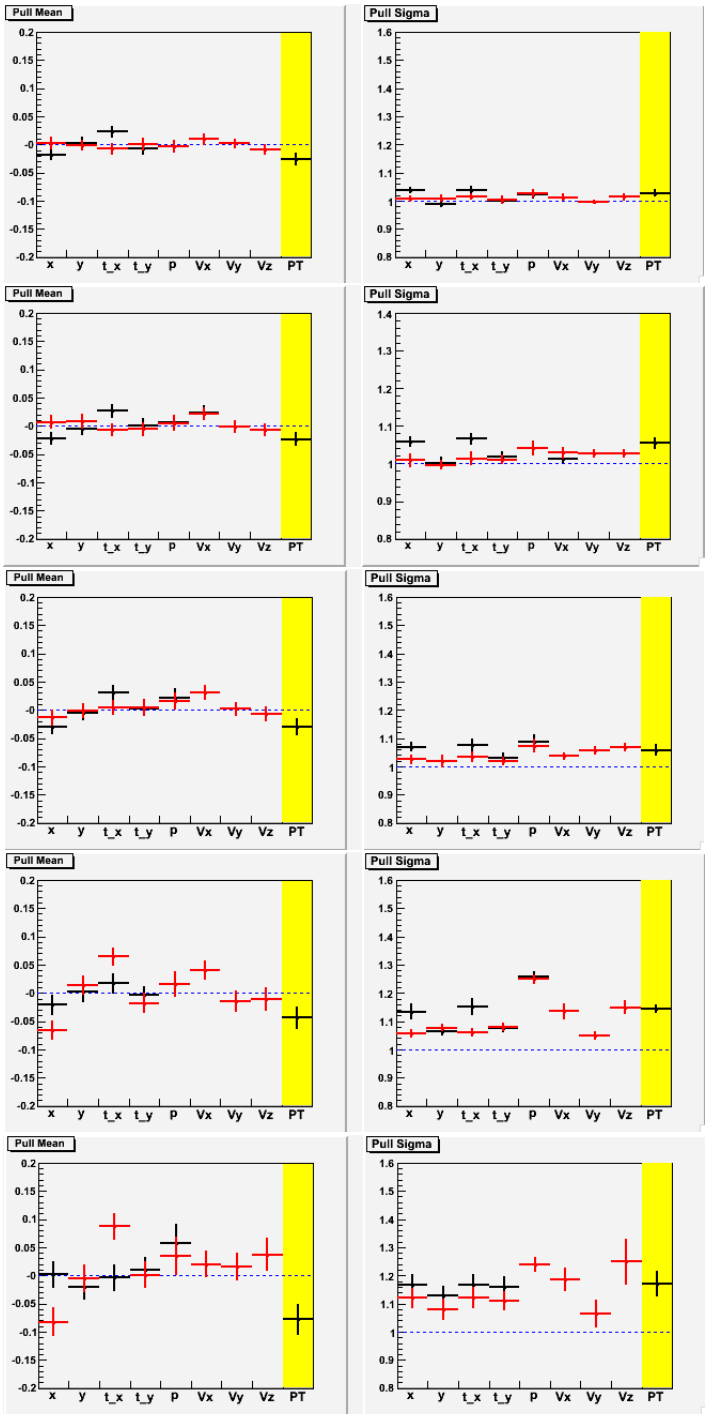

Figure 3.8: FITPull double gaussian fit parameters corresponding to the main gaussian contribution. The same notation of the previous figures is chosen. Input data were generated with increasing tail contribution in all track measurements: from top to bottom 5%, 10%, 15%, 30% and 40%.

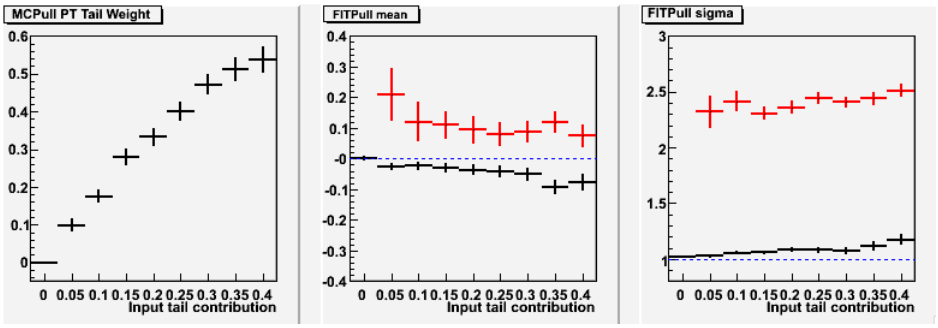

Figure 3.9: Dependence on the track tail input contribution of the proper time MCPull fitted parameters. Left: tail (second gaussian) contribution $1 - w$; center: mean values of the main (black) and second (red) gaussian; right: sigma values of the main (black) and second (red) gaussian.

shown that a bias on x modifies x and t_x FITPull mean values by almost the same quantity with opposite sign (see fig.). The same thing happens in the case of a BIAS on t_x. Quantitatively the absolute FITPull shift is smaller, so we can expect that the overall effect is dominated by the x BIAS and correlation. The $SF \neq 1$ present in the FITPulls can also be explained as due to the input BIAS. In fact tests of section 4.2.2 have shown that input BIASes modified also FITPull variances.
Therefore we can conclude that also in this case the FITPull method succeeds in discovering some measurement errors. In this case also the B proper time would be incorrectly reconstructed: in figure 3.12, the left pad shows the MCPull distribution of the reconstructed proper time. It can be fitted with a double gaussian distribution $(w \cdot G1 + (1-w) \cdot G2)$, where the G2 component is mostly due to combinatorial background. The main component G1 shows an overall $SF \approx 1.27$ (parameter p3) which suggests that proper time error is underestimated, while the BIAS is negligible $0.04\sigma_{PT} \approx 1.6fs$ (parameter p2). In the left plot it is evident that the SF indeed depends on the pion momenta, like input measurement BIASes.

3.6 Recovery potential of the measurement.

All the tests done so far demonstrated that the FITPull method can be used on real data to test the correctness of measurement values and errors down to fraction of resolution scale. Therefore it is a rather sensitive monitor of the measurement reliability. With some limits, FITPulls can also indicate which kind of problem (BIAS or SF) the measurements have. If the problem concerns track parameters we can hope that a further optimization of track fitting will recover it. But if this does not happen, we can investigate the possibility to use the FITPull method to recover the wrong measurements.

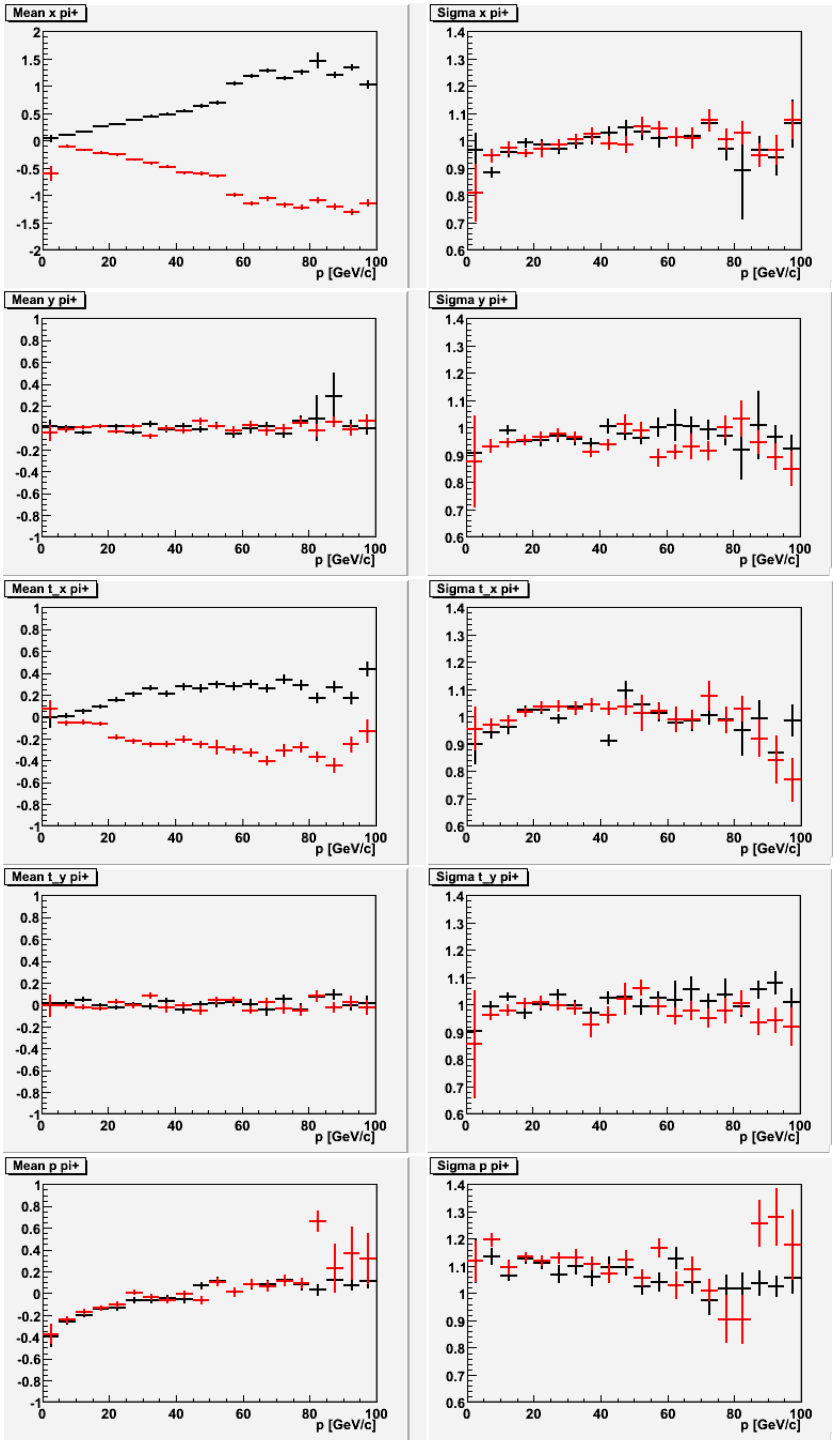

Figure 3.10: MCPull mean values (left) and sigma (right) associated to reconstructed track (x, y, t_x, t_y, p) measurements, obtained by a double gaussian fit to the distributions: red and black data correspond to main gaussian contribution for π^+ and π^- respectively.

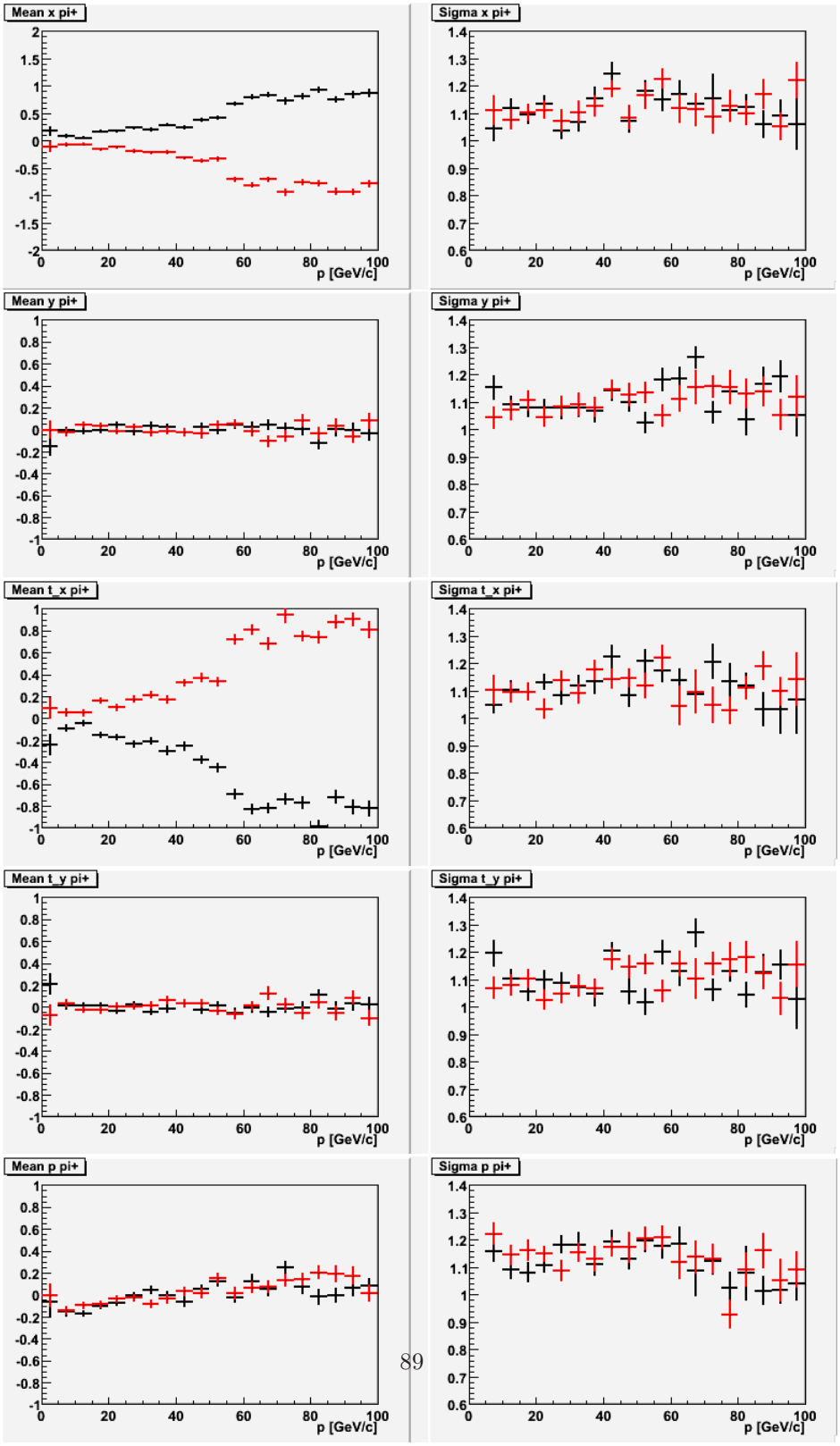

Figure 3.11: FITPull mean values (left) and sigma (right) associated to reconstructed track (x, y, t_x, t_y, p) measurements, obtained by a double gaussian fit to the distributions: red and black data correspond to main gaussian contribution for π^+ and π^- respectively.

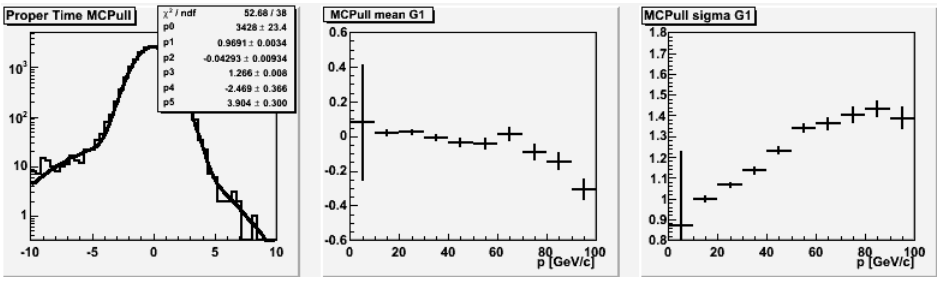

Figure 3.12: B proper time MCPull distribution (left) of $B_d \to \pi^+\pi^-$events selected with a $\chi^2 < 10$. Center and right pads show the mean and sigma MCPull parameters of the main gaussian as a function of the pion momenta.

Given the correlation between the FITPull output we observed, and the fact that quantitatively the FITPulls do not represent the input BIAS or SF, we choose to apply iteratively correction cycles in which, at each step, an input measurement is corrected by the FITPull parameters:

$$\begin{aligned} m_i^k &= m_i^{k-1} + \mathbf{B_i^{k-1}}\sqrt{\mathbf{cov_{ii}^{k-1}}} \\ \mathbf{cov_{ij}^{k}} &= \mathbf{S_i^{k-1}S_j^{k-1}cov_{ij}^{k-1}} \end{aligned} \tag{3.30}$$

where $\mathbf{B_i^{k-1}}$ and $\mathbf{S_i^{k-1}}$ indicate the FITPull BIAS and corresponding SF measured at iteration cycle $k-1$ for measurement i. During iterations BIASes cumulate by adding up, while SFs are multiplied.
Driven by the experience matured with tests on fake measurements, we decide to apply first corrections to fix the BIASes, then to recover the SFs. Moreover, given the self correlations between track measurements, we choose to correct x first, then t_x and p. With these criteria, we consider the case of reconstructed tracks of the previous section. The BIASes shown in figure 3.11 are linearly fitted and the best parameters fed to the correction cycles. During BIAS correction we also observe an improvement of the sigmas. After a few (≈ 10) correction cycles the FITPull parameters are reasonably compatible with BIAS=0 and SF=1. In this situation, we can judge if the correction worked by looking at the MCPull distributions: figure summarizes all the track measurements. We can see that, except t_x bias, which is still slightly biased, all the other measurements recovered almost completely. In this situation also B proper time value and error are better calculated, as is shown in figure 3.14 .

3.7 The $J/\Psi \to \mu\mu$ channel for FITPull calibration and generalization

The FITPull method, as seen in the previous sections, is quite promising, specially with simple decay topology. Up to now we have discussed about the

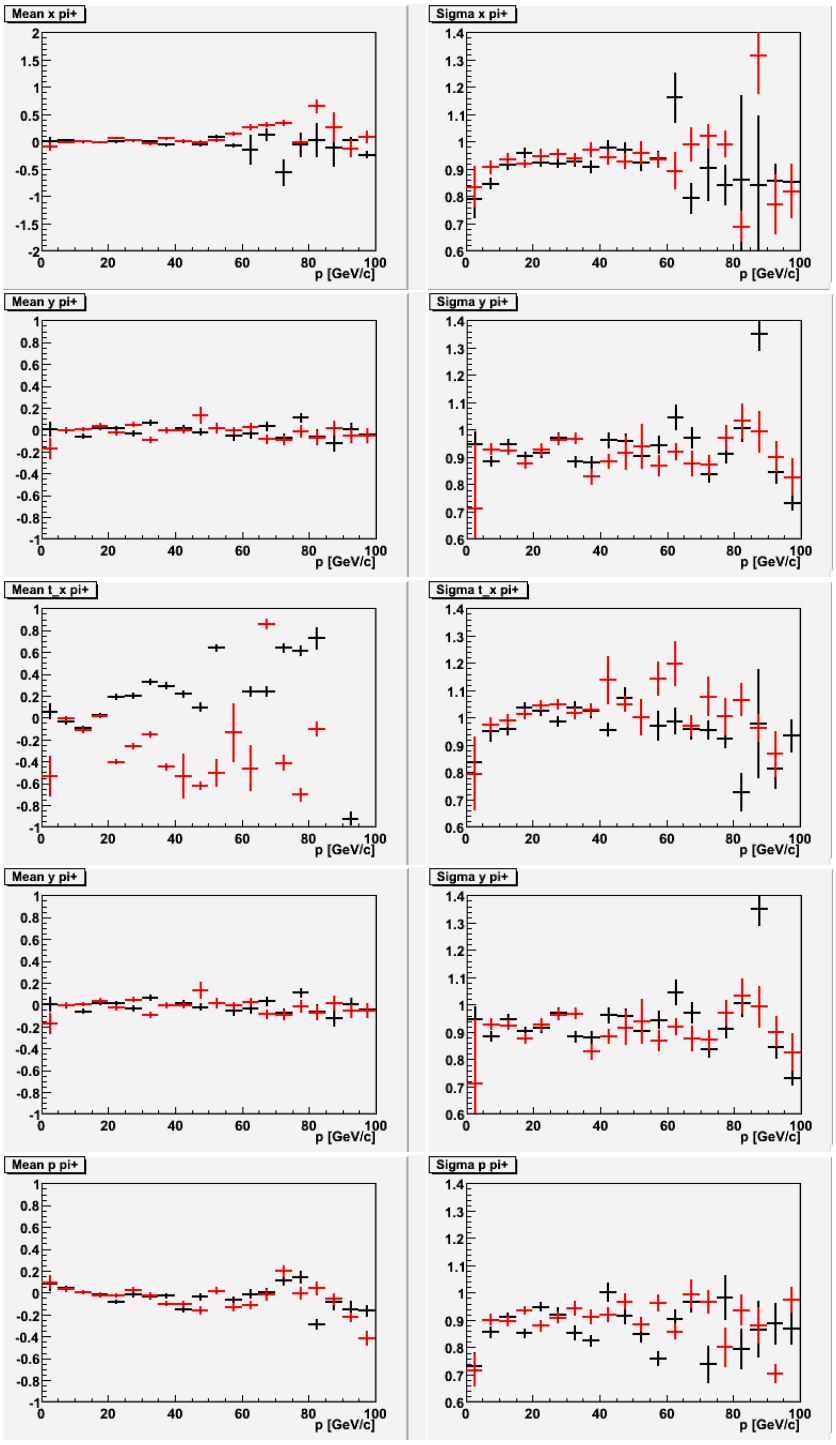

Figure 3.13: MCPull mean values (left) and sigma (right) associated to reconstructed tracks measurements after the correction cycles based on FITPull distributions. Values are obtained by a double gaussian fit to the distributions: red and black data correspond to main gaussian contribution for π^+ and π^- respectively.

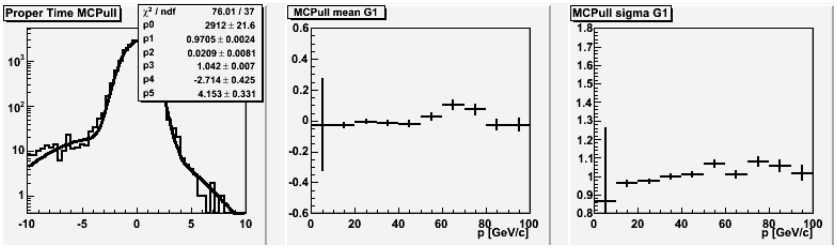

Figure 3.14: B proper time MCPull distribution and parameters after correction.

FITPull method applied to the $B_d \to \pi^+\pi^-$ decay, but the facts are much more complicated. If the FITPull reasoning is correct, the method shouldn't depend on the decay considered.

In our studies we explore in details a possible control channel in order to tune the FITPull capabilities of recovery and detection, since making a calibration for the FITPulls with only a sample of signal should generate a correction method too much "greedy" and focused only on the sample under study. Also a precise determination of the FITPull parameters requires large statistics (especially if one wants to study their phase space dependence) and low background contamination but in LHCb experiment, signals as $B \to \pi\pi$, will not own a large statistics. For all these reasons the use of the FITPull method to monitor or to recover BIASed/SF measurements cannot be performed on the signal decay itself. Thus we have thought to use a control channel that allows FITPull method to become independent from the signal. This approach has the advantage that a high statistic and low background sample can be processed. In case the control sample analysis puts in evidence tracks or vertices BIASes or SFs, the correction found can be exported to the physics channel case.

Therefore our idea is to look for a FITPull parameters (mean, variance) dependence on the input track parameters as a function of the input particle phase space. In this way we can think a correction strategy, built on an clean channel, but exportable to others channels.

We chose the $J/\Psi \to \mu^+\mu^-$channel since the prompt J/Ψ will be a strong signal in dimuon triggered events (˜170Hz@LHCb) with a low background level (B/S˜24%). The only kinematical difference between $J/\psi \to \mu\mu$ and $B \to \pi\pi$ is that the J/ψ is generated in the primary vertex. So we fit prompt $J/\Psi \to \mu^+\mu^-$with common vertex and mass constraint to extract a careful mapping to the corrections of the track parameters as a function of momentum of the particle. We have prepared an iterative method to extract, starting from the FITPull distributions, a map of the adjustments of the input track parameters as a momentum function in the decay $J/\Psi \to \mu^+\mu^-$.
Applying this iterative procedure, with a shell script, we obtain 10 maps (or histograms) of corrections for the input track parameters. At first itera-

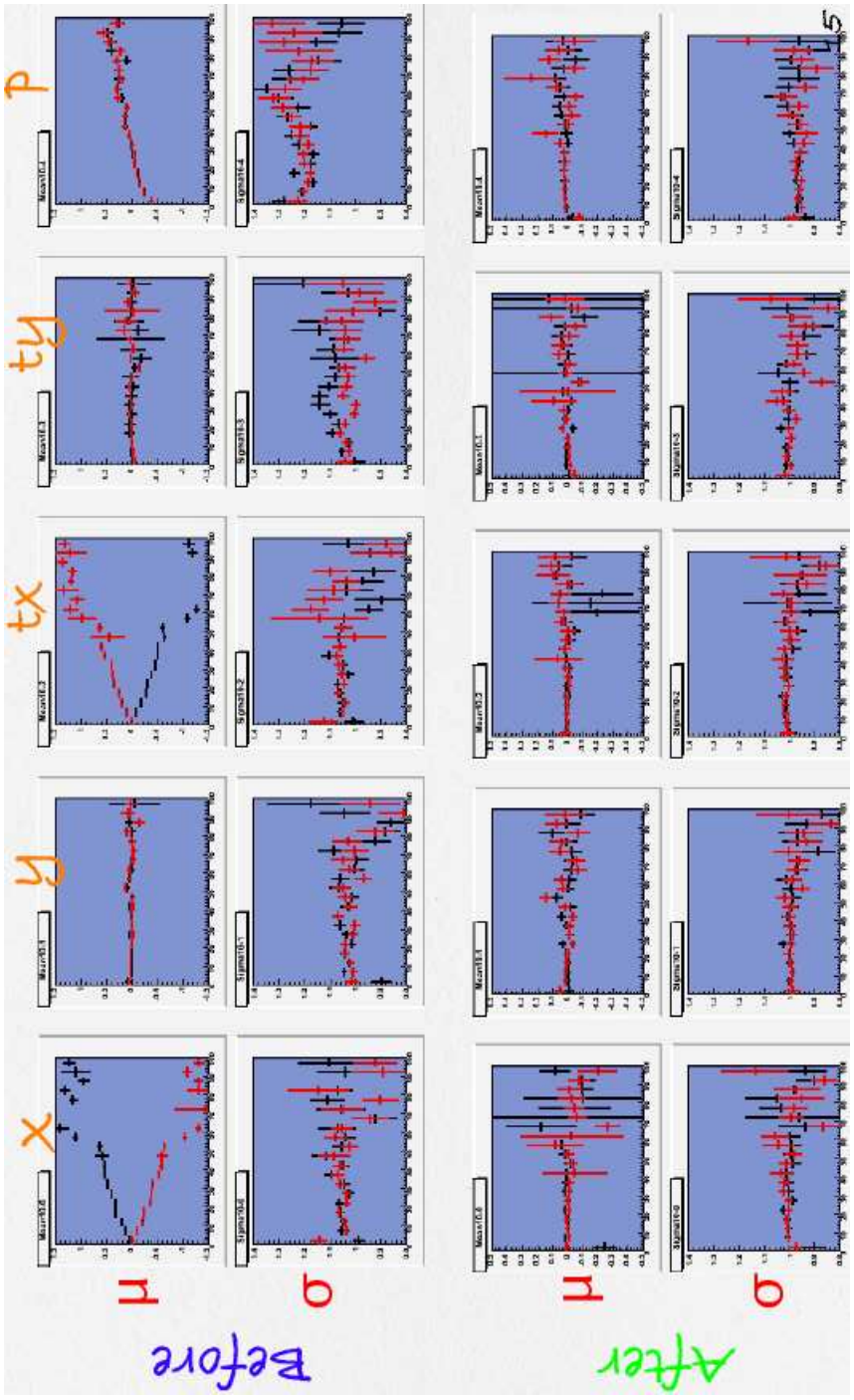

Figure 3.15: $J/\Psi \to \mu\mu$ FITPulls before and after the 32^{nd} correction.

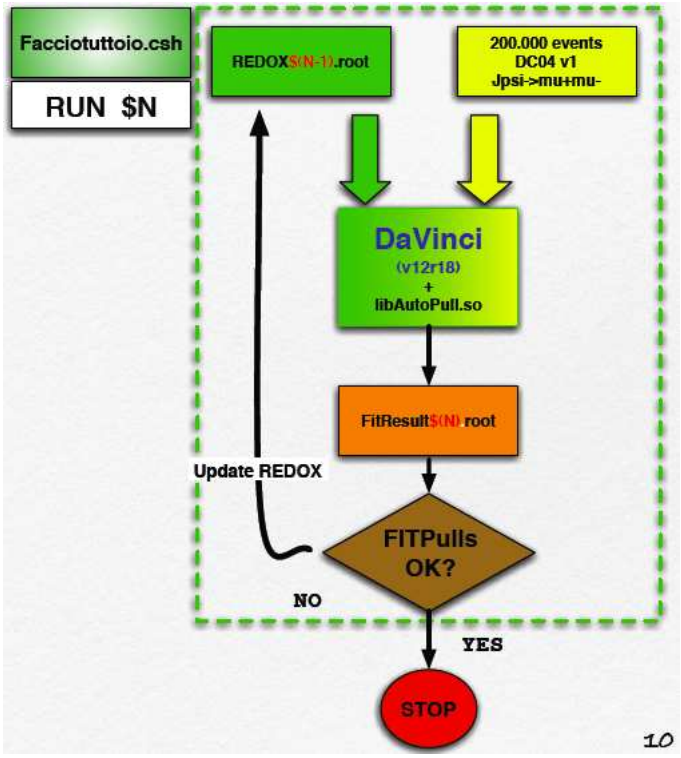

Figure 3.16: *FaccioTuttoio.csh* The procedure to determine the correction histograms.

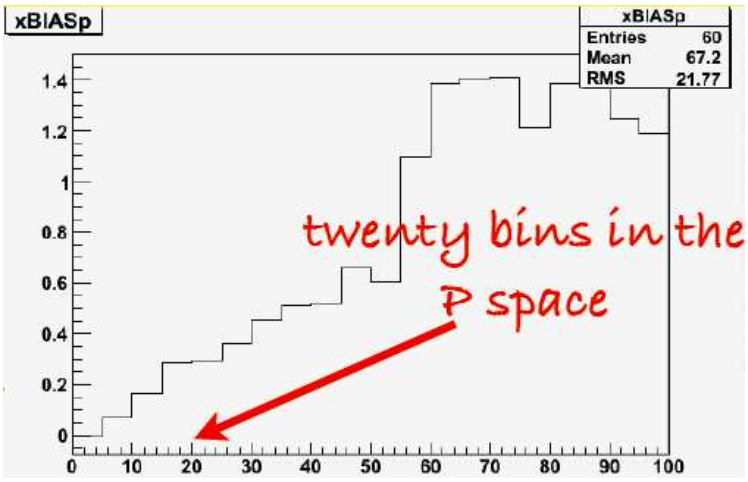

Figure 3.17: One of the ten correction histograms. In this image, the correction to be applied on the X bias is depicted as a function of the momentum (1-100 GeV/c).

tion the program takes the muons form the DSTs and performs, by means of `GlobalFitter`, the vertex fit for each muon couple and the FITPulls for each input parameter. All the fit informations are stored in a big root file. At the next iteration, the DST data is adjusted, before the `GlobalFitter,` taking into account the correction coming from the foregoing iteration. The work sequence of the script is structured in wise to recovery firstly the BIASes and then the SFs.

This loop is iterated until the FITPulls are all corrected[6]. With our sample of 200000 events $J/\Psi \rightarrow \mu^+\mu^-$ we reach the desired convergence[7] after 33 iterations. The final product of this procedure is a set of histograms[8] which contains all the corrective factors to be applied to the DST data in order to obtain gaussian FITPulls from the `GlobalFitter`. The following step was applying the correction histograms, obtained from the 33^{rd} iteration on the J/ψ sample, to two different samples: $B_d \rightarrow \pi^+\pi^-$(200.000 events) and the $B_s \rightarrow D_s\pi$(300.000 events) and evaluating the effects. The figure 3.18 demonstrates that it is possible to export the correction found out with the J/ψ sample to other channels. The validity of this method can be stated observing the consequences on the MCPulls for the propertime before and after the corrections.

[6]The conditions of convergence have to be defined in relation to physical requirements. Thus the next chapter can help us.

[7]For the $J/\psi \rightarrow \mu\mu$ we chose to stop the script just as soon as all the track parameters x, y, t_x, t_y, p have been recovered.

[8]Instead of the histograms, we could generate a mathematical function for each parameter, which contains the dependence of the BIAS or the SF from the momentum of the decaying particles.

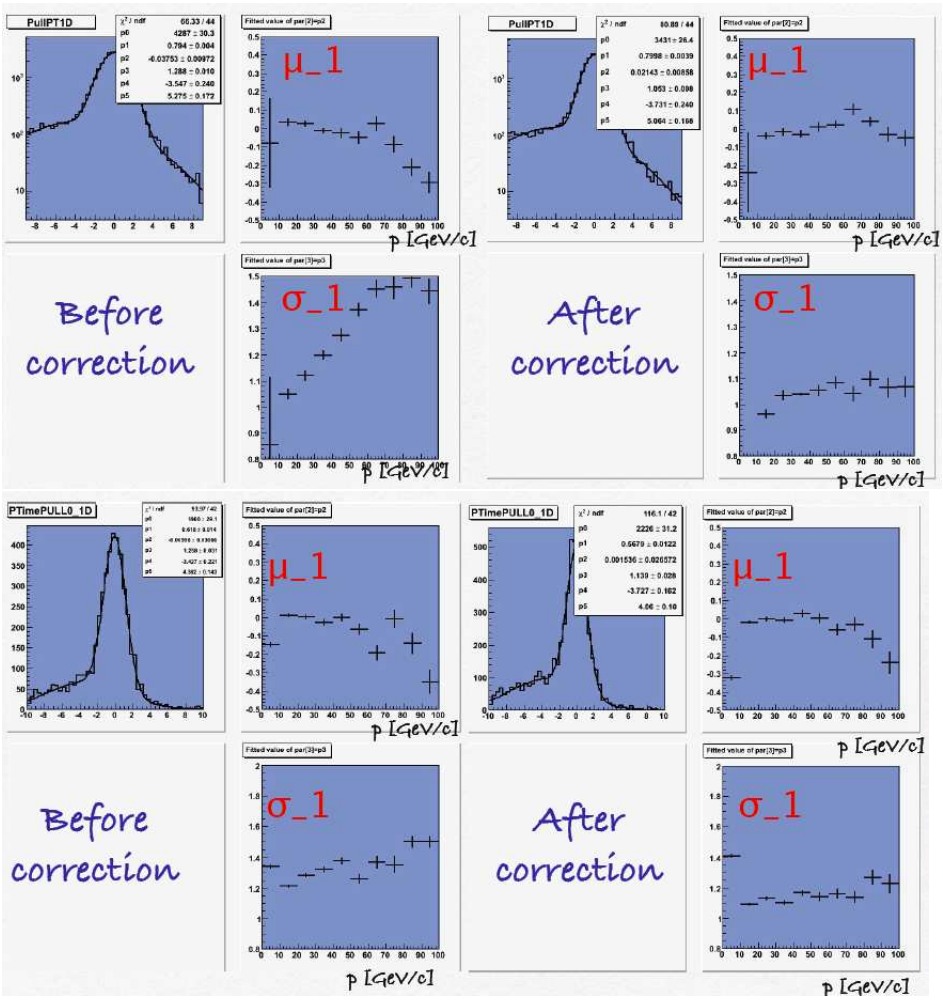

Figure 3.18: MCPulls for the proper time for the $B_d \to \pi\pi$ and $B_s \to D_s\pi$, before and after the correction coming from the $J/\Psi \to \mu\mu$ analysis.

3.8 B proper time resolution and calibration

So far we have shown that FITPulls can test the correctness of the measurements in a given decay channel. If they are canonically distributed they guarantee that input measurements are correct and, indirectly, that the B proper time measurement is reliable. On the other hand, if FITPulls are not canonical it means that some input measurements have a problem, which probably also affect proper time measurement. In this section we want to give some more quantitative study on the dependence of proper time calculation on the input measurement BIAS or SF. For this reason, taking advantage of the fake measurement generation, we vary the SF and the BIAS of the most relevant measurements and we plot the proper time MCPull parameters mean and sigma. The plots on the left column in figure 3.19 summarize the proper time dependence on the input BIAS (ranging from -2.0 to 2.0) of single measurements V_z, x, t_x and p. Like before, in case of x and t_x the bias is charge dependent. Correspondingly in the right column are plotted the results of SF dependence (with values 0.2, 0.5, 1.0, 2.0 and 5.0).
As we already noticed in section 4 proper time has a different response to different variables BIAS or SF. If one decides that a $BIAS < 0.1$ and $SF - 1 < 0.1$ correspond to a good proper time measurement, these plots can help us to to fix some limits to the input BIAS or SF which then can be translated to requirements on the FITPulls parameters.

3.9 Some considerations about the FITPulls

In this note we have described the possibility to use kinematical/geometrical fits and their output FITPull distributions to check the correctness of input measurements and errors on real data. In fact the FITPulls are normal gaussians if the input measurements and errors are correctly defined, while they deviate from being normal gaussians in presence of BIASes or Scale Factors in the input measurements or errors. Unfortunately the determination of the affected measurement is not always unique due to the correlations between measurements and the fit constraints.
The validity of this method has been proved in several tests performed with Monte Carlo data corresponding to the decay channel $B_d^0 \to \pi^+\pi^-$. The studies made on data generated according a well known distribution (fake measurements) allowed us to understand the features and the limits of the method in a simple way. The test on reconstructed Monte Carlo data have demonstrated that also in a more realistic case the FITPull monitor can be useful to discover incorrect measurements. In this case we have also shown that an almost total recovery of the corrupted measurements can be obtained by means of an iterative correction procedure obtained from an independent $J/\psi \to \mu^+\mu^-$ analysis.

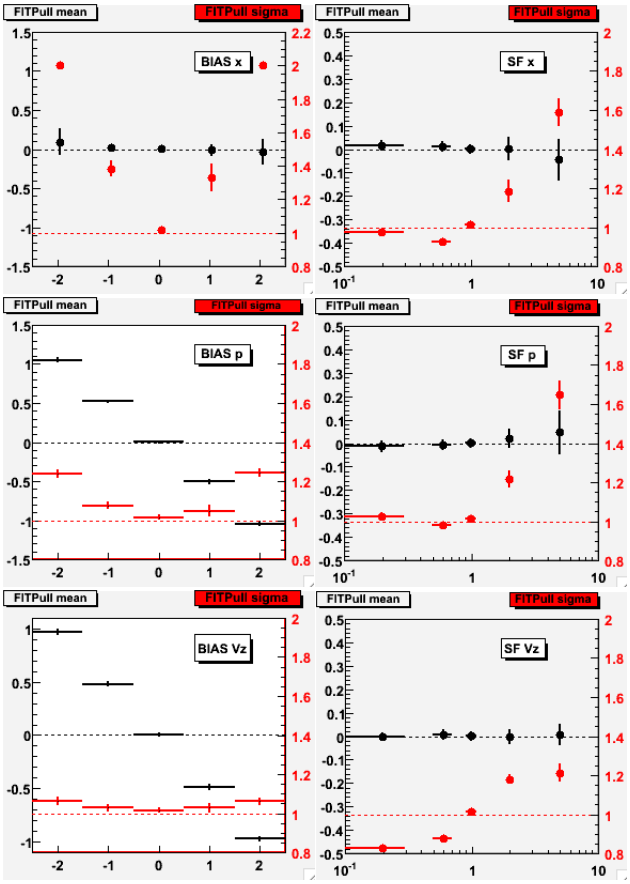

Figure 3.19: B proper time MCPull parameters mean and sigma as a function of input BIASes (left plots) and SFs (right plots) on track measurement x, t_x, p and on vertex. The simulated events correspond to $B_d \to \pi^+\pi^-$ channel and the measurements are obtained by a gaussian smearing of the Monte Carlo truth informations (Fake measurements).

Chapter 4

B proper time importance for time dependent analysis

4.1 Time dependent CP asymmetries and decay rates: from theory to experiment

The most general formula for the time dependent CP asymmetry in a generic $B \to g$ decay, where g is the a generic final state, is given by:

$$A_{CP}(t) = \frac{\Gamma\left(B(t) \to g\right) - \Gamma\left(\bar{B}(t) \to \bar{g}\right)}{\Gamma\left(B(t) \to g\right) + \Gamma\left(\bar{B}(t) \to \bar{g}\right)}$$

From an experimental point of view the asymmetry can be measured as:

$$A_{CP}^{exp}(t) = \frac{N_B(t) - N_{\bar{B}}(t)}{N_B(t) + N_{\bar{B}}(t)} \tag{4.1}$$

where N_B and $N_{\bar{B}}$ are the number of tagged B ($\bar{B}$) events that decay at the time t. Three factors fix the experimental capability to evaluate this asymmetry:

1. the B flavour tagging;
2. the statistics of the observed events (signal + background);
3. the B decay proper time resolution .

The knowledge of the initial flavour of the reconstructed B meson is necessary and this task is performed by means of the tagging procedure described in par. 1.3.2.

The sensitivity to the A_{CP} measurements is determined undoubtedly, by the statistics and the ratio B/S as reported in [24].

Finally there is another element which plays an important role in this general description: the proper time resolution. In the next paragraph we will see how the proper time determines a reduction of the asymmetry and a phase shift of the A_{CP} trigonometric components.

4.2 Time dependent analyses of decay rates or CP asymmetries

In this section I give an analytical description of all the detector contributions which contribute to the B decay rates and hence in the A_{CP} calculuses. Generally, given a B decay channel, considering the decay and the mixing effects, we can study 4 different decay transitions[1]:

$$\Gamma_{true}(B(t) \to g)$$

$$\Gamma_{true}(\bar{B}(t) \to \bar{g})$$

$$\Gamma_{true}(B(t) \to \bar{g})$$

$$\Gamma_{true}(\bar{B}(t) \to g)$$

In order to obtain the observed decay rates as a function of the measured proper time (τ), the true rates are convolved for the proper time resolution. If we assume a gaussian resolution model $G(t-\tau, \sigma_\tau)$, the equations become :

$$\Gamma^{'}_{obs}(B(\tau) \to g) = G(t-\tau;\sigma_\tau) \otimes [\Gamma_{true}(B(t) \to g)] \tag{4.2}$$

$$\Gamma^{'}_{obs}(\bar{B}(\tau) \to \bar{g}) = G(t-\tau;\sigma_\tau) \otimes \left[\Gamma_{true}(\bar{B}(t) \to \bar{g})\right] \tag{4.3}$$

$$\Gamma^{'}_{obs}(B(\tau) \to \bar{g}) = G(t-\tau;\sigma_\tau) \otimes [\Gamma_{true}(B(t) \to \bar{g})] \tag{4.4}$$

$$\Gamma^{'}_{obs}(\bar{B}(\tau) \to g) = G(t-\tau;\sigma_\tau) \otimes \left[\Gamma_{true}(\bar{B}(t) \to g)\right] \tag{4.5}$$

Moreover $\Gamma^{'}_{obs}$ are multiplied by the $\epsilon(\tau)$, in order to take into account the experimental acceptance, that, due to the trigger system, shows a dependence on the proper time.

As seen in par.1.3.2, the B flavour tagging is characterized by an efficiency ϵ_{tag} and a mistag probability ω_{tag}. For the tagged events, the four foregoing equations are mixed giving the four observed rates:

$$\Gamma_{obs}(tagged\ B(\tau) \to g) = \epsilon(\tau)\cdot\epsilon_{tag}\left[(1-\omega_{tag})\Gamma^{'}_{obs}(B(\tau) \to g) + \omega_{tag}\Gamma^{'}_{obs}(\bar{B}(\tau) \to g)\right] \tag{4.6}$$

$$\Gamma_{obs}(tagged\ \bar{B}(\tau) \to \bar{g}) = \epsilon(\tau)\cdot\epsilon_{tag}\left[(1-\omega_{tag})\Gamma^{'}_{obs}(\bar{B}(\tau) \to \bar{g}) + \omega_{tag}\Gamma^{'}_{obs}(B(\tau) \to \bar{g})\right] \tag{4.7}$$

[1]The subscript "true" refers to values without experimental uncertainties, while the subscript "obs" refers to observed values.

$$\Gamma_{obs}(tagged\, B(\tau) \to \bar{g}) = \epsilon(\tau)\cdot\epsilon_{tag}\left[(1-\omega_{tag})\Gamma^{'}_{obs}(B(\tau)\to\bar{g}) + \omega_{tag}\Gamma^{'}_{obs}(\bar{B}(\tau)\to\bar{g})\right] \tag{4.8}$$

$$\Gamma_{obs}(tagged\, \bar{B}(\tau) \to g) = \epsilon(\tau)\cdot\epsilon_{tag}\left[(1-\omega_{tag})\Gamma^{'}_{obs}(\bar{B}(\tau)\to g) + \omega_{tag}\Gamma^{'}_{obs}(B(\tau)\to g)\right] \tag{4.9}$$

while the untagged events follow the formulas:

$$\Gamma_{obs}(untagged\, B/\bar{B}(\tau)\ \to g) = \epsilon(\tau)\cdot(1-\epsilon_{tag})\left[\Gamma^{'}_{obs}(B(\tau)\to g) + \Gamma^{'}_{obs}(\bar{B}(\tau)\to g)\right] \tag{4.10}$$

$$\Gamma_{obs}(\text{untagged}\, B/\bar{B}(\tau)\ \to \bar{g}) = \epsilon(\tau)\cdot(1-\epsilon_{tag})\left[\Gamma^{'}_{obs}(\bar{B}(\tau)\to \bar{g}) + \Gamma^{'}_{obs}(B(\tau)\to \bar{g})\right] \tag{4.11}$$

Therefore with the foregoing equations we have shown the actual rates that we will observe experimentally. With a set of this information, we can turn our attention to two different applications. We will study how the decay rates are modified in virtue of the physical properties of the two different cases.

4.2.1 Flavour specific decay: $B_s \to D_s\pi$

In a flavour specific process, like $B^0_s \to D^-_s\pi^+$ and $\overline{B}^0_s \to D^+_s\pi^-$, only $B^0 \to g$ and $\bar{B}^0 \to \bar{g}$ are allowed, whereas the $\bar{B}^0 \to g$ and $B^0 \to \bar{g}$ events are forbidden. These features involve some simplifications in the Γ_{true} expressions. Reminding the par. 2.3.1 we can set

$$\lambda_f = \bar{\lambda}_{\bar{f}} = 0 \tag{4.12}$$

and the equations 2.33, 2.32, 2.35, 2.34 can be simplified:

$$I_+(t) = \bar{I}_+(t) = \cosh\frac{\Delta\Gamma}{2}t \tag{4.13}$$

$$I_-(t) = \bar{I}_-(t) = \cos\Delta m t \tag{4.14}$$

Thus the time dependence of the tagged B decay rate is given by:

$$\Gamma_{obs}\,(tagged\, B(\tau)\to g) \propto e^{-\Gamma t}\left[\cosh\left(\frac{\Delta\Gamma}{2}t\right) + (1-2\omega_{tag})\cos\Delta m t\right]\otimes G(t-\tau;\sigma_\tau)$$

and similarly for the tagged $\bar{B}$ rate.

In this formula we can notice three main elements:

1. A damping factor $e^{-\Gamma t}$, given by the B decay, with mean lifetime $1/\Gamma$.
2. A hyperbolic cosine term that takes into account of the width differences $\Delta\Gamma$ between B and $\bar{B}$.
3. An oscillatory term $\cos\Delta m\, t$ that modulates the shape of the decay exponential due to the mixing $B/\bar{B}$. The oscillation amplitude is determined by the experimental factor ω_{tag}(namely ω in the following).

The proper time resolution effects are accounted by the convolution with the function G, that transforms the true proper lifetime t into the observed one τ,

$$\frac{1}{\sqrt{2\pi}\sigma_\tau} e^{-\frac{(\tau-t)^2}{2\sigma_\tau^2}} \tag{4.15}$$

Developing the integration, the decay rate of $B \to g$ becomes[2]:

$$\begin{aligned}\Gamma_{obs}\left(tagged\, B(\tau)\to g\right) \propto \int_{-\infty}^{\infty} e^{-\Gamma t}\left[\cosh\left(\frac{\Delta\Gamma}{2}t\right)+(1-2\omega)\cos\Delta m t\right]\cdot\frac{1}{\sqrt{2\pi}\sigma_\tau}e^{-\frac{(\tau-t)^2}{2\sigma_\tau^2}}dt = \\ = \sqrt{2}\cdot e^{-\Gamma\tau}\left\{e^{+\frac{\Gamma^2\sigma_\tau^2}{2}+\frac{\Delta\Gamma^2\sigma_\tau^2}{8}}\cosh\left(\frac{\Delta\Gamma}{2}\cdot\tau-\frac{\Delta\Gamma}{2}\cdot\Gamma\cdot\sigma_\tau^2\right)+\right. \\ \left.+(1-2\omega)\cdot e^{\frac{\sigma_\tau^2\Gamma^2}{2}}\cdot e^{-\frac{\sigma_\tau^2\Delta m^2}{2}}\cos\left(\tau\Delta m-\Gamma\Delta m\sigma_\tau^2\right)\right\}\end{aligned} \tag{4.16}$$

where the rate is a function of Γ, $\Delta\Gamma$, Δm, ω, σ_τ. Comparing this formula with the one without the convolution, we can notice that the resolution adds phases in the cos and cosh terms and it also adds two corresponding dilution factors: $e^{-\frac{\sigma_\tau^2\Delta m^2}{2}}$ and $e^{+\frac{\sigma_\tau^2\Delta\Gamma^2}{8}}$ [3] . We will see its importance in the CP asymmetry computation.

If the measured B decay proper time is affected by a bias b

$$b = \sigma_\tau\cdot\Sigma$$

The equation above is modified as following:

$$\begin{aligned}\Gamma_{obs}\left(B(\tau)\to g\right) \propto \sqrt{2}\cdot e^{-\Gamma\tau}\cdot e^{\frac{\sigma_\tau^2\Gamma^2}{2}-\frac{\tau\Sigma\tau}{\sigma_\tau}+\Gamma\sigma_\tau\Sigma}\cdot\left\{e^{+\frac{\sigma_\tau^2\Delta\Gamma^2}{8}}\cosh\left(\frac{\Delta\Gamma\tau}{2}-\frac{\Delta\Gamma}{2}\cdot\Gamma\cdot\sigma_\tau^2-\frac{\Delta\Gamma\sigma_\tau\Sigma}{2}-\frac{\tau\Sigma}{\sigma_\tau}\right)+\right. \\ \left.+(1-2\omega)\cdot e^{-\frac{\sigma_\tau^2\Delta m^2}{2}}\cdot\cos\left(\tau\Delta m-\Gamma\Delta m\sigma_\tau^2-\Delta m\sigma_\tau\Sigma\right)\right\}\end{aligned} \tag{4.17}$$

[2]For details see in Appendix

[3]The factor $e^{\frac{\sigma_\tau^2\Gamma^2}{2}}$ is negligible since it is very close to 1.

that is very similar to eq. 4.16. In this case the rate is a function of Γ, $\Delta\Gamma$, Δm, ω, σ_τ and also of Σ. So the bias introduces a further phase in the cosine arguments and a further common damping factor $e^{-\frac{\tau\Sigma_\tau}{\sigma_\tau}+\Gamma\sigma_\tau\Sigma}$.

With this knowledge, the time dependent CP asymmetry, for this channel, has been transformed from the theoretical expression

$$A_{CP}^{th}(t) = \frac{\cos(\Delta m\, t)}{\cosh(\Delta\Gamma \cdot t/2)}$$

to the experimental form:

$$A_{CP}(\tau) = e^{-\frac{\sigma_\tau^2\Delta m^2}{2}} \cdot e^{-\frac{\sigma_\tau^2\Delta\Gamma^2}{8}} \cdot \frac{(1-2\omega)\cdot\cos\left(\tau\Delta m - \Gamma\Delta m\sigma_\tau^2 - \Delta m\sigma_\tau\Sigma\right)}{\cosh\left(\frac{\Delta\Gamma\tau}{2} - \frac{\Delta\Gamma}{2}\cdot\Gamma\cdot\sigma_\tau^2 - \frac{\Delta\Gamma\sigma_\tau\Sigma}{2} - \frac{\tau\Sigma}{\sigma_\tau}\right)} \tag{4.18}$$

4.2.2 B decays in CP eigenstates

In this section we consider the general neutral B decay into a final CP eigenstate $|f\rangle$, satisfying the condition

$$CP\,|f\rangle = \eta\,|f\rangle \tag{4.19}$$

The quantity under study, independent on any phase conventions and full of physical meaning, is λ_f as reported in eq. 2.36. If CP is violated if $\lambda_f \neq \pm 1$, even if $|\lambda_f| = 1$.

For the B neutral system, CP violation in the interference between decays with and without mixing can be observed by comparing decays into final CP eigenstates of a time-evolving neutral state that begins B^0 at time zero as to those of the state that begins as a $\overline{B}^0$ (see [15]):

$$\Gamma_{true}(B(t)\to f) \propto e^{-\Gamma t}|A_f|^2\left(\left(1+|\lambda_f|^2\right)\cosh\frac{\Delta\Gamma}{2}t + \left(1-|\lambda_f|^2\right)\cos\Delta m\, t + \right.$$
$$\left. -2\mathrm{Re}(\lambda)\sinh\frac{\Delta\Gamma}{2}t - 2\mathrm{Im}(\lambda_f)\sin\Delta m\, t\right)$$

$$\Gamma_{true}(\overline{B}(t)\to f) \propto e^{-\Gamma t}|A_f|^2\left|\frac{p}{q}\right|^2\left(\left(1+|\lambda_f|^2\right)\cosh\frac{\Delta\Gamma}{2}t - \left(1-|\lambda_f|^2\right)\cos\Delta m\, t + \right.$$
$$\left. -2\mathrm{Re}(\lambda)\sinh\frac{\Delta\Gamma}{2}t + 2\mathrm{Im}(\lambda_f)\sin\Delta m\, t\right)$$

Assuming the simplification $|p/q| = 1$, we can introduce the contribution due to the proper time resolution and the mistag effects ω:

$$\Gamma_{obs}\left(tagged\, B(\tau) \to f\right) \propto e^{-\Gamma t}\left(\left(1+|\lambda_f|^2\right)\cosh\frac{\Delta\Gamma}{2}t + (1-2\omega)\left(1-|\lambda_f|^2\right)\cos\Delta m\, t + \right.$$
$$\left. -2\mathrm{Re}(\lambda)\sinh\frac{\Delta\Gamma}{2}t - (1-2\omega)\,2\mathrm{Im}(\lambda_f)\sin\Delta m\, t\right) \otimes \frac{1}{\sqrt{2\pi}\sigma_\tau}e^{-\frac{(\tau-t)^2}{2\sigma_\tau^2}} =$$
$$= e^{\frac{\sigma_\tau^2\Delta\Gamma^2}{8}+\frac{\sigma_\tau^2\Gamma^2}{2}-\Gamma\tau}\cdot\left(\left(1+|\lambda_f|^2\right)\cosh\left(\frac{\Delta\Gamma}{2}\tau-\frac{\Delta\Gamma}{2}\Gamma\sigma_\tau^2\right) - 2\mathrm{Re}(\lambda_f)\sinh\left(\frac{\Delta\Gamma}{2}\tau-\frac{\Delta\Gamma}{2}\Gamma\sigma_\tau^2\right)\right) +$$
$$+ (1-2\omega)\, e^{\frac{\Gamma^2\sigma_\tau^2}{2}-\frac{\sigma_\tau^2\Delta m^2}{2}-\Gamma\tau}\left(\left(1-|\lambda_f|^2\right)\cos\left(\Delta m\,\tau-\Delta m\Gamma\sigma_\tau^2\right) - 2\mathrm{Im}(\lambda_f)\sin\left(\Delta m\,\tau-\Delta m\,\Gamma\sigma_\tau^2\right)\right) \tag{4.20}$$

$$\Gamma_{obs}\left(tagged\,\overline{B} \to f\right) \propto e^{-\Gamma t}\left(\left(1+|\lambda_f|^2\right)\cosh\frac{\Delta\Gamma}{2}t - (1-2\omega)\left(1-|\lambda_f|^2\right)\cos\Delta m\, t + \right.$$
$$\left. -2\mathrm{Re}(\lambda)\sinh\frac{\Delta\Gamma}{2}t + (1-2\omega)\,2\mathrm{Im}(\lambda_f)\sin\Delta m\, t\right) \otimes \frac{1}{\sqrt{2\pi}\sigma_\tau}e^{-\frac{(\tau-t)^2}{2\sigma_\tau^2}} =$$
$$\Gamma_{obs}\left(tagged\,\overline{B} \to f\right) \propto e^{\frac{\sigma_\tau^2\Delta\Gamma^2}{8}+\frac{\sigma_\tau^2\Gamma^2}{2}-\Gamma\tau}\cdot\left(\left(1+|\lambda_f|^2\right)\cosh\left(\frac{\Delta\Gamma}{2}\tau-\frac{\Delta\Gamma}{2}\Gamma\sigma_\tau^2\right) - 2\mathrm{Re}(\lambda_f)\sinh\left(\frac{\Delta\Gamma}{2}\tau-\frac{\Delta\Gamma}{2}\Gamma\sigma_\tau^2\right)\right) +$$
$$- (1-2\omega)\, e^{\frac{\Gamma^2\sigma_\tau^2}{2}-\frac{\sigma_\tau^2\Delta m^2}{2}-\Gamma\tau}\left(\left(1-|\lambda_f|^2\right)\cos\left(\Delta m\,\tau-\Delta m\Gamma\sigma_\tau^2\right) - 2\mathrm{Im}(\lambda_f)\sin\left(\Delta m\,\tau-\Delta m\,\Gamma\sigma_\tau^2\right)\right) \tag{4.21}$$

The time dependent CP asymmetry, for this channel, has been transformed from the theoretical expression

$$A_{CP}^{th}(t) = \frac{\Gamma_{true}(B^0(t)\to f) - \Gamma_{true}(\overline{B}^0(t)\to f)}{\Gamma_{true}(B^0(t)\to f) + \Gamma_{true}(\overline{B}^0(t)\to f)} = \frac{A_{CP}^{dir}\cos(\Delta m\, t) + A_{CP}^{mix}\sin(\Delta m\, t)}{\cosh(\Delta\Gamma\cdot t/2) - A_{CP}^{\Delta}\sinh(\Delta\Gamma\cdot t/2)}$$

where

$$A_{CP}^{dir} = \frac{1-|\lambda_f|^2}{1+|\lambda_f|^2} \qquad A_{CP}^{mix} = \frac{2\mathrm{Im}(\lambda_f)}{1+|\lambda_f|^2} \qquad A_{CP}^{\Delta} = \frac{2\mathrm{Re}(\lambda_f)}{1+|\lambda_f|^2}$$

to the experimental form:

$$A_{CP}^{exp}(\tau) = (1-2\omega)\, e^{-\frac{\sigma_\tau^2\Delta m^2}{2}-\frac{\sigma_\tau^2\Delta\Gamma^2}{8}}\cdot\frac{A_{CP}^{dir}\cdot\cos\left(\Delta m\,\tau-\Delta m\Gamma\sigma_\tau^2\right) + A_{CP}^{mix}\sin\left(\Delta m\,\tau-\Delta m\,\Gamma\sigma_\tau^2\right)}{\cosh\left(\frac{\Delta\Gamma}{2}\tau-\frac{\Delta\Gamma}{2}\Gamma\sigma_\tau^2\right) - A_{CP}^{\Delta}\sinh\left(\frac{\Delta\Gamma}{2}\tau-\frac{\Delta\Gamma}{2}\Gamma\sigma_\tau^2\right)}$$

We can conclude observing that, in the case of a bias in the proper time distribution, A_{CP}^{exp} is modified as:

$$A_{CP}^{exp}(\tau) = (1-2\omega)\, e^{-\frac{\sigma_\tau^2 \Delta m^2}{2} - \frac{\sigma_\tau^2 \Delta\Gamma^2}{8}} \cdot \frac{A_{CP}^{dir} \cdot \cos\left(\Delta m\, \tau - \Delta m \Gamma \sigma_\tau^2 + \Delta m \frac{\Sigma}{\sigma_\tau}\right) + A_{CP}^{mix} \sin\left(\Delta m\, \tau - \Delta m\, \Gamma \sigma_\tau^2 + \Delta m \frac{\Sigma}{\sigma_\tau}\right)}{\cosh\left(\frac{\Delta\Gamma}{2}\tau - \frac{\Delta\Gamma}{2}\Gamma\sigma_\tau^2 + \frac{\Delta\Gamma}{2}\Sigma\sigma_\tau\right) - A_{CP}^{\Delta} \sinh\left(\frac{\Delta\Gamma}{2}\,\tau - \frac{\Delta\Gamma}{2}\Gamma\sigma_\tau^2 + \frac{\Delta\Gamma}{2}\Sigma\sigma_\tau\right)} \tag{4.22}$$

4.2.3 Considerations

Summing up briefly the results from the foregoing paragraphs, we can notice how the proper time resolution affects the $A_{CP}^{exp}(\tau)$ measurements in both the flavour specific decay ($B_s \to D_s\pi$) and CP eigenstates (for example $B_s \to K^+K^-$ or $B_d \to \pi\pi$ decays).

The experimental effects of mistag fraction ω and B proper time resolution determine the equations 4.18 and 4.22. Both the equations contain a common dilution factor D which represents how much the oscillations amplitudes, and thus the observed *CP*, are reduced due to experimental effects.

$$D = e^{-\frac{\sigma_\tau^2 \Delta m^2}{2} - \frac{\sigma_\tau^2 \Delta\Gamma^2}{8}} \cdot (1-2\omega) \tag{4.23}$$

Also the proper time resolution put in new phases in the sin, sinh, cos, and cosh terms.

The damping factor expression is valid for the A_{CP} asymmetry of B_s and B_d. Given that LHCb will measure B proper time with a typical resolution of 40 fs, in case of the B_d, due to the small value for Δm_d, the factor $e^{-\frac{\sigma^2 \Delta m^2}{2}}$ is negligible. In case of the B_s system it amounts to ~ 0.8. Moreover $\Delta\Gamma_d$ and $\Delta\Gamma_s$ are small so the factor $e^{-\frac{\sigma^2 \Delta\Gamma^2}{8}}$ can be neglected.

In figure 4.1 is shown the σ_τ dependence of the damping factor in case of B_s. This picture can help understanding how the damping factor changes if the proper time resolution is distributed over a range. Up to now we have not advanced any hypothesis about the behavior of the proper time resolution σ_τ. In par. 3.1 we have shown that the resolution σ_τ can be measured by the proper time error that can be calculated event by event. Indeed depending on the event considered, the resolution can vary considerably. For example, from the $B_s \to D_s\pi$ decay, I pull the B meson proper time error out (fig.4.2) where it can be noticed that the values range from 10 and 60 fs. .

The time dependent analyses can take advantage of this additional observable to improve the parameters determination. In fact, this information can be used to re-weight the events according to the errors, in a similar way we calculate mean or weighted mean.

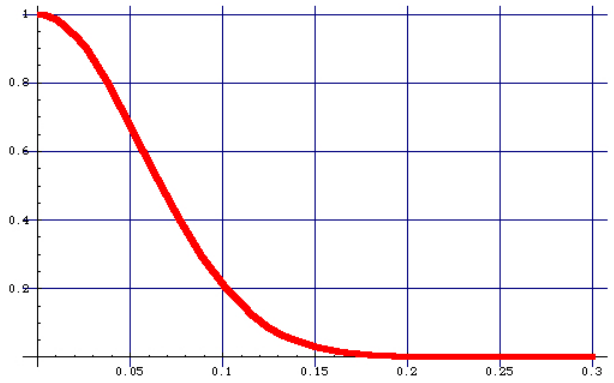

Figure 4.1: The damping factor $e^{-\frac{\sigma_\tau^2 \Delta m^2}{2}}$ as function of the proper time error σ. The time resolution can reduce significantly the A_{CP} amplitude. The present mean value for the proper time error in LHCb is estimated about ~ 40 fs and for this reason the damping factor is still quite close to 0.8. Otherwise an error value near ~ 100 fs will reduce outrageously the A_{CP} amplitude.

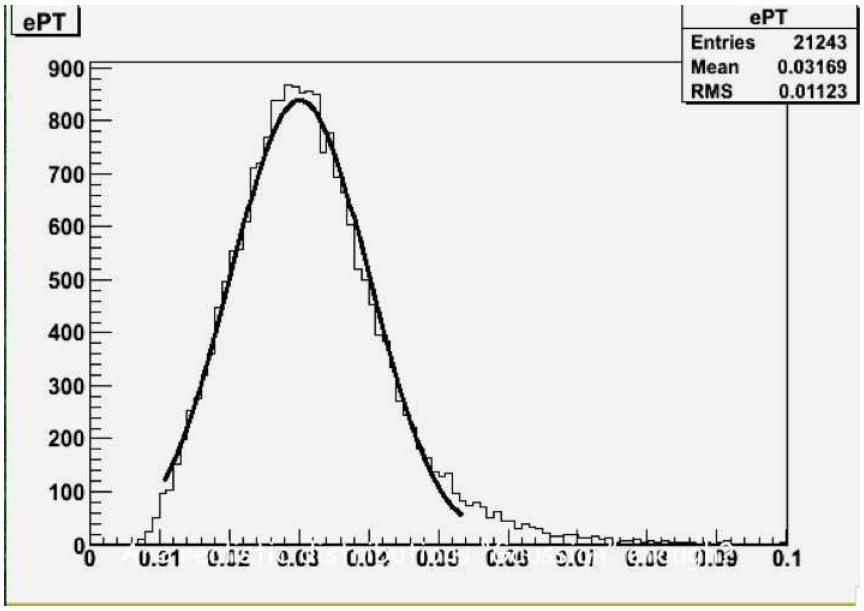

Figure 4.2: The picture represents the B proper time error distribution in the $B \to \pi\pi$ decay channel. It can be noticed that the values range from 10 and 60 fs.

4.3 RooFit studies: impact of B decay proper time measurement in time-dependent analyses

Up to now we have met the meaningful physical values CP asymmetries $A_{CP}(\tau)$, which are time dependent quantities. Moreover the equations 4.22, 4.18 show clearly how the proper time resolution can influence the measurements. LHCb will measure the B meson proper time with an excellent mean resolution of ~ 40 fs [15]. Nevertheless this error is a mean value of a distribution which can be calculated experimentally. In this section we study how this information can improve the fit results.

In order to evaluate the advantages of using the B meson proper time measurements in time dependent analyses, we have prepared a set of trials with the *RooFit* package [23]. *RooFit* allows to simulate entirely the life of the B mesons, paying attention to taggers, proper time resolution and statistics. With these studies we can also evaluate the limits on biases and on scaling factors in proper time measurements to achieve good physics results.

We studied in depth the usage of the event by event proper time error and also the utilization of a fixed resolution, understanding the incidental improvements in the physical measurements with these two different approaches.

The time resolution is a measurable value which can be correctly evaluated by error propagation (see par. 3.1) provided that the input measurements own normally distributed FITPull distributions. By applying the event by event proper time resolution could we improve the goodness of the physical parameters?

4.3.1 Signal and background, probability density functions *(*Pdf*)* definition

The package *RooFit* allows to study any B decay analysis by means of a Monte Carlo simulation. It allows to generate samples of signal and background events with realistic proportions, each one following a specific model that represents the data. The model is based on the physical decay process (time dependent rate) and it takes into account several experimental effects(resolutions, tag efficiency and acceptance).

The generated data can be analyzed by the same program, with a fit procedure, in order to retrieve all the useful information. The advantage of this approach is the possibility to study the analysis potentialities as a function of the input parameters.

The necessary model to generate or fit the data is based on a probability density function which depends on several observables. In the case of CP analysis the observables are

- the invariant mass m of the B candidate
- the flavour tag response tag
- the reconstructed B proper time τ and corresponding error σ_τ
- in case of flavour specific decays, the final state rec

The most general Pdf , for signal and background events, can be expressed by

$$Pdf(m, \tau, \sigma_\tau, tag, rec) = Pdf_{Signal}(m, \tau, \sigma_\tau, tag, rec) + Pdf_{Back}(m, \tau, \sigma_\tau, tag, rec)$$

The probability density function Pdf_{Signal} that describes the observed signal events, depends on the theoretical rate $\Gamma_{true}(t)$ (see equation 2.28, 2.29, 2.30, 2.31) and on the mass distribution: [4]

$$\mathrm{Pdf}_{\mathrm{Signal}}(m, \tau, \sigma_\tau, tag, rec) =$$

$$\epsilon(\tau) \int dt \, (\Gamma(t, tag, rec) \otimes \mathrm{Gauss}(t - \tau; \sigma_\tau)) \, \mathrm{Pdf}_{Signal}(\sigma_\tau) \mathrm{Pdf}_{Signal}(m) \quad (4.24)$$

where $\epsilon(\tau)$ is an effective function due to the detector efficiency. Its parametrization is studied on Monte Carlo data and it is given by:

$$\epsilon(\tau) = \frac{(\alpha t)^5}{1 + (\alpha t)^5}$$

The term $\mathrm{Gauss}(t - \tau; \sigma_\tau)$ represents the resolution model that transforms the true proper lifetime t into the observed one τ, given the resolution σ_τ.

For the $\mathrm{Pdf}_{Signal}(m)$ we consider a gaussian distribution centered at the B mass with resolution σ_m.

$$Pdf_{Signal}(m) = \frac{e^{-\frac{(m - m_B)^2}{2\sigma_m^2}}}{\sqrt{2\pi}\sigma_m}$$

If the σ_τ is an observable, $\mathrm{Pdf}(\sigma_\tau)$ represents the probability density function of the proper time error drawn from real data[5] . While, in case we assume a fixed value for proper time resolution, we have to omit completely the $\mathrm{Pdf}(\sigma_\tau)$.

$$\mathrm{Pdf}_{\mathrm{Signal}}(m, \tau, tag, rec) = \epsilon(\tau) \int dt \, (\Gamma_{true}(t, tag, rec) \otimes \mathrm{Gauss}(t - \tau; \sigma_\tau)) \, \mathrm{Pdf}_{Signal}(m)$$

and $\sigma_\tau$becomes a parameter.

Concerning the background, since the time and mass evolution has different origin, it is described by different functions:

[4] Inn case of $B_s \to D_s \pi$ we have tag 0=untagged, tag ± 1 = tagged and for the reconstructed channel (rec=1 $(K^+K^-\pi^+)\pi^-$ or rec=-1 $(K^+K^-\pi^-)\pi^+$)

[5] In this case we obtained the error distributions from Monte Carlo, as reported in fig. 4.2.

$$Pdf_{Back}(m, \tau, \sigma_\tau, tag, rec) = \Gamma_{Back}(\tau, tag, rec)\mathrm{Pdf}_{Back}(m)Pdf_{Back}(\sigma_\tau)$$

The $\Gamma_{Back}(\tau)$ is an effective function describing the proper time dependence of the background rate. Its functional form can be extracted from data by studying the proper time distribution in the side bands mass spectrum. In our studies we consider the following form for every *tag* and *rec* combinations:

$$\Gamma_{Back}(\tau) = \eta(\tau) \cdot e^{-\alpha_{Back}\tau} \tag{4.25}$$

while the mass distribution assume the form:

$$Pdf_{Back}(m) = e^{-\beta_{Back}m} \tag{4.26}$$

Similarly to the signal case, the $Pdf_{Back}(\sigma_\tau)$ represents the probability density function of the time error that can be extracted by the side bands mass distribution.

As shown the Pdf depends on several parameters (physical or experimental quantities) that they can be freed during the fit optimization.

4.3.2 Proper time error distribution vs fixed value

In this section we want to give a direct estimate of how much the time dependent analyses can benefit by using the proper time error as an observable respect the case in which a fixed resolution is assumed. We start considering the simplified case of a pure signal time dependent amplitude like:

$$\Gamma(\tau; \Delta m_B, \Gamma_B, A) = e^{-\Gamma_B \tau} \cdot \big(1. + A \cdot \cos(\Delta m_B \cdot \tau)\big) \tag{4.27}$$

where $\Delta m_B, \Gamma_B$ are the B mass difference and decay width and A is the amplitude.
With the `RooFit` package we generate 50.000 events according the Pdf distribution 4.24 (for the moment we assume the acceptance function is $\epsilon(\tau) = 1$, with the input parameters $\Gamma_B = 1/1.5$, $\Delta m_B = 17.8\,\mathrm{ps}^{-1}$, $A = 1$ and different proper time resolutions) defining a sample of τ^i and σ_τ^i measurements. `RooFit` exploits, for the data generation, a library function that implements the equations 4.2, 4.3, 4.4, 4.5, by including also the gaussian resolution model chosen.

To make the comparison, we fit the data generated according two different approaches:

1. two observables (τ^i and σ_τ^i) and the Pdf depending on τ and σ_τ ;
2. we neglect the information on σ_τ^i and fit with a time dependent *Pdf* with a fixed resolution value given by the mean value of the proper time error.

	input values		Fit time and error		Fit time	
Fit parameters	μ_{σ_τ} (fs)	σ_{σ_τ} (fs)	A	B/S	A	B/S
			Signal data sample			
Gauss narrow	40	8	1.001 ± 0.007		1.002 ± 0.007	
Gauss wide	100	25	1.01 ± 0.02		1.15 ± 0.03	
Landau narrow	40	8	1.002 ± 0.007		1.002 ± 0.009	
Landau wide	100	25	0.99 ± 0.02		1.69 ± 0.09	
			Signal + Background data sample			
Gauss	40	8	1.00 ± 0.01	0.25	1.09 ± 0.01	0.37
	60	10				
Landau	40	8	1.01 ± 0.01	0.28	1.07 ± 0.01	0.25
	60	10				

Table 4.1: The generation parameters of the $Pdf(\sigma_\tau)$ are reported in the first column. In case of gaussian(Landau) generation, they represent the mean(maximum) and sigma of the distribution. The first four rows gather the fit output in case of pure signal, whereas the last lines refer to the signal and background case. The comparison indicates the improvement obtained considering the time dependent analysis with (second column) and without (last column) the event by event resolution description. In case of signal+background data sample both $Pdf_{Signal/Back}(\sigma_\tau)$ parameters are quoted.

The comparison will indicate the improvement obtained considering the error in the time dependent analysis. This comparison is made in four cases corresponding to different $Pdf(\sigma_\tau)$ (gaussian or Landau) and parameters. The fit results are represented in figure 4.3, and the corresponding values are reported in table 4.1. In case of good resolutions ($\bar{\sigma}_\tau = 40$ fs) there is not too much improvement in fitting with time and error per event: the two fit strategies give similar values and errors for amplitude in agreement to the input value $A = 1$. Otherwise, in case of "unprecise" measurements ($\bar{\sigma}_\tau = 100$ fs), by fixing the resolution to the mean error leads to an incorrect amplitude value.
The same behavior is present in case we consider a Landau error distribution.
Within the limits of this speculations, we can say that in case of "precise" resolution, the linearity of the problem and the limit central theorem allows to simplify the time dependent analysis by considering the mean error.
Of course the conclusions may change dramatically if background is considered. In fact if the error time distribution of the background differs from the signal one, the analysis of τ and σ_τ observables gives better results. This fact is shown in fig. 4.4. In these cases the data are generated with a fraction $B/S = 0.25$ of background events whose time error distributions are given by a Gaussian ($\mu_{\sigma_\tau} = 60$fs, $\mu_{\sigma_\tau} = 10$fs, top plots) or a Landau ($\max_{\sigma_\tau} = 60$fs, $\mu_{\sigma_{tau}} = 10$fs, bottom plots). The corresponding fit parameters are compared in table 4.1.

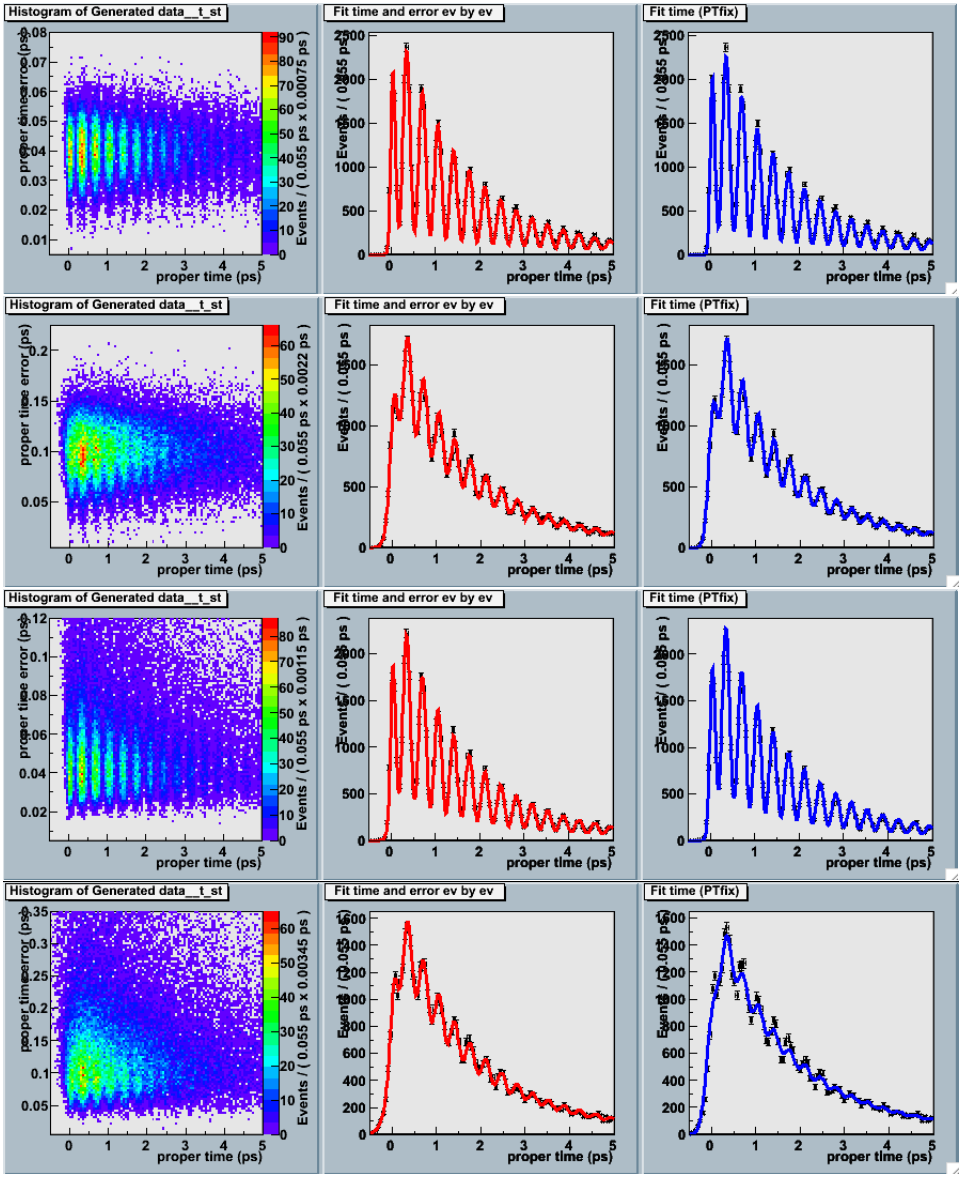

Figure 4.3: Comparison between the fit results of 50.000 events generated according to the amplitude 4.24, a gaussian time resolution model and different proper time error distributions. The second column represent the fit using time and error(event by event) , while the third column shows the fit results employing only the time observable. From top to bottom: a narrow gaussian, a wide gaussian, a narrow landau and a wide landau distributions.

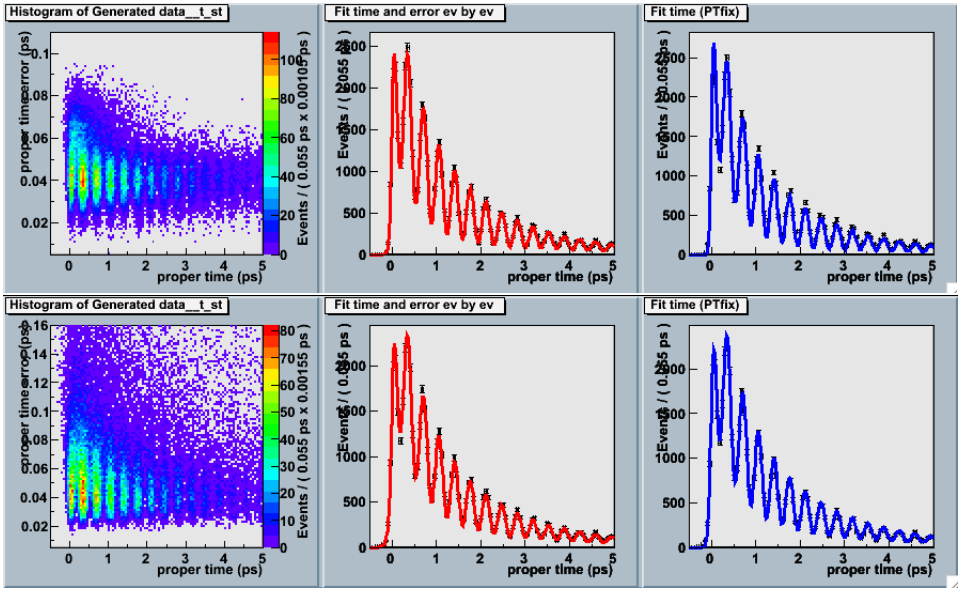

Figure 4.4: Comparison between the results of a fit of time and error per event (second column) and only time (third column) of 50.000 events with $B/S = 0.25$, a gaussian time resolution model and different proper time error distributions: top, a narrow gaussian; bottom a narrow Landau distributions.

4.4 Examples

In this section we give a description of two time dependent analyses that LHCb will perform giving emphasis to the proper time measurements.

4.4.1 Δm_s measurement: the channel $B_s(\bar{B}_s) \to D_s^{\mp}(K^+K^-\pi^{\pm})\pi^{\mp}$.

This channel is a self-tagged process, since the charge of the pion in D_s decay defines uniquely the flavour of the B particle. For this reason this channel will be used to determine not only the mixing frequency Δm_s of $\bar{B}_s^0/B_s^0$, but also the wrong tag fraction ω_{tag}. The sample of untagged events can also be useful to determine the with difference $\Delta\Gamma_s$.

The theoretical amplitude of the decay process are reported in eq. 4.6, 4.7, 4.8, 4.9 where the first two (second two) equations have the same amplitudes and correspond to the unmixed (mixed) decay amplitudes. For the untagged events (tag=0), depending on the reconstructed channel (rec=1 $(K^+K^-\pi^+)\pi^-$ or rec=-1 $(K^+K^-\pi^-)\pi^+$), the observed amplitudes are reported in equations 4.10 and 4.11 . These amplitudes are the bases for the signal Pdf, whereas for the background we follow the indications given in the par.4.3.1.

LHCb will be able to collect about 110.000 $B_s \to D_s\pi$ signal events in one year of data taking (2fb^{-1}) with an estimated background contamination of $B/S = 0.83(\pm 0.09)$ and a tagging performances of $\epsilon_{tag} = (60.22 \pm 0.18)\%$ and $\omega_{tag} = (30.26 \pm 0.23)\%$. As already mentioned, besides the measurement of Δm_s the analysis of this channel will provide an experimental determination of the ω_{tag}, provided that the proper time resolution is known. In fact in eq. 4.23 we have shown that the effects of proper time resolution and wrong tag are indistinguishable since they are factorized. Nevertheless if the proper time error is distributed over a sufficiently large range independently from the tagging performances, the analysis of time and proper time error will allow to disentangle the two contributions. Of course in this case it is extremely important that proper time error is well calibrated, for example by means of the FITPull method.

4.4.1.1 Proper time resolution dependence of Δm_s and ω_{tag} measurements

In this section we study how the measurements of Δm_s and ω_{tag} depend on the proper time resolution. Exploiting the *RooFit* capabilities, we generate several data samples corresponding to one year of data taking at LHCb. Each sample corresponds to different values of the parameters that define the proper time error distribution for the signal and the background events (quoted in tab. 4.2). Two different fits are performed:

1. Pdf_1- fit to all observables $(m, tag, rec, \tau, \sigma_\tau)$: in this case the proper time error calculated event by event is included and has a different distribution

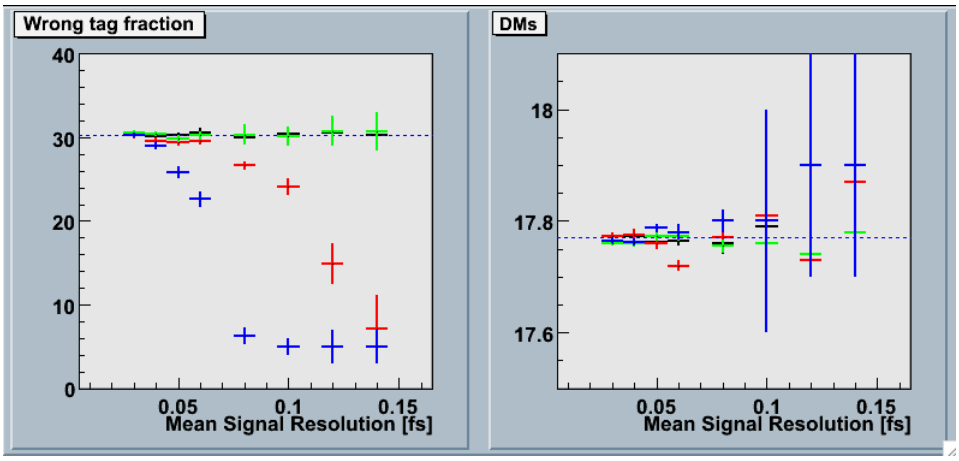

Figure 4.5: Graphical representation of the fit output for the ω_{tag} and Δm_s as a function of the input mean proper time resolution. Black (green) corresponds to Pdf_1 fits to data generated with a σ_τ gaussian(Landau) distribution. Red (blue) corresponds to Pdf_2 fits to data generated with a σ_τ gaussian(Landau) distribution. The dashed blue line represents the input generation value.

for signal or background events;

2. Pdf$_2$- fit to the (m, tag, rec, τ) observables: in this case we neglect the proper time error σ_{err} and we assume a fixed resolution value for all the events, which is extracted from the data.

In table 4.2 are reported the values of Δm_s and ω_{tag} found with the two fit approaches: independently on the $Pdf(\sigma_\tau)$, the fit approach using Pdf_1 finds the ω_{tag} and Δm_s values in agreement with the input ones($\omega_{tag} = 30.3\%$ and $\Delta m_s = 17.77\, ps^{-1}$). The approach based on Pdf_2 finds the right ω_{tag} value only for small resolution values ($\mu_{\sigma_\tau} < 60$ fs), while it fails for worse resolutions. Concerning the Δm_s the values found are in agreement with the input.

4.4.1.2 BIAS dependence of Δm_s and ω_{tag} measurements

In this section we study the dependence on the proper time bias of the Δm_s and ω_{tag} parameters. We generate several data samples with a resolution model modified by the following equation

$$G(t - \tau + b\sigma_\tau; \sigma_\tau) = \frac{e^{-\frac{(t-\tau+b\sigma_\tau)^2}{2\sigma_\tau^2}}}{\sqrt{2\pi}\sigma_\tau}$$

In table 4.3 and figure 4.6 are reported the fitter results . The bias affects both Δm_s and ω_{tag} , in particular Δm_s measurements show a strong linear

signal		background		Fit time and error		Fit time (Fixed Resolution)	
μ_{σ^τ} (fs)	σ_{σ^τ} (fs)	μ_{σ^τ} (fs)	σ_{σ^τ} (fs)	ω_{tag} %	Δm_s $(ps)^{-1}$	ω_{tag} %	Δm_s $(ps)^{-1}$
Gaussian distribution							
30	6	45	7.5	30.5 ± 0.2	17.774 ± 0.005	30.3 ± 0.5	17.774 ± 0.005
40	8	60	10	30.1 ± 0.2	17.773 ± 0.005	29.5 ± 0.5	17.776 ± 0.01
50	10	75	12.5	30.2 ± 0.4	17.762 ± 0.006	29.4 ± 0.5	17.76 ± 0.01
60	12	90	15	30.6 ± 0.5	17.765 ± 0.009	29.5 ± 0.4	17.72 ± 0.01
80	16	120	20	30.0 ± 0.5	17.76 ± 0.02	26.6 ± 0.5	17.77 ± 0.01
100	20	150	25	30.4 ± 0.6	17.79 ± 0.02	24.1 ± 1.0	17.81 ± 0.02
120	24	180	30	30.6 ± 1.0	17.73 ± 0.02	14.9 ± 2.5	17.73 ± 0.03
140	28	210	35	30.3 ± 1.5	17.78 ± 0.03	7.1 ± 4.0	17.87 ± 0.05
Landau distribution							
30	6	45	7.5	30.6 ± 0.2	17.761 ± 0.005	30.2 ± 0.3	17.765 ± 0.006
40	8	60	10	30.4 ± 0.3	17.760 ± 0.006	29.0 ± 0.4	17.762 ± 0.007
50	10	75	12.5	29.8 ± 0.4	17.772 ± 0.007	25.8 ± 0.7	17.787 ± 0.008
60	12	90	15	30.2 ± 0.5	17.772 ± 0.008	22.6 ± 0.9	17.780 ± 0.014
80	16	120	20	30.3 ± 1.2	17.755 ± 0.012	6.3 ± 1.0	17.80 ± 0.02
100	20	150	25	30.1 ± 1.2	17.760 ± 0.02	$5.0 * \pm 1.0$	17.80 ± 0.2
120	24	180	30	30.7 ± 1.8	17.74 ± 0.03	$5.0 * \pm 2.0$	17.9 ± 0.2
140	28	210	35	30.7 ± 2.3	17.78 ± 0.04	$5.0 * \pm 2.0$	17.9 ± 0.2

Table 4.2: Fit parameters ω_{tag} and Δm_s obtained by a fit to generated data with (Fit time and error columns) or without (Fit time columns) considering proper time error event by event in the Pdf . The input parameters used to generate $Pdf(\sigma_\tau$ according to a Gaussian or a Landau distribution are also quoted. μ_{σ_τ} represent the mean (max probability in case of the Landau) and σ_τ the sigma of the distribution.

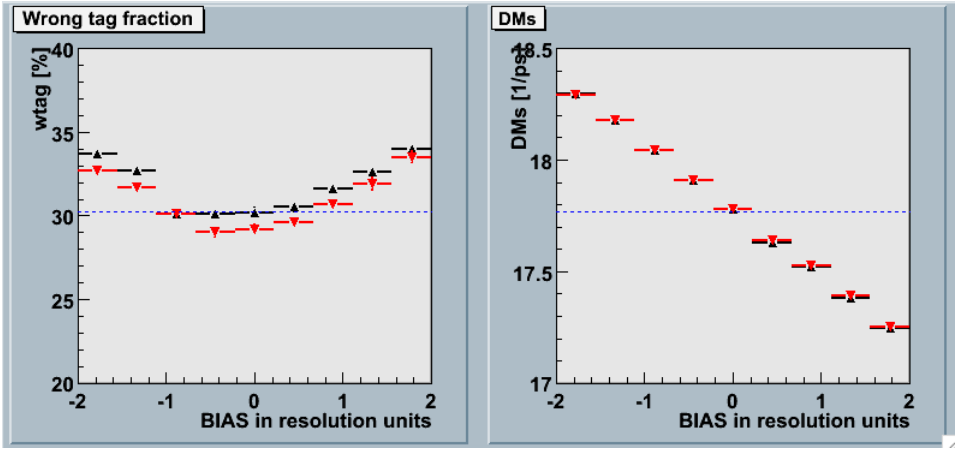

Figure 4.6: Graphical representation of the fit output for the ω_{tag} and Δm_s as a function of the input bias to the proper time. Black (green) corresponds to Pdf_1 fits to data generated with a σ_τ gaussian(Landau) distribution. Red (blue) corresponds to Pdf_2 fits to data generated with a σ_τ gaussian(Landau) distribution. The dashed blue line represents the input generation value.

dependence on the bias. This fact demonstrates the importance of a good proper time calibration for a correct and precise measurements.

4.4.1.3 Scaling Factor dependence of Δm_s and ω_{tag} measurements

In this section we study the effect of a scale factor to the proper time error on the Δm_s and ω_{tag} parameters. This fact allows us to simulate the cases where the errors are over/under estimated. We generate several data samples with a resolution model modified by the following equation

$$G(t-\tau;\sigma_\tau \times SF\,) = \frac{e^{-\frac{(t-\tau)^2}{2(\sigma_\tau \times SF)^2}}}{\sqrt{2\pi}\,(\sigma_\tau \times SF)}$$

and the $Pdf\ (\sigma_\tau)$ that does not include the scale factor SF. In table 4.4 and figure 4.7 are reported the fitter results. As expected, ω_{tag} strongly depends on SF, while $\Delta m_s$is independent. This fact demonstrates the importance of a good proper time error calibration for correct ω_{tag} measurement.

4.4.2 A CP asymmetry measurement: the channel $B_{d/s} \to h^+h^-$

As seen in the second chapter, provided that the hypothesis of the U spin symmetry is valid, the physical interpretation of the analyses of the decay channels

	signal		background		Fit time and error		Fit time (Fixed Resolution)	
BIAS	μ_{σ_τ} (fs)	σ_{σ_τ} (fs)	μ_{σ_τ} (fs)	σ_{σ_τ} (fs)	ω_{tag} %	Δm_s $(ps)^{-1}$	ω_{tag} %	Δm_s $(ps)^{-1}$
	Gaussian distribution							
-2.0	40	8	60	10	33.7 ± 0.3	18.295 ± 0.008	32.7 ± 0.3	18.290 ± 0.008
-1.5	40	8	60	10	32.7 ± 0.3	18.177 ± 0.008	31.7 ± 0.3	18.177 ± 0.007
-1.0	40	8	60	10	30.1 ± 0.3	18.045 ± 0.007	30.1 ± 0.3	18.041 ± 0.006
-0.5	40	8	60	10	30.1 ± 0.3	17.908 ± 0.007	29.0 ± 0.3	17.909 ± 0.005
0.0	40	8	60	10	30.2 ± 0.3	17.779 ± 0.007	29.2 ± 0.3	17.780 ± 0.007
0.5	40	8	60	10	30.5 ± 0.3	17.626 ± 0.007	29.6 ± 0.3	17.638 ± 0.005
1.0	40	8	60	10	31.6 ± 0.3	17.520 ± 0.007	30.7 ± 0.3	17.525 ± 0.006
1.5	40	8	60	10	32.6 ± 0.3	17.380 ± 0.008	31.9 ± 0.4	17.390 ± 0.008
2.0	40	8	60	10	34.0 ± 0.3	17.244 ± 0.008	33.5 ± 0.4	17.251 ± 0.007

Table 4.3: Fit parameters in case of BIAS to the proper time measurement (expressed in sigma units) for the $B_s \rightarrow D_s\pi$ channel. Input bias and resolution parameters are listed together with the fit outputs Δm_s and ω_{tag}.

	signal		background		Fit time and error		Fit time (Fixed Resolution)	
SF	μ_{σ_τ} (fs)	σ_{σ_τ} (fs)	μ_{σ_τ} (fs)	σ_{σ_τ} (fs)	ω_{tag} %	Δm_s $(ps)^{-1}$	ω_{tag} %	Δm_s $(ps)^{-1}$
	Gaussian distribution							
0.5	40	8	60	10	26.8 ± 0.2	17.779 ± 0.004	25.8 ± 0.2	17.781 ± 0.006
0.6	40	8	60	10	27.5 ± 0.2	17.777 ± 0.004	26.6 ± 0.2	17.778 ± 0.006
0.7	40	8	60	10	27.9 ± 0.2	17.776 ± 0.005	27.1 ± 0.2	17.777 ± 0.006
0.8	40	8	60	10	28.3 ± 0.2	17.765 ± 0.005	27.4 ± 0.2	17.765 ± 0.006
0.9	40	8	60	10	29.4 ± 0.2	17.770 ± 0.006	28.8 ± 0.2	17.771 ± 0.007
1.0	40	8	60	10	30.1 ± 0.2	17.773 ± 0.007	29.5 ± 0.2	17.776 ± 0.007
1.1	40	8	60	10	31.2 ± 0.2	17.767 ± 0.007	30.7 ± 0.2	17.766 ± 0.007
1.2	40	8	60	10	32.6 ± 0.2	17.761 ± 0.008	32.2 ± 0.2	17.762 ± 0.007
1.3	40	8	60	10	33.4 ± 0.2	17.769 ± 0.008	33.1 ± 0.2	17.770 ± 0.008
1.4	40	8	60	10	34.4 ± 0.2	17.765 ± 0.009	34.2 ± 0.2	17.763 ± 0.008
1.5	40	8	60	10	35.2 ± 0.2	17.757 ± 0.009	35.2 ± 0.2	17.754 ± 0.009
1.6	40	8	60	10	36.4 ± 0.2	17.754 ± 0.010	36.3 ± 0.2	17.757 ± 0.009
1.7	40	8	60	10	37.1 ± 0.2	17.766 ± 0.010	37.2 ± 0.2	17.767 ± 0.010
1.8	40	8	60	10	38.2 ± 0.2	17.765 ± 0.010	38.3 ± 0.2	17.768 ± 0.010
1.9	40	8	60	10	39.1 ± 0.2	17.761 ± 0.010	39.4 ± 0.2	17.761 ± 0.010
2.0	40	8	60	10	40.3 ± 0.2	17.742 ± 0.011	40.5 ± 0.2	17.745 ± 0.011

Table 4.4: Fit parameters in case of a SF of the proper time error measurement (expressed in sigma units) for the $B_s \to D_s\pi$ channel. Input bias and resolution parameters are listed together with the fit outputs Δm_s and ω_{tag}.

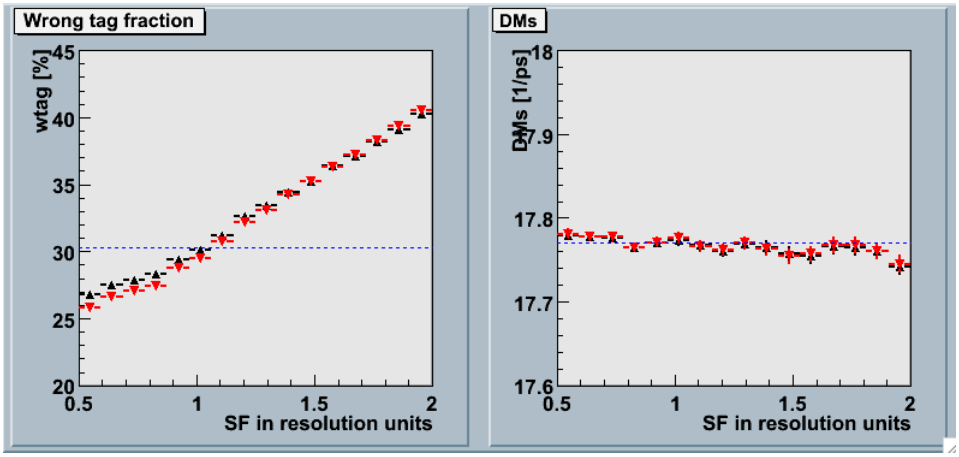

Figure 4.7: Graphical representation of the fit output for the ω_{tag} and Δm_s as a function of the input scaling factor SF of the proper time. Black corresponds to Pdf_1 fits to data generated with a σ_τ gaussian(Landau) distribution. Red corresponds to Pdf_2 fits to data generated with a σ_τ gaussian(Landau) distribution.

$B_d \to \pi^+\pi^-$ and $B_s \to K^+K^-$, allows an independent measurement of the γ angle.

LHCb put the simultaneous analyses of the $B_{d/s} \to h^+h^-$ channels forward, in guise to earn in a single step all the CP parameters involved. This approach shows the advantage in evaluating, with the most suitable way, the signals $B_{d/s} \to K\pi$ e $B_d \to \pi\pi$, that, due to the incidental particles mis-identification, can contribute to the overall background. For a detailed description see reference (A.Sarti B2hh note in preparation).

In the next subsection we will limit the discussion of the proper time error incidence on the A_{CP}^{dir} and A_{CP}^{mix} parameters and in presence of biases or scaling factors as well.

The physical relevant parameters to determine from these channels are the CP asymmetries A_{CP}^{mix} in the mixing , A_{CP}^{dir} in the decay and the charge asymmetry $A_{K\pi}$ of $B_{d/s} \to \pi K$ respect to $\bar{B}_{d/s} \to \pi K$ decays (the parameter Δm_s is supposed fixed by the dedicated measurement described above). The experimental asymmetries depend also on the tagging power ω_{tag} and on the proper time resolution.

Some useful considerations can be made:

1. as already mentioned the dilution effects given by proper time resolution are more important for the fast oscillating B_s channels, while they can be neglected in case of B_d channels.

2. all the $B_{d/s} \to h^+h^-$ channels share the same decay topology and trigger.

For this reason, in the limit of the opposite side tagging, we can assume that the ω_{tag} is the same in all the channels. The same side tagging, on the other side is different for B_s and B_d decays.

3. The $B_{d/s} \to K\pi$ are self-tagging decays, so their oscillation amplitude depends only on the ω_{tag} and the proper time resolution.

These features can help us defining the fit strategy. A separated fit of B_d decays assuming a fixed resolution model will measure A_{CP}^{mix} , A_{CP}^{dir} and $A_{K\pi}$ in the B_d sector. The control channels $B_d \to K\pi$ also provide a direct measurement of the ω_{tag} value. If this is done on the events selected by opposite side tagging, the fit result on ω_{tag} can be used to fit the B_s channels. In this case proper time resolution play an important rule, so a per event resolution model is recommended. In this case the control channels $B_s \to K\pi$ can be useful to find any possible adjustments to the experimental proper time resolution, in particular any Scale Factors.

Given this analysis framework I will discuss the analysis of the only $B_s$channels given that we are considering the only opposite tagged events, the ω_{tag} is known from a fit to the $B_d \to h^+h^-$ channels and Δm_s is measured.

Studies on DC04 Monte-Carlo have allowed to give an estimate of the event yield, the background contamination B/S and the tagging performances of the channels. In table are reported the values corresponding to one year of data taking.

4.4.2.1 Proper time resolution dependence of A_{CP}^{dir} and A_{CP}^{mix} measurements

In this section we want to study the precision of the physical parameters A_{CP}^{mix} and A_{CP}^{dir} as a function of the proper time resolution and fit strategy. As par.4.4.1.1 we consider the two fit strategies based on Pdf_1 and Pdf_2.

In table 4.6 are reported the values of A_{CP}^{mix} and A_{CP}^{dir} found with the two fit approaches: independently on the $Pdf(\sigma_\tau)$, and the fit approach, the fitted values are in agreement with the input ones($A_{CP}^{mix} = 0.347$ and $A_{CP}^{dir} = -0.123$). We can notice that the precision of these parameters worsens for decreasing resolution values.

4.4.2.2 BIAS dependence of A_{CP}^{dir} and A_{CP}^{mix} measurements

In this section we study the dependence on the proper time bias of theA_{CP}^{dir} and A_{CP}^{mix}parameters. We generate several data samples in the same way as reported in par.4.4.1.2.

In table 4.7 and figure 4.9 are reported the fitter results . A_{CP}^{dir} measurement shows a significant dependence on the bias, while the A_{CP}^{mix} does not exhibit a clear one. Anyways both fits approaches give similar results.

Channel	Branching ratio (10^{-6})	event yield $L = 2fb^{-1}$	B/S (specific)	B/S ($\bar{b}b$ inclusive)	w_{tag} (opposite side)
$B_s^0 \to \pi^+ K^-$	4.8	9800	1.92	0.54	$32.8 \pm 0.3\%$
$B_s^0 \to K^+ K^-$	18.5	35900	< 0.06	0.08	$32.8 \pm 0.3\%$

Table 4.5: Untagged annual yield and background-to-signal ratio from specific and $b\bar{b}$-inclusive background for the decays $B_s \to h^+ h^-$. The B/S values are computed without applying the trigger in order to increase the effective statistics.

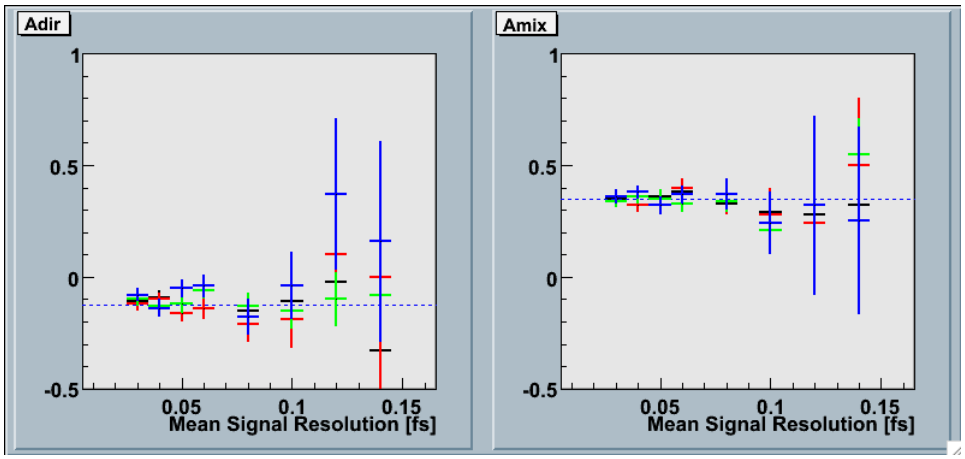

Figure 4.8: Graphical representation of the fit output for the A_{CP}^{dir} and A_{CP}^{mix} as a function of the input mean proper time resolution. Black (green) corresponds to Pdf_1 fits to data generated with a σ_τ gaussian(Landau) distribution. Red (blue) corresponds to Pdf_2 fits to data generated with a σ_τ gaussian(Landau) distribution.

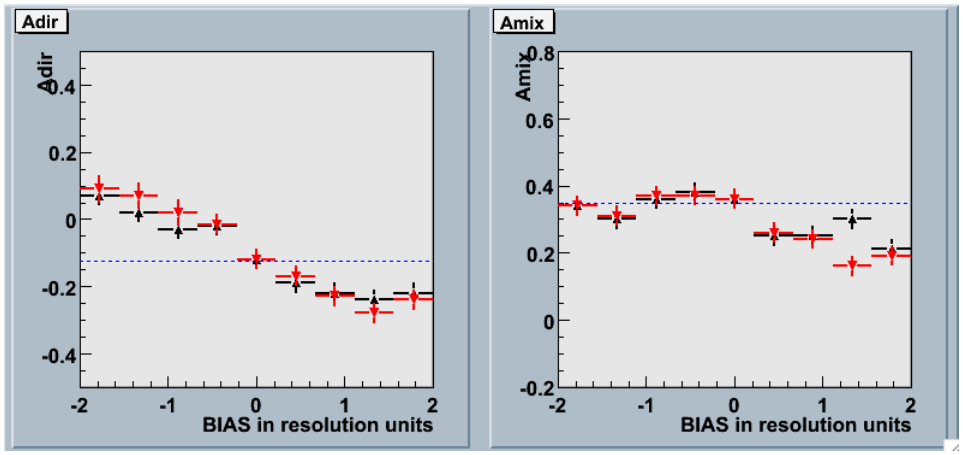

Figure 4.9: Graphical representation of the fit output for the A_{CP}^{dir} and A_{CP}^{mix} as a function of the input bias to the proper time. Black (green) corresponds to Pdf_1 fits to data generated with a σ_τ gaussian(Landau) distribution. Red (blue) corresponds to Pdf_2 fits to data generated with a σ_τ gaussian(Landau) distribution. The dashed blue line represents the input generation value.

signal		background		Fit time and error		Fit time (Fixed Resolution)	
μ_{σ^τ} (fs)	σ_{σ^τ} (fs)	μ_{σ^τ} (fs)	σ_{σ^τ} (fs)	A_{CP}^{dir}	A_{CP}^{dir}	A_{CP}^{dir}	A_{CP}^{dir}
Gaussian distribution							
30	6	45	7.5	-0.11 ± 0.03	0.35 ± 0.03	-0.12 ± 0.03	0.34 ± 0.03
40	8	60	10	-0.09 ± 0.03	0.32 ± 0.03	-0.10 ± 0.03	0.32 ± 0.03
50	10	75	12.5	-0.16 ± 0.04	0.36 ± 0.03	-0.16 ± 0.04	0.35 ± 0.03
60	12	90	15	-0.14 ± 0.04	0.38 ± 0.04	-0.14 ± 0.05	0.40 ± 0.04
80	16	120	20	-0.15 ± 0.06	0.33 ± 0.05	-0.21 ± 0.08	0.34 ± 0.06
100	20	150	25	-0.11 ± 0.09	0.29 ± 0.08	-0.19 ± 0.13	0.28 ± 0.12
120	24	180	30	-0.02 ± 0.13	0.28 ± 0.11	0.10 ± 0.19	0.24 ± 0.19
140	28	210	35	-0.33 ± 0.20	0.32 ± 0.20	0.0 ± 0.5	0.5 ± 0.3
Landau distribution							
30	6	45	7.5	-0.10 ± 0.03	0.34 ± 0.03	-0.08 ± 0.03	0.36 ± 0.03
40	8	60	10	-0.13 ± 0.03	0.36 ± 0.03	-0.14 ± 0.04	0.38 ± 0.03
50	10	75	12.5	-0.12 ± 0.04	0.35 ± 0.04	-0.05 ± 0.04	0.32 ± 0.04
60	12	90	15	-0.06 ± 0.04	0.33 ± 0.04	-0.04 ± 0.05	0.37 ± 0.04
80	16	120	20	-0.13 ± 0.06	0.34 ± 0.05	-0.18 ± 0.08	0.37 ± 0.07
100	20	150	25	-0.15 ± 0.08	0.21 ± 0.08	-0.04 ± 0.15	0.24 ± 0.14
120	24	180	30	-0.10 ± 0.12	0.23 ± 0.12	0.37 ± 0.34	0.32 ± 0.37
140	28	210	35	-0.08 ± 0.21	0.55 ± 0.16	0.16 ± 0.45	0.25 ± 0.42

Table 4.6: Values of A_{CP}^{dir} and A_{CP}^{dir} obtained by a fit with a per event proper time resolution (Fit time and error columns) or with a fixed resolution (Fit time), to several data samples generated with different resolution distributions and parameters. All the generated samples have input values: $A_{CP}^{dir} = -0.123$ and $A_{CP}^{mix} = 0.347$

	signal		background		Fit time and error		Fit time (Fixed Resolution)	
BIAS	μ_{σ^τ} (fs)	σ_{σ^τ} (fs)	μ_{σ^τ} (fs)	σ_{σ^τ} (fs)	A_{CP}^{dir}	A_{CP}^{mix}	A_{CP}^{dir}	A_{CP}^{mix}
	Gaussian distribution							
-2.0	40	8	60	10	0.07 ± 0.03	0.34 ± 0.03	0.09 ± 0.04	0.34 ± 0.03
-1.5	40	8	60	10	0.02 ± 0.03	0.30 ± 0.03	0.07 ± 0.04	0.31 ± 0.03
-1.0	40	8	60	10	-0.02 ± 0.03	0.36 ± 0.03	0.02 ± 0.04	0.37 ± 0.03
-0.5	40	8	60	10	-0.02 ± 0.03	0.38 ± 0.03	-0.015 ± 0.030	0.37 ± 0.03
0.0	40	8	60	10	-0.12 ± 0.03	0.36 ± 0.03	-0.12 ± 0.03	0.36 ± 0.03
0.5	40	8	60	10	-0.19 ± 0.03	0.25 ± 0.03	-0.17 ± 0.03	0.26 ± 0.03
1.0	40	8	60	10	-0.22 ± 0.03	0.25 ± 0.03	-0.23 ± 0.03	0.24 ± 0.03
1.5	40	8	60	10	-0.24 ± 0.03	0.20 ± 0.03	-0.28 ± 0.03	0.16 ± 0.03
2.0	40	8	60	10	-0.22 ± 0.03	0.21 ± 0.03	-0.24 ± 0.03	0.19 ± 0.03

Table 4.7: Fit parameters in case of BIAS to the proper time measurement (expressed in sigma units) for the $B_s \to hh$ channel. Input bias and resolution parameters are listed together with the fit outputs A_{CP}^{dir} and A_{CP}^{mix}.

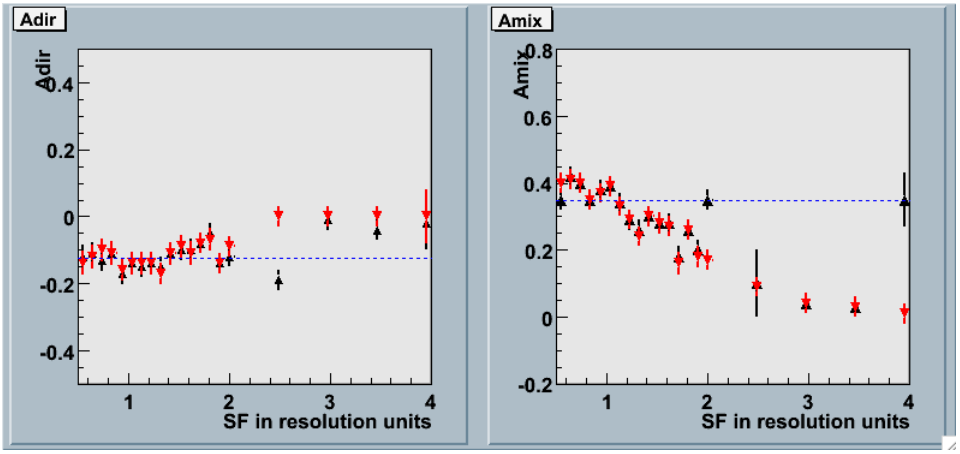

Figure 4.10: Graphical representation of the fit output for the A_{CP}^{dir} and A_{CP}^{mix} as a function of the input scaling factor SF of the proper time. Black corresponds to Pdf_1 fits to data generated with a σ_τ gaussian(Landau) distribution. Red corresponds to Pdf_2 fits to data generated with a σ_τ gaussian(Landau) distribution.

4.4.2.3 Scaling Factor dependence of A_{CP}^{dir} and A_{CP}^{mix} measurements

In this section we study the effect of a scale factor to the proper time error on the A_{CP}^{dir} and A_{CP}^{mix} parameters. This fact allows us to simulate the cases where the errors are over/under estimated. We generate several data samples with a resolution model modified as described in par. 4.4.1.3.

In table 4.8 and figure 4.10 are reported the fitter results. A_{CP}^{dir} seems to be only slightly affected by scaling factor for $SF < 2$, while for bigger scaling factors the fitted values are incompatible with the generated one. Concerning the A_{CP}^{mix} parameter, the dependence is more evident. Both fits approaches, anyways, give similar results.

	signal		background		Fit time and error		Fit time (Fixed Resolution)	
SF	μ_{σ^τ} (fs)	σ_{σ^τ} (fs)	μ_{σ^τ} (fs)	σ_{σ^τ} (fs)	A_{CP}^{dir}	A_{CP}^{mix}	A_{CP}^{dir}	A_{CP}^{mix}
	Gaussian distribution							
0.5	40	8	60	10	-0.12 ± 0.03	0.35 ± 0.03	-0.14 ± 0.04	0.40 ± 0.03
0.6	40	8	60	10	-0.11 ± 0.03	0.42 ± 0.03	-0.12 ± 0.04	0.41 ± 0.03
0.7	40	8	60	10	-0.13 ± 0.03	0.40 ± 0.03	-0.10 ± 0.04	0.40 ± 0.03
0.8	40	8	60	10	-0.11 ± 0.03	0.35 ± 0.03	-0.11 ± 0.04	0.35 ± 0.03
0.9	40	8	60	10	-0.17 ± 0.03	0.38 ± 0.03	-0.16 ± 0.04	0.37 ± 0.03
1.0	40	8	60	10	-0.14 ± 0.03	0.39 ± 0.03	-0.14 ± 0.04	0.39 ± 0.03
1.1	40	8	60	10	-0.15 ± 0.03	0.34 ± 0.03	-0.14 ± 0.03	0.33 ± 0.03
1.2	40	8	60	10	-0.14 ± 0.03	0.29 ± 0.03	-0.14 ± 0.03	0.29 ± 0.03
1.3	40	8	60	10	-0.15 ± 0.03	0.26 ± 0.03	-0.17 ± 0.03	0.24 ± 0.03
1.4	40	8	60	10	-0.11 ± 0.03	0.30 ± 0.03	-0.11 ± 0.03	0.30 ± 0.03
1.5	40	8	60	10	-0.10 ± 0.03	0.28 ± 0.03	-0.09 ± 0.03	0.28 ± 0.03
1.6	40	8	60	10	-0.10 ± 0.03	0.28 ± 0.03	-0.11 ± 0.04	0.27 ± 0.03
1.7	40	8	60	10	-0.08 ± 0.03	0.18 ± 0.03	-0.08 ± 0.03	0.16 ± 0.03
1.8	40	8	60	10	-0.05 ± 0.03	0.26 ± 0.03	-0.07 ± 0.03	0.26 ± 0.03
1.9	40	8	60	10	-0.14 ± 0.03	0.20 ± 0.03	-0.14 ± 0.03	0.18 ± 0.03
2.0	40	8	60	10	-0.12 ± 0.03	0.35 ± 0.03	-0.09 ± 0.03	0.17 ± 0.03
2.5	40	8	60	10	-0.19 ± 0.03	0.10 ± 0.03	0.00 ± 0.03	0.09 ± 0.03
3.0	40	8	60	10	-0.00 ± 0.03	0.04 ± 0.03	-0.01 ± 0.03	0.04 ± 0.03
3.5	40	8	60	10	-0.04 ± 0.03	0.03 ± 0.03	-0.04 ± 0.03	0.03 ± 0.03
4.0	40	8	60	10	-0.12 ± 0.08(*)	0.35 ± 0.08 (*)	-0.02 ± 0.03	0.01 ± 0.03

Table 4.8: Fit parameters in case of SF to the proper time measurement (expressed in sigma units) for the $B_s \to hh$ channel. Input bias and resolution parameters are listed together with the fit outputs A_{CP}^{dir} and A_{CP}^{mix}. The values indicated by the (*) symbol

Conclusions

The time dependent analyses of B decays play a key role in the study of the *CP* violation. In my thesis I focused the attention on the measurements of the B proper decay time, which is a crucial element in time dependent *CP* analyses.

B lifetime can be calculated knowing its distance of flight (from the production vertex **PV**, to the decay vertex **SV**) and its momentum **p**. The **PV** is measured with a common vertex fit of all track segments reconstructed in the vertex detector, while **SV** and the B momentum are determined by a common vertex fit of the stable B decay products. For a generic measurement of a track parameter or vertex coordinate $\mathbf{y_i}$, adjusted by a fit procedure with kinematical constraints, we can define the normalized "stretch values" or "FITPulls", given by:

$$^{FIT}Pulls(y_i) = \frac{\Delta \mathbf{y}_i}{\sqrt{\mathbf{cov}_{ii} - \mathbf{V}(\hat{\mathbf{y}})_{ii}}}$$

where $\Delta \mathbf{y}_i$ represents the difference between value of the measurement before and after the fit process, whereas in the denominator we put in the difference of the two variances, the two corresponding variances. If the measured data are gaussian distributed and the linearization of the equations constraints exploited in the fit is a good approximation within the range spread by the measurements, FITPulls turn out to be distributed as normal gaussians ($\mu = 0$, $\sigma = 1$). It is reasonable to expect that if one of the conditions above is not satisfied a deviation from normality of their shape should appear.

On real data, the method can be used on the control channel $J/\Psi \rightarrow \mu\mu$, — chosen since the prompt J/Ψ will be a strong signal in dimuon triggered events (~170Hz@LHCb) with a low background level (B/S~24%) — as a general monitor for the charged tracks calibration and to recover systematic effects that can compromise the B proper time measurement. In this way we can think of a correction strategy, built on a clean channel, but exportable to others physical decays.

Thanks to the results of this thesis, the FITPull method will be adopted by the LHCb Collaboration to monitor and calibrate the quality of the tracking algorithms. I have developed an iterative method to extract, starting from the FITPull distributions, a map of the corrections of the track parameters as a function of the momentum of the input charged tracks. In order to perform these tasks, I developed a kinematical fitter as a general software tool, the `GlobalFitter`, that has been included in the official LHCb software analysis framework. The `GlobalFitter` has been explicitly designed to compute the FITPulls and the proper time error by taking into account the full covariance matrices of the input measurements.

Furthermore, by using the `RooFit` package (a software tool for statistical modelizations and fits), I have evaluated the effects of the proper time resolution on *CP* violation parameters. In order to do that I have generated several data samples of B decays by means of a fast Monte Carlo technique, and then fitted the theoretical expressions of the decay rates to the simulated data. I

considered two different cases, $B_s \to D_s\pi$ and $B \to h^+h^-$ (where h stands for π or K), to quantify how biasies and scale factors, applied to the proper time error distribution, can affect the fit output values. The former channel is used to measure the mass difference of the B_s mass eigenstates Δm_s and the mistag probability ω_{tag}, whereas the second one provides relevant CP violation measurements. By means of these tests, I estimated how much the time dependent analyses improve by using the proper time error as an event-by-event observable with respect to the case in which a fixed resolution is assumed for all the events.

A strong dependence of ω_{tag} on the presence of a scale factor in the proper time measurement has been observed. It demonstrates the importance of a good estimation of the proper time error in order to obtain a correct ω_{tag} measurement. Similarly, an important dependence of the Δm_s measurement on the bias has been demonstrated.

The fit results for the $B \to h^+h^-$ decays show that the direct CP asymmetry coefficient A_{CP}^{dir} is only slightly affected, if the scaling factor is less than 2 units, while for bigger values the fit results are no longer statistically compatible to the generated ones. Concerning the mixing-induced CP asymmetry parameter A_{CP}^{mix}, the dependence on the scaling factor is even larger.

The conclusion of these studies is that it will be very important to provide a correct proper time measurement, and thus it will be absolutely necessary to provide a reliable calibration technique running on experimental data. For this reason the FITPull method has been adopted by the LHCb Collaboration.

Appendix A

The Least Squares Principle

Least squares is a mathematical optimization technique which, when given a series of measured data, attempts to find a function which closely approximates the data (a "best fit"). It attempts to minimize the sum of the squares of the ordinate differences (called residuals) between points generated by the function and corresponding points in the data.

Given a random variable with an expectation value defined as:

$$y(x) = f(x, a) \tag{4.28}$$

where the function f depends linearly on parameters $a_{j=1,...p}$.

$$f(x_i, a) = a_1 f_1(x_i) + a_2 f_2(x_i) + ... + a_p f_p(x_i)$$

Taken a set of measurements $y_{i=1,..n}$ we have an expectation value for each measurement that is according to eq.4.28

$$E[y_i] = f(x_i, \overline{a})$$

where $\overline{a}$ represents the true values of the parameters.

We establish the term "*residual*" the difference between the true value and the measured one:

$$r_i = f(x_i, \overline{a}) - y_i \tag{4.29}$$

that has an expectation value

$$E[r_i] = 0 \tag{4.30}$$

Then, the principle of least squares requires a minimization of the sum of the residuals above shown

$$S = \sum_{i=1}^{n} r_i^2 = \min = \sum_{i=1}^{n} \left(f(x_i, a) - y_i\right)$$

The essential property for the minimization of S is that the derivatives vanish:

$$\begin{array}{l} \frac{\partial S}{\partial a_1} = 2 \sum_{i=1}^{n} f_1(x_i) \left(a_1 f_1(x_i) + a_2 f_2(x_i) + ... + a_p f_p(x_i) - y_i\right)^2 \\ \frac{\partial S}{\partial a_2} = 2 \sum_{i=1}^{n} f_2(x_i) \left(a_1 f_2(x_i) + a_2 f_2(x_i) + ... + a_p f_p(x_i) - y_i\right)^2 \\ ... \\ \frac{\partial S}{\partial a_p} = 2 \sum_{i=1}^{n} f_p(x_i) \left(a_1 f_p(x_i) + a_2 f_p(x_i) + ... + a_p f_p(x_i) - y_i\right)^2 \end{array}$$

In a matricial form we can write

$$A = \begin{pmatrix} f_1(x_1) & f_2(x_1) & ... & f_p(x_1) \\ f_2(x_1) & f_2(x_2) & ... & f_p(x_2) \\ ... & & & \\ f_1(x_n) & f_2(x_n) & ... & f_p(x_n) \end{pmatrix} \quad a = \begin{pmatrix} a_1 \\ a_2 \\ a_3 \\ a_4 \end{pmatrix}$$

and

$$r = A\,a - y$$

hence

$$\begin{aligned} S &= r^T r \\ &= (A\,a - y)^T (A\,a - y) \\ &= y^T y - 2a^T A^T y + a^T A^T A a \end{aligned} \tag{4.31}$$

The minimization is fulfilled by

$$-2A^T y + 2A^T A\,a = 0 \;\Rightarrow\; \hat{a} = (A^T A)^{-1} A^T y \tag{4.32}$$

Then inserting the eq.4.32 in eq.**??**

$$\hat{S} = y^T y - 2\hat{a}^T A^T y + \hat{a}^T A^T A (A^T A)^{-1} A^T y = y^T y - \hat{a}^T A^T y = y^T y - y^T A \hat{a} \tag{4.33}$$

To calculate the expectation value we have to express the above expression in terms of $\overline{a}$ (true vector of parameters) instead $\hat{a}$ (estimated parameters). The least squares $\hat{a} = (A^T A)^{-1} A^T y$ are unbiased estimates of $\overline{a}$:

$$E[\hat{a}] = (A^T A)^{-1} A^T E[y] = (A^T A)^{-1} A^T A \overline{a} = \overline{a}$$

since the expectation value for the quantity $A\overline{a} - y$ is:

$$E[A\overline{a} - y] = 0 \;\Rightarrow\; E[y] = A\overline{a}$$

Hence

$$\hat{S} = (A\,\overline{a} - y)^T \left(I_n - A\,C^{-1} A^T\right) (A\,\overline{a} - y) \equiv z^T U z \tag{4.34}$$

Also we can notice that

$$\begin{aligned} E[z] &= E[A\,\overline{a} - y] = 0 \\ V[z] &= V[A\,\overline{a} - y] = \sigma^2 I_n \end{aligned} \tag{4.35}$$

so we can observe that

$$V[z_i] = E[z_i^2] = \sigma^2 \qquad E[z_i z_j] = 0$$

Then the expectation value of $\hat{S}$ is given by:

$$E[\hat{S}] = \sum_i U_{ii} E[z_i^2] = \sigma^2 Trace(U)$$

The trace of a square matrix is the sum of its diagonal elements that in this case is

$$Trace(U) = n - p$$

and therefore

$$E[\hat{S}] = \sigma^2 (n - p) \tag{4.36}$$

Appendix B

MCPull and FITPull theory

Given a decay to be reconstructed, the `GlobalFitter` provides the measured quantities corrected and the estimated unknown parameters. with their errors. The reliability of the results are guaranteed by some new mathematical quantities.

Working with Monte Carlo data, it achieves to verify if the solutions found are consistent with Monte Carlo truth. We introduce the concept of "*stretch function*":

$$^{MC}Pull_i = \frac{t_i - m_i}{\sigma_{m_i}} \tag{4.37}$$

where t_i stands for the Monte Carlo truth, whereas the m_i and are the measured (or fitted) quantities and their errors. For example the proper time value is returned with its error, so the stretch function is

$$^{MC}Pull_{\hat{\tau}} = \frac{t_\tau - \hat{\tau}}{\sigma_{\hat{\tau}}} \tag{4.38}$$

If the propertime and the proper time error are correct, the stretch function $^{MC}Pull$ follows a normal distribution with $\mu = 0$ and $\sigma = 1$ for the central limit theorem [22]. This stretch function has only one problem. It stresses the Monte Carlo information which, in the real world, it doesn't exist. We need a mathematical tool, which has to be independent of the Monte Carlo information. We propose the $^{FIT}Pull$ function:

$$^{FIT}Pull_i = \frac{m_i - \hat{y_i}}{\sqrt{\sigma^2_{m_i} - \sigma^2_{\hat{y}_i}}} \tag{4.39}$$

where m_i and σ_{m_i} are the measurement and its error, and $\hat{y_i}$ and $\sigma_{\hat{y}_i}$ are the same quantities but calculated after the fitting procedure. How is distributed this mathematical value? We can write

$$\hat{y} = m - \Delta y \qquad cov(\hat{y}) = J_y^T \cdot cov(m) \cdot J_y \tag{4.40}$$

.

The conditions for the linearization are expressed as:

$$g_k(a^*, y^*) + \sum_j \frac{\partial g_k}{\partial a_j} (\Delta a_j - \Delta a^*) + \sum_j \frac{\partial g_k}{\partial y_j} (\Delta y_j - \Delta y^*) \approx 0 \qquad (4.41)$$

where the functions and the derivatives are computed in $a^* = a + \Delta a^*$ and

$y^* = y + \Delta y^*$. In a matricial form we can summarize:

$$g + A(\Delta a - \Delta a^*) + B(\Delta y - \Delta y^*) = 0 \Rightarrow$$

$$A \cdot \Delta a + B \cdot \Delta y = c \qquad c = A \cdot \Delta a^* + B \cdot \Delta y^* - g$$

and

$$A = \begin{pmatrix} \frac{\partial g_1}{\partial a_1} & \frac{\partial g_1}{\partial a_2} & \cdots & \frac{\partial g_1}{\partial a_p} \\ \cdots & \cdots & \cdots & \cdots \\ \cdots & \cdots & \cdots & \cdots \\ \frac{\partial g_m}{\partial a_1} & \frac{\partial g_m}{\partial a_2} & \cdots & \frac{\partial g_m}{\partial a_p} \end{pmatrix}$$

$$B = \begin{pmatrix} \frac{\partial g_1}{\partial y_1} & \frac{\partial g_1}{\partial y_2} & \cdots & \frac{\partial g_1}{\partial y_n} \\ \cdots & \cdots & \cdots & \cdots \\ \cdots & \cdots & \cdots & \cdots \\ \frac{\partial g_m}{\partial y_1} & \frac{\partial g_m}{\partial y_2} & \cdots & \frac{\partial g_m}{\partial a y_n} \end{pmatrix}$$

$$g = \begin{pmatrix} g_1(a^*, y^*) \\ g_2(a^*, y^*) \\ ... \\ g_m(a^*, y^*) \end{pmatrix}$$

So the new function to be minimized can be written as

$$\Lambda = \Delta y^T \, W \, \Delta y + 2\lambda^T \left(A \cdot \Delta a + B \cdot \Delta y - c \right) \tag{4.42}$$

$$\frac{\partial \Lambda}{\partial \left(\Delta y, \lambda, \Delta a \right)} = 0 \qquad \Rightarrow$$

$$\begin{array}{l} W\Delta y + B^T \lambda = 0 \\ A^T \lambda = 0 \\ B\Delta y + A\Delta a = c \end{array} = \begin{pmatrix} W & 0 & B^T \\ 0 & 0 & A^T \\ B & A & 0 \end{pmatrix} \cdot \begin{pmatrix} \Delta y \\ \Delta a \\ \lambda \end{pmatrix} = \begin{pmatrix} 0 \\ 0 \\ c \end{pmatrix} \tag{4.43}$$

This linear system can be solved through the standard numerical methods by

the inversion

$$G^{-1} = \begin{pmatrix} W & 0 & B^T \\ 0 & 0 & A^T \\ B & A & 0 \end{pmatrix}^{-1} = \begin{pmatrix} C_{11} & C_{21}^T & C_{31}^T \\ C_{21} & C_{22} & C_{32}^T \\ C_{31} & C_{32} & C_{33} \end{pmatrix}$$

Introducing the abbreviations

$$W_B = \left(B W^{-1} B^T \right)^{-1} \tag{4.44}$$

$$W_A^{-1} = \left(A^T W_B A\right)^{-1} \tag{4.45}$$

We can solve the inversion (for more details [19], [20]) and if we realize that

the matrix G is a sparse matrix. Applying the

$$\begin{aligned}
C_{11} &= W^{-1} - W^{-1}\, B^T\, W_B\, B\, W^{-1} + W^{-1} B^T\, W_B\, A\, W_A^{-1}\, A^T\, W_B\, B\, W^{-1} \\
C_{21} &= -W_A^{-1}\, A^T\, W_B\, B\, W^{-1} \\
C_{22} &= W_A^{-1} \\
C_{31} &= W_B\, B\, W^{-1} - W_B A W_A^{-1} A^T W_B B W^{-1} \\
C_{32} &= W_B A W_A^{-1} \\
C_{33} &= -W_B + W_B A W_A^{-1} A^T W_B
\end{aligned} \tag{4.46}$$

From the eq.4.43

$$W^{-1}(W\Delta y + B^T\lambda) = 0 \quad \Rightarrow \quad \Delta y = -W^{-1}B^T\lambda \tag{4.47}$$

hence

$$-BW^{-1}B^T\lambda + A\Delta a = c \quad \Rightarrow \quad \lambda = (BW^{-1}B^T)^{-1}(A\Delta a - c)$$

$$A^T\lambda = 0 = A^T((BW^{-1}B^T)^{-1}(A\Delta a - c)) \quad \Rightarrow \quad A^T(BW^{-1}B^T)^{-1}A\Delta a = A^T(BW^{-1}B^T)^{-1}c$$

$$W_A\Delta a = A^T W_B c \Rightarrow \Delta a = W_A^{-1}A^T W_B c$$

$$\Delta y = -W^{-1}B^T(BW^{-1}B^T)^{-1}(AW_A^{-1}A^T W_B - 1)c = W^{-1}B^T W_B c - W^{-1}B^T W_B A W_A^{-1}A^T W_B c$$

Ergo

$$\frac{\partial(\Delta y)}{\partial y} = -W^{-1}B^T W_B B + W^{-1}B^T W_B A W_A^{-1}A^T W_B B \quad \Rightarrow$$

$$V(\Delta y) = \left(-W^{-1}B^T W_B B + W^{-1}B^T W_B A W_A^{-1} A^T W_B B\right) V(y) \cdot$$
$$\cdot \left(-W^{-1}B^T W_B B + W^{-1}B^T W_B A W_A^{-1} A^T W_B B\right)^T$$

$$= \left(-W^{-1}B^T W_B B + W^{-1}B^T W_B A W_A^{-1} A^T W_B B\right) V(y) \cdot$$
$$\cdot \left(-B^T W_B B W^{-1} + B^T W_B A W_A^{-1} A^T W_B B W^{-1}\right) =$$

$$= W^{-1}B^T W_B W_B^{-1} W_B B W^{-1} - W^{-1}B^T W_B A W_A^{-1} A^T W_B W_B^{-1} W_B B W^{-1} +$$
$$-W^{-1}B^T W_B A W_A^{-1} A^T W_B W_B^{-1} W_B B W^{-1} + W^{-1}B^T W_B A W_A^{-1} A^T W_B W_B^{-1} W_B A W_A^{-1} A^T W_B B W^{-1} =$$

$$= W^{-1}B^T W_B B W^{-1} - W^{-1}B^T W_B A W_A^{-1} A^T W_B B W^{-1} \tag{4.48}$$
$$-W^{-1}B^T W_B A W_A^{-1} A^T W_B B W^{-1} + W^{-1}B^T W_B A W_A^{-1} W_A W_A^{-1} A^T W_B B W^{-1} =$$

$$= W^{-1}B^T W_B B W^{-1} - W^{-1}B^T W_B A W_A^{-1} A^T W_B B W^{-1} \tag{4.49}$$

So the covariance of Δy is just the difference between $V(y)$ and $V(\hat{y})$:

$$V(\Delta y) = V(y) - V(\hat{y}) \tag{4.50}$$

thus the normalized stretch function is

$${}^{FIT}Pull_i = \frac{\Delta y_i}{\sqrt{(V(y)_{ii} - V(\hat{y})_{ii})}} = \frac{y_i - \hat{y}_i}{\sqrt{(V(y)_{ii} - V(\hat{y})_{ii})}} \tag{4.51}$$

where y_i is the measurement and the $\hat{y}_i$ is the same measurement but after the fitting procedure. This is the equation 4.39. **If the measured data are normally distributed and the condition are linear, the FITPulls should follows the standardized Gaussian distribution** (mean=0, sigma=1) [19]. In fact we can consider the Δy as the deviation from the zero, i.e. we are substituting the "truth" with "0" and the measurements with Δy in the eq. 4.37.

Appendix C

The `GlobalFitter` *Tool*

In this section I report summarily the `LagrangeGlobalFitter` class definition with its most important methods. The `GlobalFitter` can be invoked by means of three overloaded public methods, `StatusCode fit`(....). Depending on the passed arguments, a different output can be chosen. Nevertheless all the three methods are based on the common function `fitFromEverything`(....) which implements the matrix inversion as described in par. 3.3.1.

```
class LagrangeGlobalFitter : public GaudiTool, virtual public IGlobalFitter {

public:

  ///Standard constructor
  LagrangeGlobalFitter( const std::string& type, const std::string& name,
            const IInterface* parent);

  ///Destructor
  ~LagrangeGlobalFitter() {
    MParStore.clear();
    UNParStore.clear();
    MVtxStore.clear();
    UNVtxStore.clear();
    SelectParticle.clear();
    ProductionVertex.clear();
    DecayVertex.clear();
  }

  StatusCode initialize();
  StatusCode finalize();


  StatusCode fit(Vertex &WorkingVertex);  ///< Fit from a Vertex
```

```
  ///Fit from a Vertex and retrieve the proper time and its error
//of the particle/particles selected
  StatusCode fit(Vertex &WorkingVertex, std::vector < double >&,
         std::vector < double >&);


  StatusCode fit(Particle &WorkingParticle); ///< Fit from a Particle

  //Retrieve Pulls
  ///Retrieve the function FitPULL for measured particle computed
//with all the track parameters transported in the z

  StatusCode getFitPull(Particle &previousP, Particle &afterP, HepVector &pull);

 /// Retrieve the function FitPULL for a measured particle
  StatusCode getFitPull(Vertex &previousV, Vertex &afterP, HepVector &pull);

  ///Set which particle to compute the lifetime
  void setWhichParticleLifetime(Particle *);

  .........

}

StatusCode LagrangeGlobalFitter::fit(Vertex &inVertex)  {

        //Fit From Vertex
        HepMatrix Minv;
        int nm;
        Particle dummy;
        StatusCode sc=fitFromEverything(inVertex, dummy, true, Minv, nm);
        if (sc.isFailure()) return StatusCode::FAILURE;

        return StatusCode::SUCCESS;

}

StatusCode LagrangeGlobalFitter::fit(Vertex &inVertex, std::vector
< double > &lifeTime, std::vector <double > &lifeTimeErr)
{
        //Fit from Vertex and retrieve lifetime and its error
        double lfTime, lfTimeErr;
        HepMatrix Minv;
        int nm;
        Particle dummy;
```

```
        StatusCode sc=fitFromEverything(inVertex, dummy, true, Minv, nm);
        if (sc.isFailure()) return StatusCode::FAILURE;

        for (unsigned int i=0; i< SelectParticle.size(); i++)
        {
                lifeTimeCalculator(inVertex, Minv, i, nm, lfTime, lfTimeErr);
                lifeTime.push_back(lfTime);
                lifeTimeErr.push_back(lfTimeErr);
        }


        resetVars();

        return StatusCode::SUCCESS;
}

StatusCode LagrangeGlobalFitter::fit(Particle &inParticle)  {
        debug() << "fit from Particle..." << endmsg;
        HepMatrix Minv;
        int nm;
        Vertex dummy;
        return fitFromEverything(dummy, inParticle, false, Minv, nm);

}

StatusCode LagrangeGlobalFitter::fitFromEverything(Vertex &inVertex,
Particle &inParticle, bool isFromVertex,HepMatrix &V, int& num_m) {


        info() << "Starting global fit ...." << endmsg;

        StatusCode sc;

        Vertex *workingVertex=&inVertex;
        Particle *workingParticle=&inParticle;

        debug() << "Compute NdF" << endmsg;
        // then compute number of measurements, of unmeasurements, of contraints;
        int nm, nu, nc;
        if(isFromVertex) {
                sc = computeDoF(*workingVertex, nm, nu, nc);
        } else {
                sc = computeDoF(*workingParticle, nm, nu, nc);
        }
        if(sc.isFailure()) {
                error() << "cannot compute DoF" << endmsg;
```

```
                resetVars();
                return StatusCode::FAILURE;
        }

        debug() << "Number of measured variables   " << nm << endmsg;
        debug() << "Number of unmeasured variables " << nu << endmsg;
        debug() << "Number of constraints           " << nc << endmsg;
        debug() << "Number of degrees of freedom    " << nc-nu << endmsg;

        num_m=nm;



        // Second get initial estimate of unmeasured variables and transport measurements
        //to approximate vertices
        // (in the meanwhile fill vector of measurements, its
//covariance and vector of unmeasured
        HepSymMatrix Ce(nm, 0);
        HepVector e(nm,0);
        HepVector u(nu,0);
        if(isFromVertex) {
                sc = estimateAndTransport(Ce, e, u, *workingVertex);
        } else {
                sc = estimateAndTransport(Ce, e, u, *workingParticle);
        }
        if(sc.isFailure()) {
                error() << "cannot get initial estimates" << endmsg;
                resetVars();

                return StatusCode::FAILURE;
        }
        sc = checkCovariance(Ce, nm);
        if (sc.isFailure() ) {
                error() << "covariance matrix after transport check
failed... something fishy"
                << endmsg;

                resetVars();
         return StatusCode::FAILURE;
        }

        debug()<< "e " << e << endmsg;
        debug()<< "u " << u << endmsg;

        // copy parameter vector to save initial values (later used to compute chi2)
```

```
      HepVector e0(e);
      // save covariance matrix to be used for chi2 calculation
      HepSymMatrix Ce0(Ce);

      HepMatrix B_m(nc, nm, 0);
      HepMatrix C_m(nc, nu, 0);
      HepMatrix Minv_m(nm+nu+nc, nm+nu+nc, 0);

      // now start loop of linearized constraints
      bool final = false; // convergence flag
      int  icount= 0; // number of iterations counter
// iterate with linearized constraints until convergence
//------------------------------------------- iterate over icount
      while (icount < m_maxIterations) {

              // get constraint unmbalance and check them
              HepVector constraint(nc,0); // vector of non linear constraints
              if(isFromVertex) {
                      final=computeConstraint(e, u, *workingVertex, constraint);
              } else {
                      final=computeConstraint(e, u, *workingParticle, constraint);
              }

              // check that momenta are physical
              if(isFromVertex) {
                      sc = checkMomenta(*workingVertex, e, u);
              } else {
                      sc = checkMomenta(*workingParticle, e, u);
              }

              if ( sc.isFailure() )
              {
                      error() << "momenta out of range " << endmsg;
                      resetVars();
                      return StatusCode::FAILURE;
              }


              // converged !!
              if(final) break;


              // update variables e and u with linearized constraints
              HepMatrix B(nc, nm, 0);
              HepMatrix C(nc, nu, 0);
              HepMatrix Minv(nm+nu+nc, nm+nu+nc, 0);
```

```
  if(isFromVertex) {
          sc = iterateWithLinearConstraint
(Ce, e, u, nm, nu, nc, *workingVertex, constraint, B, C, Minv);
  } else {
          sc = iterateWithLinearConstraint
(Ce, e, u, nm, nu, nc, *workingParticle, constraint, B, C, Minv);
  }
  if ( sc.isFailure() ) {
          error() << "iteration " << icount+1 << " failed" << endmsg;
          resetVars();
          return StatusCode::FAILURE;
  }


  // save maxtrices for subsequent usage
  B_m=B;
  C_m=C;
  Minv_m=Minv;


  icount = icount + 1;

  debug()<< "Treasure Map" << endmsg;
  debug()<< "Measured Particles " << endmsg;
  for (std::map<Particle*,int>::iterator i=MParStore.begin();i!=MParStore.end
          debug() << i->second << " " << " " << i->first << endmsg;

  debug()<< "UnMeasured Particles " << endmsg;
  for (std::map<Particle*,int>::iterator i=UNParStore.begin();i!=UNParStore.e
          debug() << i->second << " " << " " << i->first << endmsg;

  debug()<< "Measured Vertexes " << endmsg;
  for (std::map<Vertex*,int>::iterator i=MVtxStore.begin();i!=MVtxStore.end()
          debug() << i->second << " " << " " << i->first << endmsg;

  debug()<< "UnMeasured Vertexes " << endmsg;
  for (std::map<Vertex*,int>::iterator i=UNVtxStore.begin();i!=UNVtxStore.end
          debug() << i->second << " " << " " << i->first << endmsg;

}



// if not converged, return
if(!final) {
```

```
            error() << "Sorry, no convergence" << endmsg;
            error()<< "Reached maximum number of iterations = "<< icount << endmsg;
            error() <<"If you think this event
     should be reconstructed and if you have a huge number of constraints,";
error() << "try to increase maxIterations in job options" << endmsg;
            error() << "If it doesn't help, please contact experts" << endmsg;
            return StatusCode::FAILURE;
    } else {

   info() << "GlobalFitter converged after " << icount << " iterations!" << endmsg;
    }


    // update the covariance matrix
    HepSymMatrix Cu(nu,0);

    updateCovariance(Ce, Cu, Minv_m, nm, nu);

    // check the covariance matrix
    sc = checkCovariance(Ce, Cu, nm, nu);
    if (sc.isFailure() ) {
            error() << "covariance matrix check failed... something fishy" << endmsg;
            resetVars();
            return StatusCode::FAILURE;
    }

    // build up output graph

    if(isFromVertex) {
            ////SV
            for(SmartRefVector<Particle>::iterator it=workingVertex->products().begin()
    it!=workingVertex->products().end();
    it++) {
                    debug() << " z Particle" << (*it)->pointOnTrack().z()<<" zo "<< u(3)
            }

            sc=fillDecayGraph(Ce0, e0, Ce, e, Cu, u, *workingVertex, nc-nu);
            if(sc.isFailure())
{
  resetVars();

  return StatusCode::FAILURE;
            }

    } else {
            sc=fillDecayGraph(Ce0, e0, Ce, e, Cu, u, *workingParticle, nc-nu);
```

```
            if(sc.isFailure())
    {
      resetVars();

      return StatusCode::FAILURE;
    }

        }

        V=Minv_m;
        // exit with deserved success!
        return StatusCode::SUCCESS;
}
```

Appendix D

A little algebra for A_{CP} asymmetries

We have seen that, for a flavour specific process, the decay ratio of a neutral B meson in its final state $\bar{f}$ is calculated as indicated in these lines:

$$\mathcal{R}\left(B \to \bar{f}\right) = e^{-\Gamma t}\left[\cosh\left(\frac{\Delta\Gamma}{2}t\right) + (1-2\omega)\cos\Delta m_s t\right] \otimes \frac{1}{\sqrt{2\pi}\sigma} e^{-\frac{(\tau-t)^2}{2\sigma^2}} \tag{4.52}$$

$$= \int_{-\infty}^{\infty} e^{-\Gamma t}\left[\cosh\left(\frac{\Delta\Gamma}{2}t\right) + (1-2\omega)\cos\Delta m_s t\right] \cdot \frac{1}{\sqrt{2\pi}\sigma} e^{-\frac{(\tau-t)^2}{2\sigma^2}} dt =$$

Really the convolution should be computed between 0 and $+\infty$ because the time is not defined for negative values. Notwithstanding this reasoning, we chose to compute the integral, for mathematical simplicity, from $-\infty$. The result should not be so much modified since due to the acceptance function, that cancels the integral for values near zero.

$$= \int_{-\infty}^{\infty} e^{-\Gamma t}\left[\frac{e^{\frac{\Delta\Gamma}{2}t} + e^{-\frac{\Delta\Gamma}{2}t}}{2} + (1-2\omega)\,\frac{e^{i\Delta m_s t} + e^{-i\Delta m_s t}}{2}\right] \cdot \frac{1}{\sqrt{2\pi}\sigma} e^{-\frac{(\tau-t)^2}{2\sigma^2}} dt =$$

$$= \frac{1}{\sqrt{2\pi}\sigma}\int_{-\infty}^{\infty} e^{-\Gamma t}\cdot$$

$$\cdot\left[\frac{e^{\frac{\Delta\Gamma}{2}t}\cdot e^{-\frac{(t-\tau)^2}{2\sigma^2}} + e^{-\frac{\Delta\Gamma}{2}t}\cdot e^{-\frac{(t-\tau)^2}{2\sigma^2}}}{2} + (1-2\omega)\cdot\frac{e^{i\Delta m_s t}\cdot e^{-\frac{(t-\tau)^2}{2\sigma^2}} + e^{-i\Delta m_s t}\cdot e^{-\frac{(t-\tau)^2}{2\sigma^2}}}{2}\right] dt =$$

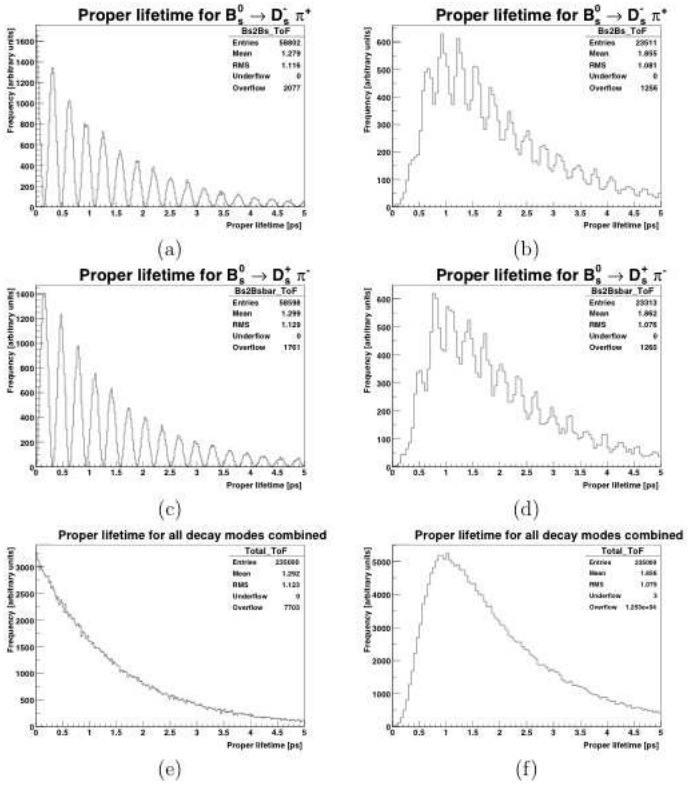

Figure 4.11: On the left there are the true proper lifetime distributions for $B_s \to D_s^- \pi^+$ and $B_s \to D_s^+ \pi^-$. On the right column there arethe same distributions after the acceptance, resolution and mistag effects were applied. The last line, picture (e) and (f), contains the untagged distributions before and after.

$$= \frac{1}{2\sqrt{2\pi}\sigma}\int_{-\infty}^{\infty} e^{-\Gamma t}\cdot e^{\frac{\Delta\Gamma}{2}t}\cdot e^{-\frac{(t-\tau)^2}{2\sigma^2}} + \frac{1}{2\sqrt{2\pi}\sigma}\int_{-\infty}^{\infty} e^{-\Gamma t}\cdot e^{-\frac{\Delta\Gamma}{2}t}\cdot e^{-\frac{(t-\tau)^2}{2\sigma^2}} +$$

$$+\frac{(1-2\omega)}{2\sqrt{2\pi}\sigma}\int_{-\infty}^{\infty} e^{-\Gamma t}\cdot e^{i\Delta m_s t}\cdot e^{-\frac{(t-\tau)^2}{2\sigma^2}} + \frac{(1-2\omega)}{2\sqrt{2\pi}\sigma}\int_{-\infty}^{\infty} e^{-\Gamma t}\cdot e^{-i\Delta m_s t}\cdot e^{-\frac{(t-\tau)^2}{2\sigma^2}} =$$

$$= \underbrace{\frac{1}{2\sqrt{2\pi}\sigma}\int_{-\infty}^{\infty} e^{\frac{\Delta\Gamma}{2}t}.....}_{\mathbf{I_1}} \qquad + \underbrace{\frac{1}{2\sqrt{2\pi}\sigma}\int_{-\infty}^{\infty} e^{-\frac{\Delta\Gamma}{2}t}.....}_{\mathbf{I_2}} \qquad +$$

$$\underbrace{\frac{(1-2\omega)}{2\sqrt{2\pi}\sigma}\int_{-\infty}^{\infty} e^{i\Delta m_s t}.....}_{\mathbf{I_3}} \qquad + \underbrace{\frac{(1-2\omega)}{2\sqrt{2\pi}\sigma}\int_{-\infty}^{\infty} e^{-i\Delta m_s t}.....}_{\mathbf{I_4}}$$

$$\mathbf{I_{1,2}} = \frac{1}{2\sqrt{2\pi}\sigma}\int_{-\infty}^{\infty} e^{\pm\frac{\Delta\Gamma}{2}t}.e^{-\Gamma t}.e^{-\frac{(\tau-t)^2}{2\sigma^2}}dt = \frac{1}{2\sqrt{2\pi}\sigma}\int_{-\infty}^{\infty} e^{\pm\frac{\Delta\Gamma}{2}t}.e^{-\Gamma t}.e^{-\frac{\tau^2}{2\sigma^2}}e^{-\frac{t^2}{2\sigma^2}}.e^{\frac{\tau t}{\sigma^2}}dt \tag{4.53}$$

$$= \frac{e^{-\frac{\tau^2}{2\sigma^2}}}{2\sqrt{2\pi}\sigma}\int_{-\infty}^{\infty} e^{\pm\frac{\Delta\Gamma}{2}t}\cdot e^{-\Gamma t}\cdot e^{-\frac{t^2}{2\sigma^2}}\cdot e^{\frac{\tau t}{\sigma^2}}dt = \frac{e^{-\frac{\tau^2}{2\sigma^2}}}{2\sqrt{2\pi}\sigma}\int_{-\infty}^{\infty} e^{-\left(\Gamma\mp\frac{\Delta\Gamma}{2}-\frac{\tau}{\sigma^2}\right)t}\cdot e^{-\frac{t^2}{2\sigma^2}}dt$$

$$c \equiv \left(\Gamma \mp \frac{\Delta\Gamma}{2} - \frac{\tau}{\sigma^2}\right)$$

$$\mathbf{I_{1,2}} = \frac{e^{-\frac{\tau^2}{2\sigma^2}}}{2\sqrt{2\pi}\sigma}\int_{-\infty}^{\infty} e^{-ct}\cdot e^{-\frac{t^2}{2\sigma^2}}dt = \frac{e^{-\frac{\tau^2}{2\sigma^2}}}{2\sqrt{2\pi}\sigma}\int_{-\infty}^{\infty} e^{-\left(\frac{t}{\sqrt{2}\sigma}+\frac{c}{\sqrt{2}}\sigma\right)^2}\cdot e^{+\frac{c^2\sigma^2}{2}}dt =$$

$$= \frac{e^{-\left(\frac{\tau^2}{2\sigma^2}-\frac{c^2\sigma^2}{2}\right)}}{2\sqrt{2\pi}\sigma}\int_{-\infty}^{\infty} e^{-\left(\frac{t}{\sqrt{2}\sigma}+\frac{c}{\sqrt{2}}\sigma\right)^2}\cdot dt$$

$$y \equiv \frac{t}{\sqrt{2}\sigma}+\frac{c}{\sqrt{2}}\sigma \qquad \Rightarrow \qquad dy = \frac{dt}{\sqrt{2}\sigma}$$

$$\mathbf{I_{1,2}} = \frac{e^{-\left(\frac{\tau^2}{2\sigma^2}-\frac{c^2\sigma^2}{2}\right)}}{2\sqrt{2\pi}\sigma}\int_{-\infty}^{\infty} e^{-y^2}\sqrt{2}\sigma\cdot dy = \frac{e^{-\left(\frac{\tau^2}{2\sigma^2}-\frac{c^2\sigma^2}{2}\right)}}{2\sqrt{2\pi}\sigma}\sqrt{2}\sigma\sqrt{2\pi} =$$

$$= \frac{e^{-\left(\frac{\tau^2}{2\sigma^2}-\frac{c^2\sigma^2}{2}\right)}}{\sqrt{2}} = \frac{e^{-\left(\frac{\tau^2}{2\sigma^2}-\left(\Gamma\mp\frac{\Delta\Gamma}{2}-\frac{\tau}{\sigma^2}\right)^2\frac{\sigma^2}{2}\right)}}{\sqrt{2}} =$$

$$= \frac{e^{-\left(\frac{\tau^2}{2\sigma^2}-\left(\Gamma\mp\frac{\Delta\Gamma}{2}-\frac{\tau}{\sigma^2}\right)^2\frac{\sigma^2}{2}\right)}}{\sqrt{2}} = \tag{4.54}$$

$$\mathbf{I_1}+\mathbf{I_2} = \frac{e^{-\left(\frac{\tau^2}{2\sigma^2}-\left(\Gamma-\frac{\Delta\Gamma}{2}-\frac{\tau}{\sigma^2}\right)^2\frac{\sigma^2}{2}\right)}}{\sqrt{2}} + \frac{e^{-\left(\frac{\tau^2}{2\sigma^2}-\left(\Gamma+\frac{\Delta\Gamma}{2}-\frac{\tau}{\sigma^2}\right)^2\frac{\sigma^2}{2}\right)}}{\sqrt{2}} =$$

$$= \frac{e^{-\frac{\tau^2}{2\sigma^2}}}{\sqrt{2}}\cdot\left[e^{+\left(\Gamma+\frac{\Delta\Gamma}{2}-\frac{\tau}{\sigma^2}\right)^2\frac{\sigma^2}{2}} + e^{+\left(\Gamma-\frac{\Delta\Gamma}{2}-\frac{\tau}{\sigma^2}\right)\frac{\sigma^2}{2}}\right] =$$

$$= \frac{e^{-\frac{\tau^2}{2\sigma^2}}}{\sqrt{2}}\cdot\left[e^{+\left[\Gamma^2+\left(\frac{\Delta\Gamma}{2}\right)^2+\left(\frac{\tau}{\sigma^2}\right)^2+\Gamma\cdot\Delta\Gamma-2\Gamma\cdot\frac{\tau}{\sigma^2}-\Delta\Gamma\cdot\frac{\tau}{\sigma^2}\right]\frac{\sigma^2}{2}} + e^{+\left[\Gamma^2+\left(\frac{\Delta\Gamma}{2}\right)^2+\left(\frac{\tau}{\sigma^2}\right)^2-\Gamma\cdot\Delta\Gamma-2\Gamma\cdot\frac{\tau}{\sigma^2}+\Delta\Gamma\cdot\frac{\tau}{\sigma^2}\right]\frac{\sigma^2}{2}}\right] =$$

$$= \frac{e^{-\frac{\tau^2}{2\sigma^2}}\cdot e^{+\left[\Gamma^2+\left(\frac{\Delta\Gamma}{2}\right)^2+\left(\frac{\tau}{\sigma^2}\right)^2-2\Gamma\cdot\frac{\tau}{\sigma^2}\right]\frac{\sigma^2}{2}}}{\sqrt{2}}\cdot\left[e^{\frac{\Delta\Gamma}{2}\cdot\frac{\tau}{\sigma^2}\cdot\sigma^2-\frac{\Delta\Gamma}{2}\cdot\Gamma\cdot\sigma^2} + e^{-\frac{\Delta\Gamma}{2}\cdot\frac{\tau}{\sigma^2}\cdot\sigma^2+\frac{\Delta\Gamma}{2}\cdot\Gamma\cdot\sigma^2}\right] =$$

$$= \sqrt{2}e^{-\frac{\tau^2}{2\sigma^2}} \cdot e^{+\left[\Gamma^2+\left(\frac{\Delta\Gamma}{2}\right)^2+\left(\frac{\tau}{\sigma^2}\right)^2-2\Gamma\cdot\frac{\tau}{\sigma^2}\right]\frac{\sigma^2}{2}} \cosh\left(\frac{\Delta\Gamma}{2}\cdot\tau - \frac{\Delta\Gamma}{2}\cdot\Gamma\cdot\sigma^2\right) \quad (4.55)$$

$$= \sqrt{2}e^{+\left[\frac{\Gamma^2\sigma^2}{2}+\frac{\Delta\Gamma^2\sigma^2}{8}-\Gamma\tau\right]} \cosh\left(\frac{\Delta\Gamma}{2}\cdot\tau - \frac{\Delta\Gamma}{2}\cdot\Gamma\cdot\sigma^2\right)$$

$$\mathbf{I_{3,4}} = \frac{(1-2\omega)}{2\sqrt{2\pi}\sigma}\int_{-\infty}^{\infty} e^{-\Gamma t}\cdot e^{\pm i\Delta m_s t}\cdot e^{-\frac{(t-\tau)^2}{2\sigma^2}}dt = \frac{(1-2\omega)\cdot e^{-\frac{\tau^2}{2\sigma^2}}}{2\sqrt{2\pi}\sigma}\int_{-\infty}^{\infty} e^{-t\left(\Gamma\mp i\Delta m_s-\frac{\tau}{\sigma^2}\right)}\cdot e^{-\frac{t^2}{2\sigma^2}}dt =$$

$$g \equiv \left(\Gamma \mp i\Delta m_s - \frac{\tau}{\sigma^2}\right)$$

$$\mathbf{I_{3,4}} = \frac{(1-2\omega)\cdot e^{-\frac{\tau^2}{2\sigma^2}}}{2\sqrt{2\pi}\sigma}\int_{-\infty}^{\infty} e^{-gt}\cdot e^{-\frac{t^2}{2\sigma^2}}dt = \frac{(1-2\omega)\cdot e^{-\frac{\tau^2}{2\sigma^2}}}{2\sqrt{2\pi}\sigma}\int_{-\infty}^{\infty} e^{-\left(\frac{t}{\sqrt{2}\sigma}+\frac{g}{\sqrt{2}}\sigma\right)^2}\cdot e^{+\frac{g^2\sigma^2}{2}}dt =$$

$$= \frac{(1-2\omega)\cdot e^{-\frac{\tau^2}{2\sigma^2}}\cdot e^{\frac{g^2\sigma^2}{2}}}{2\sqrt{2\pi}\sigma}\int_{-\infty}^{\infty} e^{-z^2}dz = \frac{(1-2\omega)\cdot e^{-\frac{\tau^2}{2\sigma^2}}\cdot e^{\frac{g^2\sigma^2}{2}}}{2\sqrt{2\pi}\sigma}\cdot\sqrt{2}\sigma\cdot\sqrt{2\pi} =$$

$$= \frac{(1-2\omega)\cdot e^{-\frac{\tau^2}{2\sigma^2}}\cdot e^{\frac{g^2\sigma^2}{2}}}{\sqrt{2}} = \frac{(1-2\omega)\cdot e^{-\frac{\tau^2}{2\sigma^2}}\cdot}{\sqrt{2}}e^{\frac{\sigma^2}{2}\left(\Gamma\mp i\Delta m_s-\frac{\tau}{\sigma^2}\right)^2} =$$

$$= \frac{(1-2\omega)\cdot e^{-\frac{\tau^2}{2\sigma^2}}\cdot}{\sqrt{2}}e^{\frac{\sigma^2}{2}\left(\Gamma^2-\Delta m_s^2+\frac{\tau^2}{\sigma^4}\mp 2i\Gamma\Delta m_s-2\Gamma\frac{\tau}{\sigma^2}\pm 2i\frac{\tau\Delta m_s}{\sigma^2}\right)} =$$

$$= \frac{(1-2\omega)\cdot e^{-\Gamma\tau}\cdot e^{\frac{\sigma^2\Gamma^2}{2}}\cdot e^{-\frac{\sigma^2\Delta m_s^2}{2}}}{\sqrt{2}} e^{\frac{\sigma^2}{2}\left(-2i\Gamma\Delta m_s \pm 2i\frac{\tau\Delta m_s}{\sigma^2}\right)} =$$

$$= \frac{(1-2\omega)\cdot e^{-\Gamma\tau}\cdot e^{\frac{\sigma^2\Gamma^2}{2}}\cdot e^{-\frac{\sigma^2\Delta m_s^2}{2}}}{\sqrt{2}} e^{\pm i\tau\Delta m_s} e^{\mp i\Gamma\Delta m_s\sigma^2}$$

$$\mathbf{I_3}+\mathbf{I_4} = \sqrt{2}\cdot(1-2\omega)\cdot e^{-\Gamma\tau}\cdot e^{\frac{\sigma^2\Gamma^2}{2}}\cdot e^{-\frac{\sigma^2\Delta m_s^2}{2}}\cos\left(\tau\Delta m_s - \Gamma\Delta m_s\sigma^2\right) \quad (4.56)$$

$$\Rightarrow \quad \mathcal{R}\left(B\to\bar{f}\right) = \mathbf{I_1}+\mathbf{I_2}+\mathbf{I_3}+\mathbf{I_4} =$$

$$= \sqrt{2}\cdot e^{-\Gamma\tau}\left\{e^{+\frac{\Gamma^2\sigma^2}{2}+\frac{\Delta\Gamma^2\sigma^2}{8}}\cosh\left(\frac{\Delta\Gamma}{2}\cdot\tau - \frac{\Delta\Gamma}{2}\cdot\Gamma\cdot\sigma^2\right) + \right.$$
$$\left. + (1-2\omega)\cdot e^{\frac{\sigma^2\Gamma^2}{2}}\cdot e^{-\frac{\sigma^2\Delta m_s^2}{2}}\cos\left(\tau\Delta m_s - \Gamma\Delta m_s\sigma^2\right)\right\} \quad (4.57)$$

In case of bias in our model, we have to substitute the term τ with the $\tau - b$,

where b is the bias expressed in σ units:

$$b = \sigma\cdot\Sigma$$

$$= \sqrt{2}\cdot e^{-\Gamma(\tau-\sigma\cdot\Sigma)}\left\{e^{+\frac{\Gamma^2\sigma^2}{2}+\frac{\Delta\Gamma^2\sigma^2}{8}}\cosh\left(\frac{\Delta\Gamma}{2}\cdot(\tau-\sigma\cdot\Sigma) - \frac{\Delta\Gamma}{2}\cdot\Gamma\cdot\sigma^2\right) + \right.$$
$$\left. + (1-2\omega)\cdot e^{\frac{\sigma^2\Gamma^2}{2}}\cdot e^{-\frac{\sigma^2\Delta m_s^2}{2}}\cos\left((\tau-\sigma\cdot\Sigma)\cdot\Delta m_s - \Gamma\Delta m_s\sigma^2\right)\right\} =$$

$$= \sqrt{2} \cdot e^{-\Gamma\tau} \cdot e^{\Gamma\sigma\cdot\Sigma} \left\{ e^{+\frac{\Gamma^2\sigma^2}{2}+\frac{\Delta\Gamma^2\sigma^2}{8}} \cosh\left(\frac{\Delta\Gamma}{2}\cdot\tau - \frac{\Delta\Gamma}{2}\cdot\sigma\cdot\Sigma - \frac{\Delta\Gamma}{2}\cdot\Gamma\cdot\sigma^2\right) + \right.$$

$$\left. + (1-2\omega)\cdot e^{\frac{\sigma^2\Gamma^2}{2}} \cdot e^{-\frac{\sigma^2\Delta m_s^2}{2}} \cos\left(\tau\cdot\Delta m_s - \sigma\cdot\Sigma\cdot\Delta m_s - \Gamma\Delta m_s\sigma^2\right) \right\}$$

otherwise:

$$\mathcal{R}\left(B\to\bar{f}\right) = e^{-\Gamma t}\left[\cosh\left(\frac{\Delta\Gamma}{2}t\right) + (1-2\omega)\cos\Delta m_s t\right] \otimes \frac{1}{\sqrt{2\pi}\sigma} e^{-\frac{(\tau-b-t)^2}{2\sigma^2}} \tag{4.58}$$

$$= \int_{-\infty}^{\infty} e^{-\Gamma t}\left[\cosh\left(\frac{\Delta\Gamma}{2}t\right) + (1-2\omega)\cos\Delta m_s t\right] \cdot \frac{1}{\sqrt{2\pi}\sigma} e^{-\frac{(\tau-\sigma\Sigma-t)^2}{2\sigma^2}} dt =$$

$$= \int_{-\infty}^{\infty} e^{-\Gamma t}\left[\frac{e^{\frac{\Delta\Gamma}{2}t} + e^{-\frac{\Delta\Gamma}{2}t}}{2} + (1-2\omega)\frac{e^{i\Delta m_s t} + e^{-i\Delta m_s t}}{2}\right] \cdot \frac{1}{\sqrt{2\pi}\sigma} e^{-\frac{(\tau-\sigma\Sigma-t)^2}{2\sigma^2}} dt =$$

$$= \frac{1}{\sqrt{2\pi}\sigma}\int_{-\infty}^{\infty} e^{-\Gamma t}\cdot$$

$$\cdot\left[\frac{e^{\frac{\Delta\Gamma}{2}t}\cdot e^{-\frac{(\tau-\sigma\Sigma-t)^2}{2\sigma^2}} + e^{-\frac{\Delta\Gamma}{2}t}\cdot e^{-\frac{(\tau-\sigma\Sigma-t)^2}{2\sigma^2}}}{2} + (1-2\omega)\cdot\frac{e^{i\Delta m_s t}\cdot e^{-\frac{(\tau-\sigma\Sigma-t)^2}{2\sigma^2}} + e^{-i\Delta m_s t}\cdot e^{-\frac{(\tau-\sigma\Sigma-t)^2}{2\sigma^2}}}{2}\right] dt =$$

$$= \frac{1}{2\sqrt{2\pi}\sigma}\int_{-\infty}^{\infty} e^{-\Gamma t}\cdot e^{\frac{\Delta\Gamma}{2}t}\cdot e^{-\frac{(t\tau-\sigma\Sigma-t)^2}{2\sigma^2}} + \frac{1}{2\sqrt{2\pi}\sigma}\int_{-\infty}^{\infty} e^{-\Gamma t}\cdot e^{-\frac{\Delta\Gamma}{2}t}\cdot e^{-\frac{(\tau-\sigma\Sigma-t)^2}{2\sigma^2}} +$$

$$+\frac{(1-2\omega)}{2\sqrt{2\pi}\sigma}\int_{-\infty}^{\infty} e^{-\Gamma t}\cdot e^{i\Delta m_s t}\cdot e^{-\frac{(\tau-\sigma\Sigma-t)^2}{2\sigma^2}} + \frac{(1-2\omega)}{2\sqrt{2\pi}\sigma}\int_{-\infty}^{\infty} e^{-\Gamma t}\cdot e^{-i\Delta m_s t}\cdot e^{-\frac{(\tau-\sigma\Sigma-t)^2}{2\sigma^2}} =$$

$$= \underbrace{\frac{1}{2\sqrt{2\pi}\sigma}\int_{-\infty}^{\infty} e^{\frac{\Delta\Gamma}{2}t}.....}_{\mathbf{I_1}} \qquad + \underbrace{\frac{1}{2\sqrt{2\pi}\sigma}\int_{-\infty}^{\infty} e^{-\frac{\Delta\Gamma}{2}t}.....}_{\mathbf{I_2}} \qquad +$$

$$\underbrace{\frac{(1-2\omega)}{2\sqrt{2\pi}\sigma}\int_{-\infty}^{\infty}e^{i\Delta m_s t}.....}_{\mathbf{I_3}} \qquad + \underbrace{\frac{(1-2\omega)}{2\sqrt{2\pi}\sigma}\int_{-\infty}^{\infty}e^{-i\Delta m_s t}.....}_{\mathbf{I_4}}$$

$$\mathbf{I_{1,2}} = \frac{1}{2\sqrt{2\pi}\sigma}\int_{-\infty}^{\infty}e^{\pm\frac{\Delta\Gamma}{2}t}\cdot e^{-\Gamma t}\cdot e^{-\frac{(\tau-\sigma\Sigma-t)^2}{2\sigma^2}}dt = \tag{4.59}$$

$$\frac{1}{2\sqrt{2\pi}\sigma}\int_{-\infty}^{\infty}e^{\pm\frac{\Delta\Gamma}{2}t}\cdot e^{-\Gamma t}\cdot e^{-\frac{\tau^2}{2\sigma^2}}e^{-\frac{t^2}{2\sigma^2}}\cdot e^{-\frac{\Sigma^2\sigma^2}{2\sigma^2}}e^{-\frac{\sigma\Sigma t}{\sigma^2}}\cdot e^{-\frac{\tau\Sigma}{\sigma}}e^{\frac{\tau t}{\sigma^2}}dt$$

$$= \frac{e^{-\frac{\tau^2}{2\sigma^2}}\cdot e^{-\frac{\Sigma^2\sigma^2}{2\sigma^2}}\cdot e^{-\frac{\tau\Sigma}{\sigma}}}{2\sqrt{2\pi}\sigma}\int_{-\infty}^{\infty}e^{\pm\frac{\Delta\Gamma}{2}t}\cdot e^{-\Gamma t}\cdot e^{-\frac{t^2}{2\sigma^2}}e^{-\frac{\sigma\Sigma t}{\sigma^2}}\cdot e^{\frac{\tau t}{\sigma^2}}dt =$$

$$\frac{e^{-\frac{\tau^2}{2\sigma^2}}\cdot e^{-\frac{\Sigma^2\sigma^2}{2\sigma^2}}\cdot e^{-\frac{\tau\Sigma}{\sigma}}}{2\sqrt{2\pi}\sigma}\int_{-\infty}^{\infty}e^{-\left(\Gamma\mp\frac{\Delta\Gamma}{2}-\frac{\tau}{\sigma^2}+\frac{\sigma\Sigma}{\sigma^2}\right)t}\cdot e^{-\frac{t^2}{2\sigma^2}}dt =$$

$$c \equiv \left(\Gamma \mp \frac{\Delta\Gamma}{2} - \frac{\tau}{\sigma^2} + \frac{\sigma\Sigma}{\sigma^2}\right)$$

$$\mathbf{I_{1,2}} = \frac{e^{-\frac{\tau^2}{2\sigma^2}}\cdot e^{-\frac{\Sigma^2\sigma^2}{2\sigma^2}}\cdot e^{-\frac{\tau\Sigma}{\sigma}}}{2\sqrt{2\pi}\sigma}\int_{-\infty}^{\infty}e^{-ct}\cdot e^{-\frac{t^2}{2\sigma^2}}dt = \frac{e^{-\frac{\tau^2}{2\sigma^2}}\cdot e^{-\frac{\Sigma^2\sigma^2}{2\sigma^2}}\cdot e^{-\frac{\tau\Sigma}{\sigma}}}{2\sqrt{2\pi}\sigma}\int_{-\infty}^{\infty}e^{-\left(\frac{t}{\sqrt{2}\sigma}+\frac{c}{\sqrt{2}}\sigma\right)^2}\cdot e^{+\frac{c^2\sigma^2}{2}}dt =$$

$$= \frac{e^{-\frac{\tau^2}{2\sigma^2}}\cdot e^{-\frac{\Sigma^2\sigma^2}{2\sigma^2}}\cdot e^{-\frac{\tau\Sigma}{\sigma}}e^{+\frac{c^2\sigma^2}{2}}}{2\sqrt{2\pi}\sigma}\int_{-\infty}^{\infty}e^{-\left(\frac{t}{\sqrt{2}\sigma}+\frac{c}{\sqrt{2}}\sigma\right)^2}\cdot dt$$

$$y \equiv \frac{t}{\sqrt{2}\sigma} + \frac{c}{\sqrt{2}}\sigma \qquad \Rightarrow \qquad dy = \frac{dt}{\sqrt{2}\sigma}$$

$$\mathbf{I_{1,2}} = \frac{e^{-\frac{\tau^2}{2\sigma^2}} \cdot e^{-\frac{\Sigma^2\sigma^2}{2\sigma^2}} \cdot e^{-\frac{\tau\Sigma}{\sigma}} e^{+\frac{c^2\sigma^2}{2}}}{2\sqrt{2\pi}\sigma} \int_{-\infty}^{\infty} e^{-y^2} \sqrt{2}\sigma \cdot dy = \frac{e^{-\frac{\tau^2}{2\sigma^2}} \cdot e^{-\frac{\Sigma^2\sigma^2}{2\sigma^2}} \cdot e^{-\frac{\tau\Sigma}{\sigma}} e^{+\frac{c^2\sigma^2}{2}}}{2\sqrt{2\pi}\sigma} \sqrt{2}\sigma\sqrt{2\pi} =$$

$$= \frac{e^{-\frac{\tau^2}{2\sigma^2}} \cdot e^{-\frac{\Sigma^2\sigma^2}{2\sigma^2}} \cdot e^{-\frac{\tau\Sigma}{\sigma}} e^{+\frac{c^2\sigma^2}{2}}}{\sqrt{2}} = e^{-\frac{\tau^2}{2\sigma^2}} \cdot e^{-\frac{\Sigma^2\sigma^2}{2\sigma^2}} \cdot e^{-\frac{\tau\Sigma}{\sigma}} \cdot \frac{e^{\left(\Gamma \mp \frac{\Delta\Gamma}{2} - \frac{\tau}{\sigma^2} + \frac{\sigma\Sigma}{\sigma^2}\right)^2 \frac{\sigma^2}{2}}}{\sqrt{2}} =$$

$$= e^{-\frac{\tau^2}{2\sigma^2}} \cdot e^{-\frac{\Sigma^2\sigma^2}{2\sigma^2}} \cdot e^{-\frac{\tau\Sigma}{\sigma}} \cdot \frac{e^{\left(\mp \frac{\Delta\Gamma}{2} + \frac{\Gamma - \tau + \sigma\Sigma}{\sigma^2}\right)^2 \frac{\sigma^2}{2}}}{\sqrt{2}} = \tag{4.60}$$

$$\mathbf{I_1} + \mathbf{I_2} = e^{-\frac{\tau^2}{2\sigma^2}} \cdot e^{-\frac{\Sigma^2\sigma^2}{2\sigma^2}} \cdot e^{-\frac{\tau\Sigma}{\sigma}} \cdot \left(\frac{e^{\left(\Gamma - \frac{\Delta\Gamma}{2} - \frac{\tau}{\sigma^2} + \frac{\sigma\Sigma}{\sigma^2}\right)^2 \frac{\sigma^2}{2}}}{\sqrt{2}} + \frac{e^{\left(\Gamma + \frac{\Delta\Gamma}{2} - \frac{\tau}{\sigma^2} + \frac{\sigma\Sigma}{\sigma^2}\right)^2 \frac{\sigma^2}{2}}}{\sqrt{2}} \right) =$$

$$= \frac{e^{-\frac{\tau^2}{2\sigma^2}} \cdot e^{-\frac{\Sigma^2\sigma^2}{2\sigma^2}} \cdot e^{-\frac{\tau\Sigma}{\sigma}}}{\sqrt{2}} \cdot \left[e^{+\left(\Gamma + \frac{\Delta\Gamma}{2} - \frac{\tau}{\sigma^2} + \frac{\sigma\Sigma}{\sigma^2}\right)^2 \frac{\sigma^2}{2}} + e^{+\left(\Gamma - \frac{\Delta\Gamma}{2} - \frac{\tau}{\sigma^2} + \frac{\sigma\Sigma}{\sigma^2}\right) \frac{\sigma^2}{2}} \right] =$$

$$\frac{e^{-\frac{\tau^2}{2\sigma^2}} \cdot e^{-\frac{\Sigma^2\sigma^2}{2\sigma^2}} \cdot e^{-\frac{\tau\Sigma}{\sigma}}}{\sqrt{2}} \cdot \left\{ e^{+\left[\Gamma^2 + \left(\frac{\Delta\Gamma}{2}\right)^2 + \left(\frac{\tau}{\sigma^2}\right)^2 + \left(\frac{\sigma\Sigma}{\sigma^2}\right)^2 + \Gamma\cdot\Delta\Gamma - 2\Gamma\cdot\frac{\tau}{\sigma^2} - \Delta\Gamma\cdot\frac{\tau}{\sigma^2} + \frac{2\Gamma\sigma\Sigma}{\sigma^2} + \frac{\Delta\Gamma\sigma\Sigma}{\sigma^2} - \frac{2\tau\sigma\Sigma}{\sigma^4}\right]\frac{\sigma^2}{2}} \right.$$
$$\left. + e^{+\left[\Gamma^2 + \left(\frac{\Delta\Gamma}{2}\right)^2 + \left(\frac{\tau}{\sigma^2}\right)^2 + \left(\frac{\sigma\Sigma}{\sigma^2}\right)^2 - \Gamma\cdot\Delta\Gamma - 2\Gamma\cdot\frac{\tau}{\sigma^2} + \Delta\Gamma\cdot\frac{\tau}{\sigma^2} + \frac{2\Gamma\sigma\Sigma}{\sigma^2} - \frac{\Delta\Gamma\sigma\Sigma}{\sigma^2} - \frac{2\tau\sigma\Sigma}{\sigma^4}\right]\frac{\sigma^2}{2}} \right\} =$$

$$\frac{e^{-\frac{\tau^2}{2\sigma^2}} \cdot e^{-\frac{\Sigma^2\sigma^2}{2\sigma^2}} \cdot e^{-\frac{\tau\Sigma}{\sigma}} \cdot e^{+\left[\Gamma^2 + \left(\frac{\Delta\Gamma}{2}\right)^2 + \left(\frac{\tau}{\sigma^2}\right)^2 + \left(\frac{\sigma\Sigma}{\sigma^2}\right)^2 - 2\Gamma\cdot\frac{\tau}{\sigma^2} + \frac{2\Gamma\sigma\Sigma}{\sigma^2}\right]\frac{\sigma^2}{2}}}{\sqrt{2}} \cdot$$
$$\cdot \left[e^{\frac{\Delta\Gamma}{2}\cdot\frac{\tau}{\sigma^2}\cdot\sigma^2 - \frac{\Delta\Gamma}{2}\cdot\Gamma\cdot\sigma^2 - \frac{\Delta\Gamma\sigma\Sigma}{\sigma^2}\frac{\sigma^2}{2} - \frac{2\tau\sigma\Sigma}{\sigma^4}\frac{\sigma^2}{2}} + e^{-\frac{\Delta\Gamma}{2}\cdot\frac{\tau}{\sigma^2}\cdot\sigma^2 + \frac{\Delta\Gamma}{2}\cdot\Gamma\cdot\sigma^2 + \frac{\Delta\Gamma\sigma\Sigma}{\sigma^2}\frac{\sigma^2}{2} + \frac{2\tau\sigma\Sigma}{\sigma^4}\frac{\sigma^2}{2}} \right] =$$

$$\frac{e^{-\frac{\tau^2}{2\sigma^2}}\cdot e^{-\frac{\Sigma^2\sigma^2}{2\sigma^2}}\cdot e^{-\frac{\tau\Sigma}{\sigma}}\cdot e^{+\frac{\Gamma^2\sigma^2}{2}+\frac{\sigma^2\Delta\Gamma^2}{8}+\frac{\tau}{2\sigma^2}^2+\frac{\Sigma}{\sigma^2}^2\frac{\sigma^2}{2}-\Gamma\tau+\Gamma\sigma\Sigma}}{\sqrt{2}}\cdot$$

$$\cdot 2\cosh\left(\frac{\Delta\Gamma\tau}{2}-\frac{\Delta\Gamma}{2}\cdot\Gamma\cdot\sigma^2-\frac{\Delta\Gamma\sigma\Sigma}{2}-\frac{\tau\Sigma}{\sigma}\right)=$$

$$=\sqrt{2}e^{-\frac{\tau\Sigma}{\sigma}}\cdot e^{+\frac{\Gamma^2\sigma^2}{2}+\frac{\sigma^2\Delta\Gamma^2}{8}-\Gamma\tau+\Gamma\sigma\Sigma}\cosh\left(\frac{\Delta\Gamma\tau}{2}-\frac{\Delta\Gamma}{2}\cdot\Gamma\cdot\sigma^2-\frac{\Delta\Gamma\sigma\Sigma}{2}-\frac{\tau\Sigma}{\sigma}\right)$$

$$\mathbf{I_{3,4}}=\frac{(1-2\omega)}{2\sqrt{2\pi}\sigma}\int_{-\infty}^{\infty}e^{-\Gamma t}\cdot e^{\pm i\Delta m_s t}\cdot e^{-\frac{(\tau-\sigma\Sigma-t)^2}{2\sigma^2}}dt=\frac{(1-2\omega)\cdot e^{-\frac{\tau^2}{2\sigma^2}}\cdot e^{-\frac{\Sigma^2}{2}}}{2\sqrt{2\pi}\sigma}\int_{-\infty}^{\infty}e^{-t\left(\Gamma\mp i\Delta m_s-\frac{\tau}{\sigma^2}+\frac{\sigma\Sigma}{\sigma^2}\right)}\cdot e^{-\frac{t^2}{2\sigma^2}}dt=$$

$$g\equiv\left(\Gamma\mp i\Delta m_s-\frac{\tau}{\sigma^2}+\frac{\sigma\Sigma}{\sigma^2}\right)$$

$$\mathbf{I_{3,4}}=\frac{(1-2\omega)\,e^{-\frac{\tau^2}{2\sigma^2}}\cdot e^{-\frac{\Sigma^2}{2}}}{2\sqrt{2\pi}\sigma}\int_{-\infty}^{\infty}e^{-gt}\cdot e^{-\frac{t^2}{2\sigma^2}}dt=$$

$$=\frac{(1-2\omega)\cdot e^{-\frac{\tau^2}{2\sigma^2}}\cdot e^{-\frac{\Sigma^2}{2}}}{2\sqrt{2\pi}\sigma}\int_{-\infty}^{\infty}e^{-\left(\frac{t}{\sqrt{2}\sigma}+\frac{g}{\sqrt{2}}\sigma\right)^2}\cdot e^{+\frac{g^2\sigma^2}{2}}dt=$$

$$=\frac{(1-2\omega)\,e^{-\frac{\tau^2}{2\sigma^2}}\cdot e^{-\frac{\Sigma^2}{2}}\cdot e^{\frac{g^2\sigma^2}{2}}}{2\sqrt{2\pi}\sigma}\int_{-\infty}^{\infty}e^{-z^2}dz=\frac{(1-2\omega)\cdot e^{-\frac{\tau^2}{2\sigma^2}}\cdot e^{-\frac{\Sigma^2}{2}}\cdot e^{\frac{g^2\sigma^2}{2}}}{2\sqrt{2\pi}\sigma}\cdot\sqrt{2}\sigma\cdot\sqrt{2\pi}=$$

$$= \frac{(1-2\omega)\cdot e^{-\frac{\tau^2}{2\sigma^2}}\cdot e^{-\frac{\Sigma^2}{2}}\cdot e^{\frac{g^2\sigma^2}{2}}}{\sqrt{2}} = \frac{(1-2\omega)\cdot e^{-\frac{\tau^2}{2\sigma^2}}\cdot e^{-\frac{\Sigma^2}{2}}\cdot}{\sqrt{2}} e^{\frac{\sigma^2}{2}\left(\Gamma\mp i\Delta m_s-\frac{\tau}{\sigma^2}+\frac{\sigma\Sigma}{\sigma^2}\right)^2} =$$

$$= \frac{(1-2\omega)\cdot e^{-\frac{\tau^2}{2\sigma^2}}\cdot e^{-\frac{\Sigma^2}{2}}\cdot}{\sqrt{2}} e^{\frac{\sigma^2}{2}\left(\Gamma^2-\Delta m_s^2+\frac{\tau^2}{\sigma^4}+\frac{\sigma^2\Sigma^2}{\sigma^4}\mp 2i\Gamma\Delta m_s-2\Gamma\frac{\tau}{\sigma^2}\pm 2i\frac{\tau\Delta m_s}{\sigma^2}+2\frac{\Gamma\sigma\Sigma}{\sigma^2}\mp 2i\Delta m_s\frac{\sigma\Sigma}{\sigma^2}-2\frac{\tau\sigma\Sigma}{\sigma^4}\right)} =$$

$$= \frac{(1-2\omega)\cdot e^{-\frac{\tau^2}{2\sigma^2}}\cdot e^{-\frac{\Sigma^2}{2}}\cdot e^{\frac{\sigma^2\Gamma^2}{2}}\cdot e^{-\frac{\sigma^2\Delta m_s^2}{2}}\cdot e^{+\frac{\tau^2}{2\sigma^2}}\cdot e^{+\frac{\Sigma^2}{2}}}{\sqrt{2}} e^{\frac{\sigma^2}{2}\left(\mp 2i\Gamma\Delta m_s-2\Gamma\frac{\tau}{\sigma^2}\pm 2i\frac{\tau\Delta m_s}{\sigma^2}+2\frac{\Gamma\sigma\Sigma}{\sigma^2}\mp 2i\Delta m_s\frac{\sigma\Sigma}{\sigma^2}-2\frac{\tau\sigma\Sigma}{\sigma^4}\right)}=$$

$$= \frac{(1-2\omega)\cdot e^{\frac{\sigma^2\Gamma^2}{2}}\cdot e^{-\frac{\sigma^2\Delta m_s^2}{2}}\cdot e^{-\Gamma\tau}\cdot e^{\Gamma\sigma\Sigma}\cdot e^{-\frac{\tau\Sigma}{\sigma}}}{\sqrt{2}} e^{\frac{\sigma^2}{2}\left(\mp 2i\Gamma\Delta m_s\pm 2i\frac{\tau\Delta m_s}{\sigma^2}\mp 2i\Delta m_s\frac{\sigma\Sigma}{\sigma^2}\right)}=$$

$$= \frac{\sqrt{2}}{2}(1-2\omega)\cdot e^{\frac{\sigma^2\Gamma^2}{2}}\cdot e^{-\frac{\sigma^2\Delta m_s^2}{2}}\cdot e^{-\Gamma\tau}\cdot e^{\Gamma\sigma\Sigma}\cdot e^{-\frac{\tau\Sigma}{\sigma}} e^{\left(\pm 2i\frac{\tau\Delta m_s}{\sigma^2}\frac{\sigma^2}{2}\mp 2i\Gamma\Delta m_s\frac{\sigma^2}{2}\mp 2i\Delta m_s\frac{\sigma\Sigma}{\sigma^2}\frac{\sigma^2}{2}\right)}=$$

$$= \frac{\sqrt{2}}{2}(1-2\omega)\cdot e^{\frac{\sigma^2\Gamma^2}{2}}\cdot e^{-\frac{\sigma^2\Delta m_s^2}{2}}\cdot e^{-\Gamma\tau}\cdot e^{\Gamma\sigma\Sigma}\cdot e^{-\frac{\tau\Sigma}{\sigma}} e^{\left(\pm i\tau\Delta m_s\mp i\Gamma\Delta m_s\sigma^2\mp i\Delta m_s\sigma\Sigma\right)}$$

$$\mathbf{I_3}+\mathbf{I_4} = \sqrt{2}(1-2\omega)\cdot e^{\frac{\sigma^2\Gamma^2}{2}}\cdot e^{-\frac{\sigma^2\Delta m_s^2}{2}}\cdot e^{-\Gamma\tau}\cdot e^{\Gamma\sigma\Sigma}\cdot e^{-\frac{\tau\Sigma}{\sigma}}\cdot\cos\left(\tau\Delta m_s-\Gamma\Delta m_s\sigma^2-\Delta m_s\sigma\Sigma\right)$$

$$\Rightarrow \quad \mathcal{R}\left(B\to\bar{f}\right) = \mathbf{I_1}+\mathbf{I_2}+\mathbf{I_3}+\mathbf{I_4} =$$

$$= \sqrt{2}\cdot e^{-\Gamma\tau}\cdot e^{\frac{\sigma^2\Gamma^2}{2}}\cdot e^{\Gamma\sigma\Sigma}\cdot e^{-\frac{\tau\Sigma}{\sigma}}\left\{\cdot e^{+\frac{\sigma^2\Delta\Gamma^2}{8}}\cosh\left(\frac{\Delta\Gamma\tau}{2}-\frac{\Delta\Gamma}{2}\cdot\Gamma\cdot\sigma^2-\frac{\Delta\Gamma\sigma\Sigma}{2}-\frac{\tau\Sigma}{\sigma}\right)+\right.$$

$$+(1-2\omega)\cdot e^{-\frac{\sigma^2\Delta m_s^2}{2}}\cdot\cos\left(\tau\Delta m_s-\Gamma\Delta m_s\sigma^2-\Delta m_s\sigma\Sigma\right)\Big\} \tag{4.61}$$

So the relative CP asymmetry is obtained by the ratio:

$$A_{CP}(t)=\frac{\Gamma(B^0\to f)-\Gamma(\overline{B}^0\to f)}{\Gamma(B^0\to f)+\Gamma(\overline{B}^0\to f)}=$$

$$=e^{-\frac{\sigma^2\Delta m_s^2}{2}}\cdot e^{-\frac{\sigma^2\Delta\Gamma^2}{8}}\cdot\frac{(1-2\omega)\cdot\cos\left(\tau\Delta m_s-\Gamma\Delta m_s\sigma^2-\Delta m_s\sigma\Sigma\right)}{\cosh\left(\frac{\Delta\Gamma\tau}{2}-\frac{\Delta\Gamma}{2}\cdot\Gamma\cdot\sigma^2-\frac{\Delta\Gamma\sigma\Sigma}{2}-\frac{\tau\Sigma}{\sigma}\right)}$$

Now I want to apply the same technique to the B decay to CP eigenstates case. In spite of the flavour specific decay, in this case there are only two decay mode:

$$\Gamma(B\to f)\propto e^{-\Gamma t}|A_f|^2\left(\left(1+|\lambda_f|^2\right)\cosh\frac{\Delta\Gamma}{2}t+\left(1-|\lambda_f|^2\right)\cos\Delta m\,t-2Re(\lambda)\sinh\frac{\Delta\Gamma}{2}t-2Im(\lambda_f)\sin\Delta m\,t\right)$$

$$\Gamma(\overline{B}\to f)\propto e^{-\Gamma t}|A_f|^2\left|\frac{p}{q}\right|^2\left(\left(1+|\lambda_f|^2\right)\cosh\frac{\Delta\Gamma}{2}t-\left(1-|\lambda_f|^2\right)\cos\Delta m\,t-2Re(\lambda)\sinh\frac{\Delta\Gamma}{2}t+2Im(\lambda_f)\sin\Delta m\,t\right)$$

By applying the convolution theory and the mistag effects, and assuming $|p/q|=1$, we can introduce the dependence to the distribution of the proper time resolution:

$$\mathcal{R}\,(B\to f)\propto e^{-\Gamma t}\left(\left(1+|\lambda_f|^2\right)\cosh\frac{\Delta\Gamma}{2}t+(1-2\omega)\left(1-|\lambda_f|^2\right)\cos\Delta m\,t-2Re(\lambda)\sinh\frac{\Delta\Gamma}{2}t-(1-2\omega)\,2Im(\lambda_f)\sin\Delta m\,t\right)$$

$$\otimes\frac{1}{\sqrt{2\pi}\sigma}e^{-\frac{(\tau-t)^2}{2\sigma^2}} \tag{4.62}$$

$$=\int_{-\infty}^{\infty}e^{-\Gamma t}\left(\left(1+|\lambda_f|^2\right)\cosh\frac{\Delta\Gamma}{2}t+(1-2\omega)\left(1-|\lambda_f|^2\right)\cos\Delta m\,t-2Re(\lambda)\sinh\frac{\Delta\Gamma}{2}t-(1-2\omega)\,2Im(\lambda_f)\sin\Delta m\,t\right)$$

$$\cdot\frac{1}{\sqrt{2\pi}\sigma}e^{-\frac{(\tau-t)^2}{2\sigma^2}}dt=$$

$$=\mathbf{I_1}+\mathbf{I_2}+\mathbf{I_3}+\mathbf{I_4}$$

where

$$\mathbf{I_1} = \int_{-\infty}^{\infty} \left(1+|\lambda_f|^2\right) \cosh\frac{\Delta\Gamma}{2} t \cdot \frac{e^{-\Gamma t}}{\sqrt{2\pi}\sigma} e^{-\frac{(\tau-t)^2}{2\sigma^2}} dt = \frac{\left(1+|\lambda_f|^2\right) e^{-\frac{\tau^2}{2\sigma^2}}}{\sqrt{2\pi}\sigma} \int_{-\infty}^{\infty} \cosh\frac{\Delta\Gamma}{2} t \, e^{-\Gamma t} \cdot e^{-\frac{t^2}{2\sigma^2}} \cdot e^{\frac{t\tau}{\sigma^2}} dt =$$

$$= \frac{\left(1+|\lambda_f|^2\right) e^{-\frac{\tau^2}{2\sigma^2}}}{\sqrt{2\pi}\sigma} \int_{-\infty}^{\infty} \frac{e^{\frac{\Delta\Gamma}{2}t} + e^{-\frac{\Delta\Gamma}{2}t}}{2} e^{-\Gamma t} \cdot e^{-\frac{t^2}{2\sigma^2}} \cdot e^{\frac{t\tau}{\sigma^2}} dt =$$

$$\mathbf{I_1} = \mathbf{I_{1A}} + \mathbf{I_{1B}}$$

$$\mathbf{I_{1A}}, \mathbf{I_{1B}} = \frac{\left(1+|\lambda_f|^2\right) e^{-\frac{\tau^2}{2\sigma^2}}}{2\sqrt{2\pi}\sigma} \int_{-\infty}^{\infty} e^{\pm\frac{\Delta\Gamma}{2}t} e^{-\Gamma t} \cdot e^{-\frac{t^2}{2\sigma^2}} \cdot e^{+\frac{t\tau}{\sigma^2}} dt =$$

$$= \frac{\left(1+|\lambda_f|^2\right) e^{-\frac{\tau^2}{2\sigma^2}}}{2\sqrt{2\pi}\sigma} \int_{-\infty}^{\infty} e^{\left(\pm\frac{\Delta\Gamma}{2}-\Gamma+\frac{\tau}{\sigma^2}\right)t} \cdot e^{-\frac{t^2}{2\sigma^2}} dt =$$

$$= \frac{\left(1+|\lambda_f|^2\right) e^{-\frac{\tau^2}{2\sigma^2}}}{2\sqrt{2\pi}\sigma} e^{\frac{\sigma^2}{2}\left(\pm\frac{\Delta\Gamma}{2}-\Gamma+\frac{\tau}{\sigma^2}\right)^2} \int_{-\infty}^{\infty} e^{-\left(\frac{t}{\sqrt{2}\sigma}-\frac{\sigma}{\sqrt{2}}\left(\pm\frac{\Delta\Gamma}{2}-\Gamma+\frac{\tau}{\sigma^2}\right)\right)^2} dt =$$

$$= \frac{\left(1+|\lambda_f|^2\right) e^{-\frac{\tau^2}{2\sigma^2}}}{2\sqrt{2\pi}\sigma} e^{\frac{\sigma^2}{2}\left(\pm\frac{\Delta\Gamma}{2}-\Gamma+\frac{\tau}{\sigma^2}\right)^2} \sqrt{2\pi}\sqrt{2}\sigma = \frac{\left(1+|\lambda_f|^2\right) e^{-\frac{\tau^2}{2\sigma^2}}}{2} e^{\frac{\sigma^2}{2}\left(\pm\frac{\Delta\Gamma}{2}-\Gamma+\frac{\tau}{\sigma^2}\right)^2} =$$

$$= \frac{\left(1+|\lambda_f|^2\right) e^{-\frac{\tau^2}{2\sigma^2}+\frac{\sigma^2\Delta\Gamma^2}{8}+\frac{\sigma^2\Gamma^2}{2}+\frac{\tau^2}{2\sigma^2}-\Gamma\tau\pm\left(\frac{\Delta\Gamma\tau}{2}-\frac{\sigma^2}{2}\Delta\Gamma\cdot\Gamma\right)}}{2} \Rightarrow$$

$$\mathbf{I_1} = \sqrt{2}\left(1+|\lambda_f|^2\right) e^{\frac{\sigma^2\Delta\Gamma^2}{8}+\frac{\sigma^2\Gamma^2}{2}-\Gamma\tau} \cdot \cosh\left(\frac{\Delta\Gamma}{2}\tau - \frac{\sigma^2}{2}\Delta\Gamma\cdot\Gamma\right) \qquad (4.63)$$

$$\mathbf{I_2} = \int_{-\infty}^{+\infty} (1-2\omega)\left(1-|\lambda_f|^2\right) \cos\Delta m\, t \cdot \frac{e^{-\Gamma t}}{\sqrt{2\pi}\sigma} e^{-\frac{(\tau-t)^2}{2\sigma^2}} dt =$$

$$= \frac{(1-2\omega)\left(1-|\lambda_f|^2\right) e^{-\frac{\tau^2}{2\sigma^2}}}{\sqrt{2\pi}\sigma} \int_{-\infty}^{+\infty} \cos\Delta m\, t \cdot e^{-\Gamma t} \cdot e^{-\frac{t^2}{2\sigma^2}} \cdot e^{\frac{t\tau}{\sigma^2}} dt =$$

$$= \frac{(1-2\omega)\left(1-|\lambda_f|^2\right) e^{-\frac{\tau^2}{2\sigma^2}}}{\sqrt{2\pi}\sigma} \int_{-\infty}^{+\infty} \frac{e^{i\Delta m\, t} + e^{-i\Delta m\, t}}{2} e^{-\Gamma t} \cdot e^{-\frac{t^2}{2\sigma^2}} \cdot e^{\frac{t\tau}{\sigma^2}} dt =$$

$$= \sqrt{2}\,(1-2\omega)\left(1-|\lambda_f|^2\right) e^{\frac{\Gamma^2\sigma^2}{2}-\frac{\sigma^2\Delta m^2}{2}-\Gamma\tau} \cos\left(\Delta m\,\tau - \Delta m\Gamma\sigma^2\right) \qquad (4.64)$$

$$\mathbf{I_3} = -\int_{-\infty}^{+\infty} 2Re(\lambda) \sinh\frac{\Delta\Gamma}{2} t \cdot \frac{e^{-\Gamma t}}{\sqrt{2\pi}\sigma} e^{-\frac{(\tau-t)^2}{2\sigma^2}} dt =$$

$$= -2\sqrt{2}\, Re(\lambda_f) e^{\frac{\Gamma^2\sigma^2}{2}+\frac{\sigma^2\Delta\Gamma^2}{8}-\Gamma\tau} \sinh\left(\frac{\Delta\Gamma}{2}\,\tau - \frac{\Delta\Gamma}{2}\Gamma\sigma^2\right) \qquad (4.65)$$

$$\mathbf{I_4} = -\int_{-\infty}^{+\infty} (1-2\omega)\, 2Im(\lambda_f) \sin\Delta m\, t \cdot \frac{e^{-\Gamma t}}{\sqrt{2\pi}\sigma} e^{-\frac{(\tau-t)^2}{2\sigma^2}} dt =$$

$$= -2\sqrt{2} Im(\lambda_f)\,(1-2\omega)\, e^{\frac{\Gamma^2\sigma^2}{2} - \frac{\sigma^2\Delta m^2}{2} - \Gamma\tau} \sin\left(\Delta m\,\tau - \Delta m\,\Gamma\sigma^2\right) \qquad (4.66)$$

Hence

$$\mathcal{R}\,(B \to f) \propto e^{\frac{\sigma^2\Delta\Gamma^2}{8} + \frac{\sigma^2\Gamma^2}{2} - \Gamma\tau} \cdot \left(\left(1 + |\lambda_f|^2\right) \cosh\left(\frac{\Delta\Gamma}{2}\tau - \frac{\Delta\Gamma}{2}\Gamma\sigma^2\right) - 2Re(\lambda_f) \sinh\left(\frac{\Delta\Gamma}{2}\tau - \frac{\Delta\Gamma}{2}\Gamma\sigma^2\right)\right) +$$

$$+ (1-2\omega)\, e^{\frac{\Gamma^2\sigma^2}{2} - \frac{\sigma^2\Delta m^2}{2} - \Gamma\tau} \left(\left(1 - |\lambda_f|^2\right) \cos\left(\Delta m\,\tau - \Delta m\Gamma\sigma^2\right) - 2Im(\lambda_f) \sin\left(\Delta m\,\tau - \Delta m\,\Gamma\sigma^2\right)\right) \qquad (4.67)$$

$$\mathcal{R}\,(\overline{B} \to f) \propto e^{\frac{\sigma^2\Delta\Gamma^2}{8} + \frac{\sigma^2\Gamma^2}{2} - \Gamma\tau} \cdot \left(\left(1 + |\lambda_f|^2\right) \cosh\left(\frac{\Delta\Gamma}{2}\tau - \frac{\Delta\Gamma}{2}\Gamma\sigma^2\right) - 2Re(\lambda_f) \sinh\left(\frac{\Delta\Gamma}{2}\tau - \frac{\Delta\Gamma}{2}\Gamma\sigma^2\right)\right) +$$

$$- (1-2\omega)\, e^{\frac{\Gamma^2\sigma^2}{2} - \frac{\sigma^2\Delta m^2}{2} - \Gamma\tau} \left(\left(1 - |\lambda_f|^2\right) \cos\left(\Delta m\,\tau - \Delta m\Gamma\sigma^2\right) - 2Im(\lambda_f) \sin\left(\Delta m\,\tau - \Delta m\,\Gamma\sigma^2\right)\right) \qquad (4.68)$$

So the CP asymmetry can be computed

$$A_{CP}(t) = -\,(1-2\omega)\, e^{-\frac{\sigma^2\Delta m^2}{2} - \frac{\sigma^2\Delta\Gamma^2}{8}} \cdot \frac{\left(1 - |\lambda_f|^2\right) \cos\left(\Delta m\,\tau - \Delta m\Gamma\sigma^2\right) - 2Im(\lambda_f) \sin\left(\Delta m\,\tau - \Delta m\,\Gamma\sigma^2\right)}{\left(1 + |\lambda_f|^2\right) \cosh\left(\frac{\Delta\Gamma}{2}\tau - \frac{\Delta\Gamma}{2}\Gamma\sigma^2\right) - 2Re(\lambda_f) \sinh\left(\frac{\Delta\Gamma}{2}\tau - \frac{\Delta\Gamma}{2}\Gamma\sigma^2\right)} =$$

$$= (1-2\omega)\, e^{-\frac{\sigma^2\Delta m^2}{2} - \frac{\sigma^2\Delta\Gamma^2}{8}} \cdot \frac{A_{CP}^{dir} \cdot \cos\left(\Delta m\,\tau - \Delta m\Gamma\sigma^2\right) + A_{CP}^{mix} \sin\left(\Delta m\,\tau - \Delta m\,\Gamma\sigma^2\right)}{\cosh\left(\frac{\Delta\Gamma}{2}\tau - \frac{\Delta\Gamma}{2}\Gamma\sigma^2\right) - A_{CP}^{\Delta} \sinh\left(\frac{\Delta\Gamma}{2}\tau - \frac{\Delta\Gamma}{2}\Gamma\sigma^2\right)} \qquad (4.69)$$

analogously for a bias $b = \Sigma\sigma$ on the time resolution distribution

$$(1-2\omega)\, e^{-\frac{\sigma^2\Delta m^2}{2} - \frac{\sigma^2\Delta\Gamma^2}{8}} \cdot \frac{A_{CP}^{dir} \cdot \cos\left(\Delta m\,\tau - \Delta m\Gamma\sigma^2 + \Delta m\frac{\Sigma}{\sigma}\right) + A_{CP}^{mix} \sin\left(\Delta m\,\tau - \Delta m\,\Gamma\sigma^2 + \Delta m\frac{\Sigma}{\sigma}\right)}{\cosh\left(\frac{\Delta\Gamma}{2}\tau - \frac{\Delta\Gamma}{2}\Gamma\sigma^2 + \frac{\Delta\Gamma}{2}\Sigma\sigma\right) - A_{CP}^{\Delta} \sinh\left(\frac{\Delta\Gamma}{2}\tau - \frac{\Delta\Gamma}{2}\Gamma\sigma^2 + \frac{\Delta\Gamma}{2}\Sigma\sigma\right)} \qquad (4.70)$$

Appendix D

Mass Difference

Mixing occurs when eigenstates of one observable-flavour, are not pure mass eigenstates but formed by superposition of mass eigenstates. The flavour states will alter over time in two distinct ways. First the amplitudes of the different mass eigenstate components will decay at different rates, given by the width difference.

Second the phases of the components will vary at different frequencies according to their mass eigenvalues. This evolution of relative phase drives flavour oscillation at the beat frequency.

Starting from the eq.2.17 we can see that

$$\frac{q}{p} = -\frac{M_{12}^*}{|M_{12}|}\left[1 - \frac{1}{2} Im\left(\frac{\Gamma_{12}}{M_{12}}\right)\right] \tag{4.71}$$

Since in the B_s mesons $|M_{12}| \gg |\Gamma_{12}|$, the approximation

$$\frac{q}{p} = -\frac{M_{12}^*}{|M_{12}|}$$

is quite good. Also we can take in account that, within the standard model,

$$M_{12} \propto (V_{ts}^* V_{tb})^2 \propto (V_{ts}^*)^2 \tag{4.72}$$

Therefore the

$$\frac{q}{p} = \frac{V_{ts}^2}{V_{ts} V_{ts}^*} = e^{2i\delta\gamma} \rightarrow \left|\frac{q}{p}\right| = 1 \tag{4.73}$$

can be assumed to within $\mathcal{O}(10^{-3})$. The measurements of the mass difference

in the B_s system achieve an improvement about the knowledge of the V_{CKM} element V_{ts}. Actually the $|M_{12}| \gg |\Gamma_{12}|$, then

$$\Delta m_s \approx 2|M_{12}| \tag{4.74}$$

therefore we can extract the value of V_{ts} through the eq.4.72.

Another way to measure the validity of the CKM matrix is estimating the ratio:

$$\frac{\Delta m_s}{\Delta m_d} = \left|\frac{V_{ts}}{V_{td}}\right| \cdot R_{sd} \tag{4.75}$$

where the R_{sd} contains a set of parameter almost valued.

Present situation on Δm_s

The first attempts to measure the Δm_s have yielded a lower limit $\Delta m_s > 14.5\ ps^{-1}$ with a confidence level of 95%. Recently D0 collaboration reported the interval $17\ ps^{-1} < \Delta m_s < 21\ ps^{-1}$at 90% C.L. using a large sample of B_s semileptonic decays.

However the most recently result comes from the CDF experiment which has published [17] [18] these results:

$$\Delta m_s = 17.77 \pm 0.10(stat) \pm 0.07\ (sys) \tag{4.76}$$

$$\left|\frac{V_{td}}{V_{ts}}\right| = 0.2060^{+0.001}_{-0.002} \pm 0.0007(exp)^{+0.081}_{-0.060}(theor) \tag{4.77}$$

To reach these value the CDF Collaboration has employed 1 fb^{-1} of data from $p\bar{p}$ collisions at $\sqrt{s} = 1.96$TeV collected with the CDF II detector at the Fermilab Tevatron. The sample contains signals of 5600 fully reconstructed hadronic B_s decays. 3100 partially reconstructed hadronic B_s decays, and 61500 partially reconstructed semileptonic B_s decays. The probability was measured as a function of proper decay time that the B_s decays with the same, or opposite, flavour as the flavour at production. To fulfill the measurements of the value of the Δm_s has been employed the amplitude scan technique.

The amplitude scan

This methods exploits the likelihood technique. In fact the likelihood term describing the tagged proper decay time of a $B^0_{d,s}$ meson is modified by including an additional parameter multiplying the cosine term. This parameter is called the amplitude A

$$\mathcal{L} \propto 1 \pm A \cdot D \cdot \cos(\Delta m \cdot t) \tag{4.78}$$

where the A parameter is left free during the fit, while D is fixed and known in the scan procedure. In this wise we calculate an A value for each Δm. In case of infinite statistics, optimal resolution and perfect tagging, one would expect A to be unity for the true Δm_s value. In practice a set of fitted values (A, σ_A)

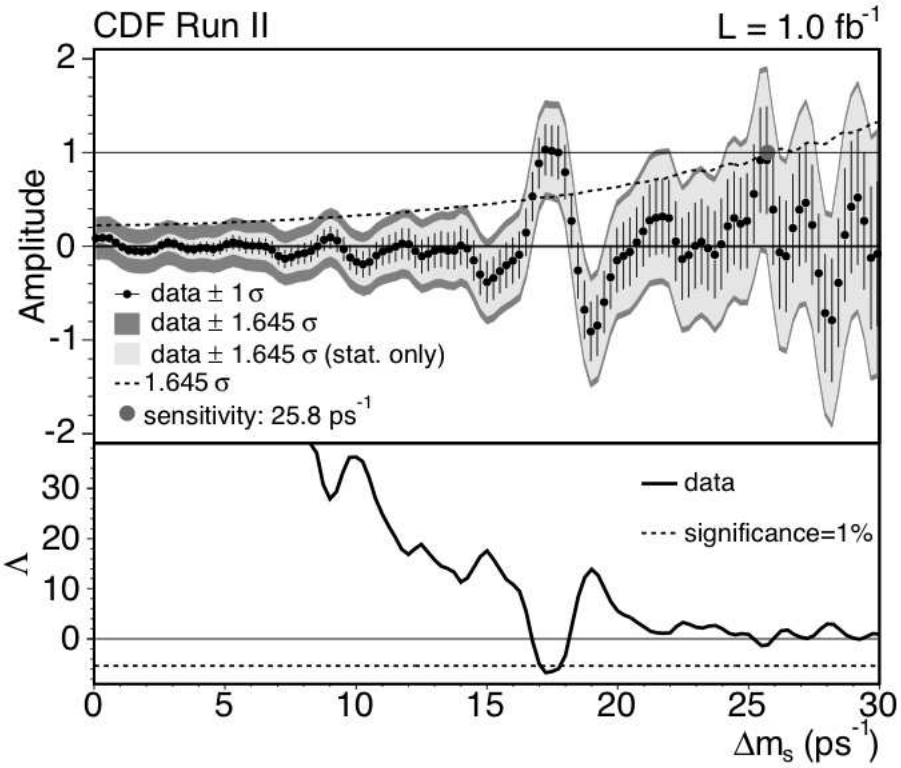

Figure 4.12: (Upper) The measured amplitude values and uncertainties versus $B_s\bar{B}_s$oscillation frequency Δm_s. At $17.77\,ps^{-1}$the amplitude is consistent with one and inconsistent with zero at 3.7 σ. (Lower) The logarithm of the ratio of likelihoods for amplitude equal to zero and amplitude equal to one, $\Lambda = \log\left[\mathcal{L}^{\mathcal{A}=0}/\mathcal{L}^{\mathcal{A}=1}(\Delta m_s)\right]$, versus the oscillation frequency. The dashed horizontal line indicates the value of Λ that corresponds to a probability of 1% in the case of randomly tagged data.

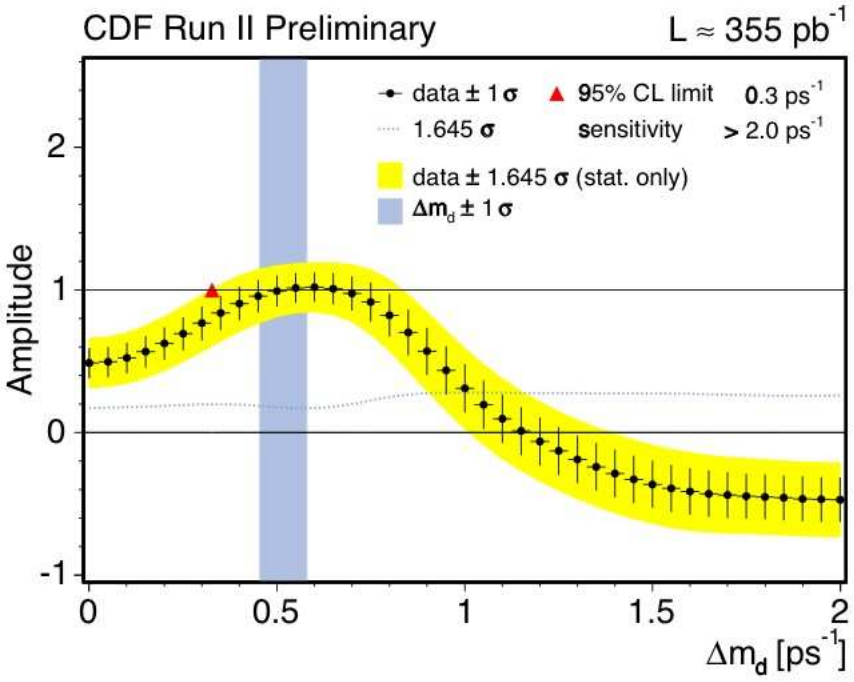

Figure 4.13: The amplitude scan for the B_d system at CDF II.

for each Δm_s hypothesis is obtained. A Δm_s hypothesis is excluded to a 95% confidence level in case the following relation is observed

$$A + 1.645\sigma_A < 1$$

The sensitivity of a mixing measurement is defined as the Δm value for which $1.645\sigma_A = 1$. The figure 4.13 shows the result of the amplitude scan to B_d mesons at CDF II.

LHCb technique

Another approach to extract directly the Δm_s value is to zero in on the shape of the CP asymmetry generated by the proper time distributions of the events that have been flavour-tagged as having oscillated. In LHCb the decay $B_s \to D_s^- \pi^+$ will be used to determine the oscillation frequency Δm_s.

The decay channel $B_s/\overline{B}_s \to D_s^{\mp}\pi^{\pm}$ is self tagging, i.e. the charge of $D_s^{\mp}$ identifies univocal the flavour of the B meson at the decay instant. This decay is very important in the delta mass determination. Thus $A_f = \bar{A}_f \Rightarrow \lambda = \bar{\lambda} = 0$ and with $\left|\frac{p}{q}\right| = 1$ the flavour asymmetry can be defined as

$$A^{flav} = \frac{\Gamma_{\bar{B}\to f(t)} - \Gamma_{B\to f(t)}}{\Gamma_{\bar{B}\to f(t)} + \Gamma_{B\to f(t)}} = -D \cdot \frac{\cos(\Delta m_s t)}{\cosh(\Delta\Gamma_s t)} \tag{4.79}$$

where D is a dilution factor that comes under the wrong tag fraction ω with the equality $D = (1 - 2\omega)$. This observable provides also information about the $\Delta\Gamma$.

The $D_s^{\mp}$ doesn't have a favoured decay channel. The highest rate, $(10.8 \pm 3.1)\%$, decay channel is $D_s^- \to \eta^0(\pi^+\pi^-\pi^0)\rho^-(\pi^-\pi^0)$. It is easy to understand that the reconstruction of this channel quite difficult, since the neutral particles among the final states that increase the $\gamma\gamma$ combinatorial background.

Also $D_s^{\mp}$ can decay into the $K^+K^-\pi^{\mp}$ final state with a branching fraction of $(4.4 \pm 1.2)\%$ and thus this decay mode is more convenient since there are less final states and no neutral particles and it is a resonant decay mode.

The observed distribution proper time is quite different from the true distribution due the acceptance and the time resolution. The selection of the events requires that a B_s travels at least 2.5 mm downstream. This condition, not only suppresses the background level, but also it cuts all the signal events which have a true lifetime smaller than $2ps$. With Monte Carlo studies, we obtain a fitted function, in term of τ, of the form:

$$\epsilon(\tau) = N\frac{(a\tau)^5}{1 + (a\tau)^5} \tag{4.80}$$

where N and a are the fitted parameters. N is the asymptotically acceptance reached for great values of proper time.

Another pejorative term is the time resolution. The proper lifetime of a B_s meson is calculated from its momentum and the separation of the primary and secondary vertexes as shown in eq. 3.1. The uncertainty in the secondary vertex dominates the accuracy of the measurement.

Bibliography

[1] G.Balbi et al., The selection crate for the L0 calorimeter trigger , LHCb-2003-095

[2] E. Noether, Invariante Variationsprobleme, Nachr. v. d. Ges. d. Wiss. zu Göttingen 1918, pp235-257

[3] Gerhart Luders and Bruno Zumino. Some consequences of the TCP Invariance, Phys. Rev. 106, 385-386, 1957

[4] C. S. Wu, E. Ambler, R. W. Hayward, D. D. Hoppes and R. P. Hudson, Phys. Rev. **105** (1957) 1413.

[5] J. H. Christenson, J. W. Cronin, V. L. Fitch and R. Turlay, Phys. Rev. Lett. **13** (1964) 138.

[6] A. D. Sakharov, Pisma Zh. Eksp. Teor. Fiz. **5** (1967) 32 [JETP Lett. **5** (1967 SOPUA,34,392-393.1991 UFNAA,161,61-64.1991) 24].

[7] V. A. Rubakov and M. E. Shaposhnikov, *Prepared for CERN-Santiago de Compostela-La Plata Meeting on Trends in Theoretical Physics, CERN-Santiago de Compostela-La Plata, Argentina, 28 Apr - 6 May 1997*

[8] I.Bigi, A.I.Sanda, CP Violation. 2000

[9] V.F.Weisskopf and E.P.Wigner, *Z. Phys.* 63 54 (1930); *Z. Phys.* 65 18(1830)

[10] L.Bart Anton Hommels. *The Tracker in the Trigger of LHCb* Ph.D thesis (2006)

[11] J. van Tilburg, *Track simulation and reconstruction in LHCb*, Ph.D. thesis, NIKHEF, 2005, CERN-THESIS/2005-040.

[12] G. Barrand et al., GAUDI - *A software architecture and framework for building HEP data processing applications*, Comput. Phys. Commun. 140 (2001) 45.

[13] L.Fernandez, P.Koppenburg. HTL Exclusive Selections Design and Implementation. LHCb 2005-015, LPHE 2005-011, 2005

[14] LHCb Trigger System. CERN/LHCC 2003-31, 2003

[15] LHCb Reoptimized Detector Design and Performance, TDR 2003

[16] LHCb RICH TDR, CERN LHCC 2000-037

[17] CDF Collaboration, Measurements of the $B_s - \bar{B}_s$ oscillation frequency, hep-ex 0606027

[18] CDF Collaboration, Observation of the $B_s - \bar{B}_s$ oscillations, hep-ex/0609040

[19] V.Blobel, Formulae and methods in experimental data evaluation, vol.3 European Physical Society.

[20] Quarteroni, Sacco, Saleri, Matematica Numerica. Springer

[21] Martin, Statistics for Physicists, 1971 Academic Press London and New York

[22] Mood, Graybill, Boes. Introduzione alla statistica, McGraw-Hill

[23] `RooFit` Package http://roofit.sourceforge.net/

[24] H. G. Moser and A. Roussarie, Nucl. Instrum. Meth. A **384**, 491 (1997).

[25] I. I. Bigi, arXiv:hep-ph/0608225.

[26] A. J. Buras, arXiv:hep-ph/0505175.

[27] M. Bander, D. Silverman and A. Soni, Phys. Rev. Lett. **43** (1979) 242.

[28] R. Fleischer, arXiv:hep-ph/9908341.

[29] Atwood, Dunietz, Soni, Enhanced CP Violation with $B \to KD^0(\overline{D}^0)$ Modes and Extraction of the CKM Angle γ.

[30] Bigi, Sanda , Phys. Lett. 211B, 213 (1998)

[31] G.Balbi et al. Weak phase gamma and SU(3) breaking from $B_d \to \pi^+\pi^-$, $B_s \to K^+K^-$ and $B_s \to K^0\bar{K}^0$ decays at LHCb, CERN, LHCb-2003-164, (2003).

[32] See P.Vankov CERN presentations 2006

[33] See B.Carron CERN presentations 2005

[34] See S.Vecchi or G.Balbi CERN presentations: 2004/2006

[35] R. Fruhwirth, et al., Data analysis techniques for high-energy physics, Cambridge monographs on particle physics, nuclear physics and cosmology, 2000; R.K. Bock, et al., Formulae and methods in experimental data evaluation, European Physical Society, 1984.

[36] See presentation by Jeroen van Tilburg and M.Merk at LHCb Reconstruction meeting, 23 Nov 23, 2004